

Pål Gunnar Ellingsen

**Polarimetric and  
hyperspectral imaging  
methods for characterisation  
of bio- and nanomaterials**

Thesis for the degree of Philosophiae Doctor

Trondheim, August 2014

Norwegian University of Science and Technology  
Faculty of Natural Sciences and Technology  
Department of Physics



**NTNU – Trondheim**  
Norwegian University of  
Science and Technology

**NTNU**

Norwegian University of Science and Technology

Thesis for the degree of Philosophiae Doctor

Faculty of Natural Sciences and Technology  
Department of Physics

© Pål Gunnar Ellingsen

ISBN 978-82-326-0392-3 (printed ver.)  
ISBN 978-82-326-0393-0 (electronic ver.)  
ISSN 1503-8181

Doctoral theses at NTNU, 2014:238

Printed by NTNU-trykk

# Abstract

Presented here is the development of a time gated Raman spectrometer, a new method for designing polarimeters, testing of an overdetermined Mueller matrix imaging ellipsometer and Mueller matrix imaging of collagen fibre directions and silicon strain. In addition, a new method, spectral correlation, for analysing hyperspectral images, is developed, implemented and tested.

The time gated Raman spectrometer is capable of gating away long lifetime luminescence ( $> 2$  ns), by using a time gated ICCD and a 2 ns pulsed Nd:YAG laser. Furthermore, the system can be used to study UV resonance Raman effects, due to the third (355 nm) and fourth (266 nm) order harmonic excitations available.

For optimising broadband polarimeters, genetic algorithms are employed. The resulting polarimeters are demonstrated to have a lower noise propagation and a broader spectral range, compared to previous commercial and patented designs. One of the designs is realised as a Mueller matrix liquid crystal variable retarder based ellipsometer. Its performance is in good agreement with computer optimised models. For calibrating the instrument, an extended version of the eigenvalue calibration method is employed.

Mueller matrix imaging is used together with state of the art decomposition methods to image collagen fibre orientations in cartilage and tendon. 3D directional imaging of the collagen fibres is achieved by using different angles of incidence upon the sample and a new method for calculating the fibre direction from the linear retardance. The method uses an effective medium approach to justify that the slow axis is along the direction of the fibres. A similar approach is used to study strain in silicon wafers.

Lastly, a spectral correlation method for analysing hyperspectral fluorescence images is developed and demonstrated to be good for analysing double stained amyloid plaques in mice. The resulting analysis allows for calculating the radius dependent mean and standard deviations for a set of plaques as a function of radius. By studying amyloid plaques from mice of different ages, it was found that there were significant changes with age in the structure of the plaques. Furthermore, the method was found to work well for analysing multi-component Raman spectra, where it detected small amounts of tetrahydrofuran in water.



# Preface

This thesis is a major part of the requirements for a Philosophiae Doctor (PhD) degree from the Norwegian University of Science and Technology (NTNU). The work was conducted from September 2010 to June 2014, and the main location for it was the optical labs at the Department of Physics. It was supervised by Professor Mikael Lindgren and co-supervised by Professor Morten Kildemo. The work would not have been possible, had it not been for the nice group of people which I have had the pleasure of working with.

I specially want to thank Mikael Lindgren, who has given me excellent guidance, help, ideas and opportunities during the work. He has helped me with publishing my result through good discussions and assistance in writing the papers.

Morten Kildemo has been a very good co-supervisor on my thesis, as well as my masters degree supervisor. He has helped me greatly, and I am grateful for everything he thought me during my masters degree and for the help and discussions I have received.

The single most important person for this thesis is Lars Martin, who has become a close friend during our collaboration. He started his PhD a year before me, and as a consequence supervised me on my master, during which we lay the foundations for much of our research. In times of frustration he has been there to give advice, and the discussions, brainstorming, problem solving and publishing we have done together, have resulted in excellent research and publications. The sum of our work is greater than what we could have done alone.

The lunch discussions in our group were fruitful and resulted in several papers. These discussions would not have been possible, had it not been for Paul Anton, Tor, Ingar, Daniel, Jerome and Zhara. All of whom have become friends of mine.

I also wish to thank Julien for the initial design of the time gated Raman spectrometer. Eirik, who did his PhD before I started, I want to thank for the help in understanding excited state absorption.

A large part of my work was focused towards biomedical research. As part of this I have collaborated with the biophysics group at the department of physics. I want to thank Magnus, Rajesh, Nina and Astrid for the collaboration and samples they have provided.

I especially want to thank Thor Bernt for being like a second co-supervisor,

always available for questions, and enquiring how my work is going.

From the rest of the department I want to thank Per Magne for always trying to find dissused equipment I could salvage, Ingve for being available for any theoretical questions I might have and Åsmund for showing that there is always a silver lining.

From the department of computer and information sciences I want to thank Keith for the help he has given me on understanding genetic algorithms. At the department of cancer research and molecular medicine I want to thank Odrun for the work done on photodynamic therapy.

From Sweden and Linköping University I want to thank Sofie and Per for providing the opportunity to analyse data sets and samples of amyloid plaques. I also want to thank Cesar at FOI and Thomas at Umeå University for the collaboration on optical power limiting materials.

From ENS, Lyon, I want to thank Chantal and Stephane. Furthermore I wish to thank Patrice in Grenoble.

During my work I have had the pleasure of supervising several master students, some of whose work have resulted in publications. I therefore want to thank Vegard, Thomas Brakstad, Monica, Thomas Trøen, Anette, Brede, Bent and Eirik

From my own master study I want to thank Nick Robins and John D. Close at the ANU, Australia, for getting me interested in optical instrumentation.

Additionally, I want to thank all the other collaborators I have had the pleasure to work with, especially the LUPAS project.

My family, above all mum Fiona, dad Kjell and sister Inger, are very important for me, and have been important in getting me interested in science and supporting me. I love you all. I also want to thank the family friends Lise and Ketil for thier support and showing how interesting nature can be.

My time in Trondheim was made pleasant through my friends and the university sportsclub NTNUI, especially the dance club. Thank you all for providing something to focus on and have fun with, during my spare time.

During the finalisation of this thesis Paul Anton, Vegard, Morten, Mikael, Lars and, my mum and dad have been of great help for proofreading and correcting mistakes in the thesis. Thank you very much for the time spent on this.

I want to thank "Norges tekniske høgskoles fond", SINTEF and the faculty for travel support. I want to thank the university for the techniques I learned during "Researchers Grand Prix". I also want to thank the department for teaching me the importance of retaining any information in writing. Wikipedia has been an excellent entry portal for finding information. For finding quotes for the thesis I want to thank goodreads.com for their extensive database.

# List of papers

This chapter contains a list of scientific papers which I have published during the progress of my PhD work. It is split in two sections, the first contains the main papers of the thesis, and the second section is a list of papers related to the work presented in the thesis. Following the PhD regulations at NTNU, the main contribution of each author is outlined.

## Paper 1

P. A. Letnes, I. S. Nerbø, L. M. S. Aas, P. G. Ellingsen, and M. Kildemo, “Fast and optimal broad-band Stokes/Mueller polarimeter design by the use of a genetic algorithm,” *Opt. Express* **18**, 10 (2010)

As a result of an excellent lunch discussion about the problem of optimising polarimetric broadband designs, the ideas for this paper were proposed on the basis of a course in genetic algorithms taken by PAL. The genetic algorithms turned out to be very suitable for optimising polarimeters.

The main author of this paper was PAL, who wrote the Python code. He also wrote the related parts of the paper i.e., the genetic algorithm and the results. The other parts were mostly written by ISN, though LMSA wrote a few paragraphs. I and LMSA developed software to confirm the results. All the authors contributed to the discussion part of the paper.

## Paper 2

L. M. S. Aas, P. G. Ellingsen, B. E. Fladmark, P. A. Letnes, and M. Kildemo, “Overdetermined broadband spectroscopic Mueller matrix polarimeter designed by genetic algorithms,” *Opt. Express* **21**, 8753 – 8762 (2013)

Having found the results in paper 1, the next step was to realise a polarimeter designed by a genetic algorithm.

Together with PAL, I developed a new software, using a Python library for genetic optimisation. PAL did most of the backbone of the program, while I did more of the polarimeter specific programming, implementing all the different components and the measured data from them. BEF, a master student, was

supervised by LMSA, and together they realised the experimental system. I made minor contributions in this process.

The first draft of the paper was written by LMSA, while I and MK helped under the revisions.

### **Paper 3**

L. M. S. Aas, P. G. Ellingsen, M. Kildemo, and M. Lindgren, “Dynamic response of a fast near infra-red Mueller matrix ellipsometer,” *J. Mod. Opt.* **57**(17), 1603–1610 (2010)

This paper explains the dynamic properties of the Mueller matrix imaging ellipsometer. It has been the basis for the understanding and developing of our system.

MK wrote the draft, LMSA improved upon it and made it ready for publication. I and LMSA did the experimental part together. All the authors took part in the final discussion

### **Paper 4**

L. M. S. Aas, P. G. Ellingsen, and M. Kildemo, “Near infra-red Mueller matrix imaging system and application to retardance imaging of strain,” *Thin Solid Films* **519**, 2737–2741 (2011)

Strain in multicrystalline silicon is imaged by using the Mueller matrix imaging ellipsometer.

LMSA did the experimental work and wrote the paper. I and MK helped in finalising the paper and discussing the results.

### **Paper 5**

P. G. Ellingsen, M. B. Lilledahl, L. M. S. Aas, C. D. L. Davies, and M. Kildemo, “Quantitative characterization of articular cartilage using Mueller matrix imaging and multiphoton microscopy,” *J. Biomed. Opt.* **16**, 116002 (2011)

Using Mueller matrix imaging (MMI) and second harmonic generation (SHG), the collagen fibres in articular cartilage from a chicken knee were studied. By employing an effective medium approach, the direction of the collagen fibers in plane could be determined from MMI. SHG was then used to verify the results.



I recorded and analysed the Mueller matrix images, while MBL recorded the SHG images. The paper was written by me and MBL, with help from MK and LMSA on the discussion and analysis.

### **Paper 6**

P. G. Ellingsen, L. M. S. Aas, V. S. Hagen, R. Kumar, M. B. Lilledahl, and M. Kildemo, “Mueller matrix three-dimensional directional imaging of collagen fibers,” *J. Biomed. Opt.* **19**, 26002 (2014)

In this paper, a continuation of the work in paper 5, I extended the in plane method for determining the collagen fibre direction to 3D directions, by recording images at different angles of incidence.

The samples were prepared by RK, who also recorded the SHG images. The MMI images were taken by me and VSH. I did the analysis and wrote most of the paper. LMSA helped with the development of the model. All authors took part in the discussion and the revising of the paper.

### **Paper 7**

P. G. Ellingsen, N. K. Reitan, B. D. Pedersen, and M. Lindgren, “Hyperspectral analysis using the correlation between image and reference,” *J. Biomed. Opt.* **18**, 20501 (2013)

The characterisation of the spectral differences in hyperspectral images has been done in a range of different ways depending on the available data and the application. These methods had up until then focused either on linear processes or not knowing much about the sample. With MLs knowledge of radar technology and image recognition using optical correlation, he suggested the use of the correlation coefficient for a statistical determination of the differences in spectra. I developed the method, wrote the code and applied it on a data set from NKR and BDP. The article was written by me, with help and suggestions from the coauthors.

### **Paper 8**

P. G. Ellingsen, S. Nyström, N. K. Reitan, and M. Lindgren, “Spectral correlation analysis of amyloid  $\beta$  plaque inhomogeneity from double staining experiments,” *J. Biomed. Opt.* **18**, 101313 (2013)

This is the application of the correlation coefficient method, paper 7, on tissue slices from mice with Alzheimer’s disease. The work was part of the LUPAS EU-project.

I developed the software used for the analysis. Some of the data handling was done by NKR. The samples were prepared by SN and imaged by NKR and SN. Most of the paper was written by me. All authors contributed to all parts of article and in the discussion.

### **Paper 9**

P. G. Ellingsen and M. Lindgren, “Design and test of a Raman spectroscopic system based on a time-gated intensified CCD,” *Submitt. to Opt. Express* **4**, June 2014 (2014)

This paper shows the design and test of a time gated Raman and luminescence spectrometer. In addition, it shows the application of the spectral correlation method, from papers 7 and 8, to analyse Raman spectra.

I developed the system and did all the measurements, with guidance from ML. The paper was written by me, with help from ML.

## Related papers not included in the thesis

### Paper 10

M. Kildemo, L. M. S. Aas, P. G. Ellingsen, H. Hemmen, E. L. Hansen, and J. O. Fossum, “Mueller matrix imaging of nematic textures in colloidal dispersions of Na-fluorohectorite synthetic clay,” in *Proc. SPIE*, P. H. Lehmann, W. Osten, and K. Gastinger, Eds., **8082**, 808221–808221–8 (2011)

This paper demonstrates the use of Mueller matrix imaging on a colloid. It shows the spatial ordering of clay.

### Paper 11

M. Kildemo, J. Maria, P. G. Ellingsen, and L. M. S. Aas, “Parametric model of the Mueller matrix of a Spectralon white reflectance standard deduced by polar decomposition techniques,” *Opt. Express* **21**(15), 1071–1086 (2013)

This paper demonstrates the use of Mueller matrix ellipsometric scattering data together with decomposition methods for parametric modeling the Spectralon reference sample.

### Paper 12

L. M. S. Aas, D. G. Skåre, P. G. Ellingsen, P. A. Letnes, and M. Kildemo, “Design, optimization and realization of a ferroelectric liquid crystal based Mueller matrix ellipsometer using a genetic algorithm,” *Thin Solid Films* **In press** (2014)

This paper demonstrates the design, optimization and realisation of a FLC based Mueller matrix ellipsometer.

### **Paper 13**

S. Nyström, K. M. Psonka-Antonczyk, P. G. Ellingsen, L. B. G. Johansson, N. Reitan, S. Handrick, S. Prokop, F. L. Heppner, B. M. Wegenast-Braun, M. Jucker, M. Lindgren, B. T. Stokke, P. Hammarström, and K. P. R. Nilsson, “Evidence for age-dependent in vivo conformational rearrangement within A $\beta$  amyloid deposits,” *ACS Chem. Biol.* **8**, 1128–33 (2013)

This is the paper published before paper 8 as a part of the LUPAS EU-project. It was the first to show a rearrangement of the A $\beta$  plaques over time.

### **Paper 14**

T. Kindahl, P. G. Ellingsen, C. Lopes, C. Brännlund, M. Lindgren, and B. Eliasson, “Photophysical and DFT characterization of novel Pt(II)-coupled 2,5-diaryloxazoles for nonlinear optical absorption,” *J. Phys. Chem. A* **116**, 11519–30 (2012)

This paper shows the synthesis and characterisation of platinum(II) complexes. The characterisation is done both with photophysical characterisation and density functional theory calculations.

# Contents

<b>Abstract</b>	<b>i</b>
<b>Preface</b>	<b>iii</b>
<b>List of papers</b>	<b>v</b>
<b>1. Introduction</b>	<b>1</b>
<b>2. Background and Theory</b>	<b>3</b>
2.1. On light . . . . .	3
2.2. Polarised light . . . . .	4
2.2.1. Stokes formalism . . . . .	5
2.2.2. The Mueller matrix . . . . .	6
2.2.3. Forward polar decomposition . . . . .	6
2.2.4. Differential decomposition . . . . .	7
2.2.5. Polarisation changing materials and properties . . . . .	8
2.3. Spectroscopy . . . . .	10
2.3.1. Light - molecule interactions . . . . .	11
2.3.2. Fluorescence spectroscopy . . . . .	12
2.3.3. Raman spectroscopy . . . . .	14
<b>3. Methods and results</b>	<b>15</b>
3.1. Mueller matrix imaging . . . . .	15
3.1.1. Experimental Mueller matrix imaging setup . . . . .	15
3.1.2. Overview of results from MMI . . . . .	16
3.1.3. Retardance imaging of strain . . . . .	19
3.1.4. Collagen fibres in biological tissue . . . . .	20
3.2. Spectroscopic characterisation . . . . .	22
3.2.1. Hyperspectral fluorescence imaging . . . . .	22
3.2.2. Time gated Raman spectroscopy . . . . .	26
<b>4. Summary</b>	<b>31</b>
4.1. Conclusion . . . . .	31
4.2. Possible future work . . . . .	32
<b>Bibliography</b>	<b>42</b>

*Contents*

<b>A. Excited state absorption</b>	<b>43</b>
A.1. Background and theory . . . . .	43
A.2. Methods and result . . . . .	45
<b>B. Papers</b>	<b>47</b>
Paper 1 . . . . .	49
Paper 2 . . . . .	61
Paper 3 . . . . .	73
Paper 4 . . . . .	83
Paper 5 . . . . .	99
Paper 6 . . . . .	107
Paper 7 . . . . .	115
Paper 8 . . . . .	121
Paper 9 . . . . .	129

# 1. Introduction

*“The difference between screwing around and science is writing it down.”*

— Adam Savage

The study of how light interacts with our surroundings is something which defines us as humans. Ever since the first spearfishers discovered that catching the fish required them to throw their spears below it, we have known that light interacts with our surroundings in a peculiar way. Today we know that the effect, that the fishermen discovered, is due to the refraction of light, mathematically explained by Snell’s law. Even if it is fully understood today, the “breaking” of a pencil by the water surface, as illustrated in figure 1.1, is a fascinating effect.



Figure 1.1.: The “breaking” of a pencil by a water surface.

There are a lot of other phenomena arising from the fundamental properties of light, many of which are famous and spectacular. My personal favourites are the rainbow, the red sunset and the polarisation of the blue sky. At first glance the rainbow is a result of the splitting of all the wavelengths in sunlight, due to dispersion in the raindrops [15, 16]. By looking further into the rainbow and all the effects related to it, we have discovered that some of the effects are not so easily explained. Explaining these requires the

## 1. Introduction

study of the wave nature of light and how it scatters on particles [16, 17]. The scattering of light is also responsible for the beautiful colours at sunset and the blue sky [18]. In addition to the colours, the blue sky is polarised, meaning that the electromagnetic waves oscillate in a non random direction. Polarisation is one of the fundamental properties of light which, together with its wavelength, will be studied here.

One of the aims of the work presented here was to study known interactions between polarised light and the structure of biological samples [19–28], and nanomaterials [29–32] as part of collaborations with other research groups. This was to be achieved by using and improving a newly developed system for measuring the polarisation altering properties of a sample [31, 33, 34]. In addition to improving the setup step by step, a secondary objective was to develop computer software for more robust and precise optical design. Initially, the software was to be based on searching all possible solutions, however during the work, it instead became based upon algorithms for optimisation developed in the field of artificial intelligence [35].

Another aim of the work was to employ and develop different spectroscopy techniques, known to be suited for application on biomedical and nanomaterial samples [36–45]. These projects were to rely on the collaboration with international research groups, one of which was an EU project in the seventh framework program, namely the LUPAS (Luminescent Polymers for in vivo imaging of Amyloid Signatures) project. In studying amyloid samples, a new system for carrying out hyperspectral fluorescence microscopy was to be used, requiring implementation and development of new image analysis software.

Another spectroscopy technique to be developed was a time gated Raman spectrometer. The technique should use a newly acquired state of the art monochromator with an ICCD, together with a pulsed laser. It was to solve some of the problems related to luminescence dominating the Raman signal [46, 47]. In addition, it should enable the detection of resonance Raman by using UV excitation [48].

In order to present the results from the aims, chapter 2, briefly describes the background and theory laying the foundations for the work presented. It will include the theory for polarisation and spectroscopy. Following this, chapter 3 will give an overview of the different experimental setups, the system design and optimisation, as well as selected results from the work published during the thesis. Chapter 4 will summarise the thesis in a conclusion and present possible continuations of the work presented here. Appendix A includes a presentation of an unpublished setup for doing excited state absorption (ESA) and is included mostly as a reference for possible future ESA setups. Lastly, appendix B includes the papers which are part of this thesis.



## 2. Background and Theory

*“We are just an advanced breed of monkeys on a minor planet of a very average star. But we can understand the Universe. That makes us something very special.”*

— Stephen Hawking

As Stephen Hawking points out, we are capable of understanding (parts of) the Universe. In doing so, we have developed different theories and tried to prove them wrong by employing the scientific method. New theories are based upon accepted theories, which have stood up to rigorous tests and predicted experiment outcomes. In such a way, we are building our tree of knowledge. It is this tree that the work presented here was aimed at adding a tiny branch to. In order to do so, the work builds upon work done by scientists before me, especially advances done on manipulation and detection of light.

This chapter briefly explains the background and theory for the work presented in the thesis. It will not be an extensive explanation of the theory, as there are a number of good books going in depth on the theory, like for example the books in references [49–52]. Furthermore, theory explained satisfactorily in the included papers will not be repeated here.

### 2.1. On light

When reading this text you are most likely looking at it with your eyes. If that is the case, you will be observing photons that have either been emitted by a screen or reflected off the paper. These photons are quanta of the electromagnetic field. The electromagnetic field describes not only light, but also x-rays, radio waves, etc. In order for us to see light, it must have a wavelength (denoted as  $\lambda$ ) in the range 380 nm to 750 nm. Wavelength is one of the fundamental properties of the electromagnetic field, the others being amplitude, phase, direction of propagation and direction of oscillation, known as polarisation. All of these properties are of interest for studying and observing our surroundings.

## 2. Background and Theory

### 2.2. Polarised light

As humans we can not, under most circumstances, see what polarisation is. The exception being for instance Haidinger's brushes [53]. In contrast, some insects (bees, ants, crickets, ...) have the ability to observe the difference between different polarisation states of light [54]. Understanding how it is possible to see the differences, requires us to define what polarisation is. As already mentioned, polarisation is the direction of the electric field oscillation in electromagnetic waves. Electromagnetic waves, as most commonly defined, are transverse waves. Consequently, the oscillation is in the plane normal to the direction of the propagation, see figure 2.1. This plane can then be used to describe polarisation, by tracing how the wave intersects it over time. Since the field oscillates with a harmonic motion, the only possible path for the polarisation is an ellipse, with the special cases of a line and a circle. The ellipse is known as the polarisation ellipse and can be seen in figure 2.1.

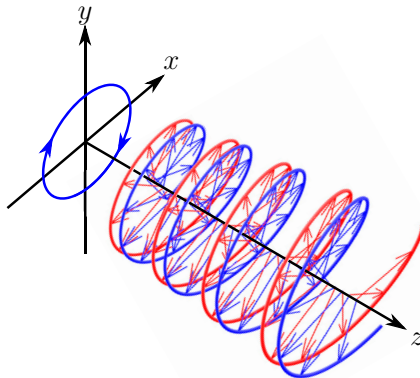


Figure 2.1.: Figure showing the electric (blue) and magnetic (red) parts of an elliptically polarised electromagnetic wave. Furthermore the coordinate system and the polarisation ellipse for right elliptical light is shown. The  $z$ -axis points away from the source.

In the general description, there is the possibility for longitudinal polarisation, where (part of) the electromagnetic wave is longitudinal [55, 56]. It requires radially polarised beams and was believed to only be achieved over a few wavelengths [55] in distance, however, recently there was published a

design for several tens of thousands of wavelengths [57]. The beam has some desirable properties, amongst others no divergence. A beam with no divergence can be used to achieve better focusing in high-resolution imaging [56]. The case of longitudinal electromagnetic waves is a special case, and will not be discussed any more in this thesis.

### 2.2.1. Stokes formalism

Having now understood what polarisation is, it is useful to quantify it. One convenient way of quantifying it is to use the Stokes formalism. First we define the electric field as a monochromatic plane wave traveling in the  $z$ -direction [49, 58]

$$\mathbf{E}(z, t) = \mathbf{E}_0 e^{i(\omega t - kz)} = \text{Re} \left\{ E_{x0} e^{i(\omega t - kz + \delta_x)} \right\} \hat{x} + \text{Re} \left\{ E_{y0} e^{i(\omega t - kz + \delta_y)} \right\} \hat{y}, \quad (2.1)$$

where  $\mathbf{E}_0$  is the time dependent electric field amplitude,  $\omega$  is the angular frequency,  $t$  the time,  $k = 2\pi/\lambda$  the wave vector and  $\hat{x}$  and  $\hat{y}$  the unit vectors in the  $x$  and  $y$  directions. See figure 2.1 for the definition of the coordinate system.  $E_{x0}$  is the time dependent electric field amplitude in the  $x$  direction,  $E_{y0}$  the time dependent electric field amplitude in the  $y$  direction, and  $\delta_x$  and  $\delta_y$  are their phases.

Using the field described in equation (2.1), it is possible to define the Stokes vector as [50, 58]

$$\mathbf{S} = \begin{bmatrix} s_0 \\ s_1 \\ s_2 \\ s_3 \end{bmatrix} = \begin{bmatrix} \langle E_{x0}^2 \rangle + \langle E_{y0}^2 \rangle \\ \langle E_{x0}^2 \rangle - \langle E_{y0}^2 \rangle \\ 2\langle E_{x0} E_{y0} \rangle \cos \delta \\ 2\langle E_{x0} E_{y0} \rangle \sin \delta \end{bmatrix}, \quad (2.2)$$

with  $\delta = \delta_y - \delta_x$  describing the phase difference between the two components of the electric fields.  $\langle \rangle$  denotes time averages. The first component of the Stokes vector,  $s_0$ , is the total intensity of the light.  $s_1$  describes the amount of linearly horizontally ( $x$ -direction) or vertically polarised ( $y$ -direction) light. The  $s_2$  component is similar to  $s_1$ , as it describes the amount of linear polarised light at  $\pm 45^\circ$ . Finally, the  $s_3$  component is the amount of left or right circular polarised light. The first three components of the Stokes vector ( $s_0, s_1, s_2$ ) can all be measured using a linear polariser, while the last component relates the left and right circular polarisation, and therefore requires a wave plate to be measured.

It is here worth noting that there are two possible ways of defining right and left circular polarisation. In the work presented here the definition from Hauge et al. [58] will be used. It defines right circular polarisation as a clockwise

## 2. Background and Theory

rotation of the electric field when looking towards the source, see figure 2.1.

The Stokes vector is one way of describing polarisation of light. Another common way of describing it is through the Jones vector, it is a two-vector with the  $x$  component of the electric field  $E_x = E_{x0}e^{i\delta_x}$  as the first element and the  $y$  component of the electric field  $E_y = E_{y0}e^{i\delta_y}$  as the second. Compared to the real Stokes vector, the Jones vector is a complex vector that describes the phase of the electric field. However, since it can only describe fully polarised light, it is not of that much interest for the work presented here, since the samples studied are all partially depolarising. In comparison, the Stokes vector is a real vector that can be used to describe unpolarised light, though it does not describe the absolute phase.

### 2.2.2. The Mueller matrix

Once the Stokes vector (equation (2.2)) has been defined, it is advantageous to define a transformation matrix for it, describing its interaction with matter. This transformation matrix is known as the Mueller matrix,  $\mathbf{M}$ , and is a  $4 \times 4$  real matrix. Since the Stokes vector can describe depolarised light, the Mueller matrix describes, in addition to other properties of a sample, depolarising effects. The Mueller matrix for air (diag[1, 1, 1, 1]) and other simple optical components can easily be recognised, see subsection 2.2.5, though if the system becomes more complex, like for instance turbid media (biological tissue), or scattering media (rough surfaces), it is insightful to use Mueller matrix decomposition techniques. From these it is easier to extract the physical properties of the sample, for example birefringence, optical rotation and depolarisation. There are several ways of doing a matrix decomposition, but the main ones used in this thesis is the forward polar decomposition developed by Lu and Chipman [59] and the differential decomposition originally proposed by Azzam [60]. These will be presented in the ensuing subsections.

### 2.2.3. Forward polar decomposition

The forward polar decomposition, developed by Lu and Chipman [59], has been the most widely used method for decomposing Mueller matrices. It decomposes the Mueller matrix into three different Mueller matrices via

$$\mathbf{M} = \mathbf{M}_\Delta \mathbf{M}_R \mathbf{M}_D, \quad (2.3)$$

where  $\mathbf{M}_\Delta$  is the depolarisation matrix,  $\mathbf{M}_R$  is the retardance matrix and  $\mathbf{M}_D$  the diattenuation matrix.

After decomposing the measured Mueller matrices, it is convenient to further calculate the properties of a sample by various models. One way of calculating the properties is using the equations derived by Manhas et al. [61].

Examples of the properties one then gets, is the direction of the fast axis of the linear retardance  $\theta$ , the optical rotation  $\psi$  and the linear retardance  $\delta$ . These quantities can further be used to understand the structure to property relationships in a sample.

The forward polar decomposition in equation 2.3, is only one of six possible permutations of the  $\mathbf{M}_\Delta$ ,  $\mathbf{M}_R$  and  $\mathbf{M}_D$  matrices [62,63]. These permutations are grouped into the forward polar decomposition with the depolarisation ( $\mathbf{M}_\Delta$ ) assumed to occur after diattenuation ( $\mathbf{M}_D$ ), and the reverse with the opposite order. The permutation of the forward polar decomposition given in equation (2.3), is the one most commonly used and the one used in the work presented here.

#### 2.2.4. Differential decomposition

The forward polar decomposition and the permutations, assume that the polarisation effects are sequential, which is only correct for some samples. For instance, most biological tissue is turbid in its nature [24], resulting in the polarisation effects occurring simultaneously. As a consequence, either the parameters in the forward polar decomposition can be modified as explained by Kumar et al. [64], or another decomposition method is needed. One of the methods that can decompose simultaneous effects is the differential decomposition, first proposed by Azzam for Jones matrices [60], and further refined to Mueller matrices by Ossikovski [65] and Kumar et al. [64].

The differential decomposition method decomposes the Mueller matrix by taking its matrix logarithm

$$\mathbf{L} = \ln \mathbf{M} = \mathbf{m}l,$$

where  $\mathbf{m}$  is the differential matrix and  $l$  the path length through the sample.  $\mathbf{m}$  contains the polarisation properties of the sample per unit length. From  $\mathbf{L}$  it is now possible to construct two matrices describing the material properties

$$\begin{aligned} \mathbf{L} &= \mathbf{L}_m + \mathbf{L}_u, \\ \mathbf{L}_m &= \frac{1}{2} (\mathbf{L} - \mathbf{G}\mathbf{L}^T\mathbf{G}), \\ \mathbf{L}_u &= \frac{1}{2} (\mathbf{L} + \mathbf{G}\mathbf{L}^T\mathbf{G}), \end{aligned}$$

where  $G$  is the Minkowski metric tensor,  $\text{diag}[1, -1, -1, -1]$ . The properties of the sample can be found from  $\mathbf{L}_m$  and  $\mathbf{L}_u$ , where  $\mathbf{L}_m$  will result in the properties themselves and  $\mathbf{L}_u$  the depolarisation and uncertainty (standard deviation) in the properties. The uncertainty is a result of the randomness in the sample. Properties that one can calculate from  $\mathbf{L}_m$  and  $\mathbf{L}_u$  are the same

## 2. Background and Theory

as for the forward polar decomposition, though some of them depend on  $l$ , see Kumar et al. [64] and paper 6.

### 2.2.5. Polarisation changing materials and properties

Having now described how characteristic properties of a material can be calculated from the Mueller matrix, it is interesting to look at what causes these properties. The most interesting properties with respect to the work presented here are depolarisation, linear retardance (birefringence), direction of the fast axis of the linear retardance and optical rotation. Depolarisation is an effect that arises from several different processes. It describes how much of the incoming polarised light is lost and/or converted to non-polarised light. One way this occurs is through multiple scattering of the light by particles in the sample, resulting in an averaging effect (with respect to both time and space). Similarly, the summing of differently polarised light intensities on a detector element results in depolarisation. The depolarisation on a detector element can be a problem in certain imaging setups, as it is not caused by the sample itself. Biological tissue samples are generally turbid media and therefore polarised light experiences a significant amount of depolarisation when propagating through it. Depolarisation can be calculated without doing a decomposition, as described by Gil et al. [66]. though mostly the depolarisation found from the decomposition will be used here.

Linear retardance is induced by different refractive indices along different axes in a medium. If two of the axes have the same refractive index, different from the third, it is known as an uniaxial medium. A well known example of an uniaxial system is a wave plate. When all of the axes have different refractive indices, it is known as a biaxial medium. An example of a biaxial system is a chiral liquid crystal [67]. If the electromagnetic wave propagates along one of the two ordinary axes in a uniaxial system, it induces a phase shift between the electric field components

$$\delta = \frac{2\pi l \Delta n}{\lambda} \quad (2.4)$$

where  $l$  is the thickness of the wave plate and  $\Delta n = n_e - n_o$  the difference in refractive index along the extraordinary axis,  $n_e$ , and the ordinary axis,  $n_o$ .

It is not only homogeneous systems, e.g. a wave plate, which have different diffusion properties in different directions, resulting in birefringence. Liquid crystals, where elongated macromolecules in liquid exhibit crystal-like behaviour, are well known birefringent media. The orientation of the molecules is controlled by surface alignment and electromagnetic fields. These crystals are for example used in displays for mobile phones, TVs and computer screens. Some of these use an electrically controlled liquid crystal, sandwiched between

two crossed polarisers, to generate and display the image. In order to explain how these liquid crystals change the incoming polarisation, one has to use effective medium theories like the Bruggeman effective medium model [67]. This model assumes that the particles are smaller than the wavelength of the incoming light. It predicts that if the particles have a difference in shape along at least two directions, an example would be a cylinder, they will give rise to an effective form birefringence. In section 3.1 this way of modeling the properties will be applied to collagen fibres, which are long fibres embedded in a tissue. They have a different refractive index compared to the surrounding tissue, and as a consequence they give rise to a form birefringence.

An additional property that can be found from the Mueller matrix of a birefringent medium, is the direction of the fast axis of the linear retardance. The direction describes the axis of the ordinary refractive index in the plane perpendicular to the direction of propagation. Depending on the sample, this axis or the slow axis, also known as the axis of the extraordinary refractive index (assuming  $n_e > n_o$ ), can be combined with effective medium modeling to determine the direction of the particles responsible for the linear retardance. As described in paper 5, this is the case for collagen fibres in tissue, where the long axis of the the fibres corresponds to the slow axis of the linear retardance, due to the higher refractive index of the collagen fibres compared to the surrounding medium.

The last property of the Mueller matrix being discussed here, is the optical rotation. It describes the rotation of linear polarised light around the axis of light propagation [26, 61]. Physically it arises from the chirality (mirror symmetry, like your hands) of molecules or structures [68]. It is normally a weak effect requiring sensitive techniques for detection. Several different biological molecules exhibit chirality [69], including glucose [26, 70].

## 2. Background and Theory

### 2.3. Spectroscopy

As light is something we see all the time, we rarely stop and think about how we see light, how it interacts with matter around us and how it is emitted. An example of a light phenomena is the northern lights (aurora), see figure 2.2, where high energy electrons from the sun excite ionised oxygen and nitrogen in our upper atmosphere. These excited atoms and molecules then emit light when they relax to the ground state. The colour of the light is specific to a given molecule, with the single-atomic form of oxygen emits the green and the high altitude red, while nitrogen emits low altitude red and a purple [71–73]. By measuring the wavelength of the light using spectroscopy and comparing it to references, it is possible to identify the molecule or atom from where the light originated. In order to understand the emission of light, we have to first look at how light interacts with molecules. Thereafter we can look at different ways this interaction occurs and how we measure it with spectroscopy.



Figure 2.2.: "Green and red northern lights" by Jerome Maria. <https://flic.kr/p/bihrwg>



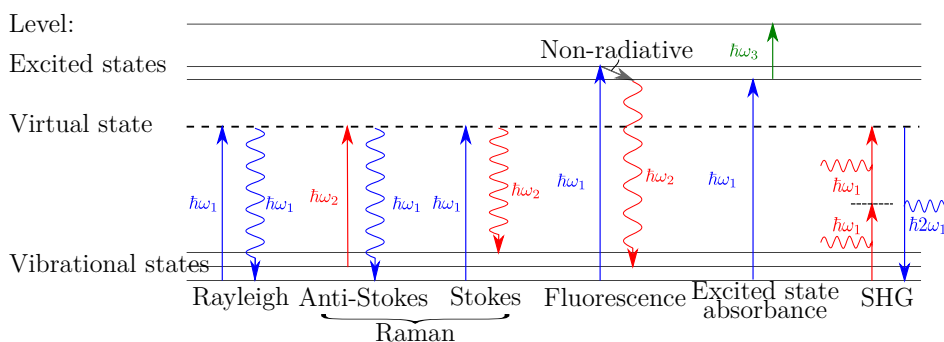


Figure 2.3.: Jablonski diagram of excitation and emission processes for certain spectroscopy techniques. In the figure  $\omega_1 > \omega_2$ . The decay in the excited state of the fluorescence (gray arrow) is a non-radiative decay.

### 2.3.1. Light - molecule interactions

A photon can be absorbed and/or reemitted by the electrons of an atom or molecule. There are several different ways for this to occur, some of which are shown in figure 2.3. Whether an effect is described as a scattering effect or an absorptive effect depends on the lifetime of the electronic state. For instance, virtual states are “forbidden” states in quantum mechanics, i.e., they are not energy eigenstates of the molecule or atom. Since they are “forbidden”, the lifetime is short ( $\ll 1$  ps [47]) enough that the scattering can be thought of as instantaneous. If the photon is absorbed to an energy eigenstate, which usually has a much longer lifetime, it is recognised as an absorption process.

Figure 2.3 shows both scattering and absorption effects. The linear scattering effects are known as Rayleigh and Raman scattering, respectively. Rayleigh scattering is an elastic scattering process where the energy of the photon is unchanged. Raman scattering is an inelastic scattering process where the photon either is emitted with higher energy, known as anti-Stokes scattering, or lower energy, known as Stokes scattering. As anti-Stokes scattering requires the molecule or atom to be in a higher vibrational state than the ground state, it is less likely to occur compared to Stokes scattering.

Another effect presented in figure 2.3 is fluorescence, which is an absorption to an excited state followed by a deexcitation with the emission of a photon. The emitted photon will have a lower energy than the excitation photon in most cases, due to the non-radiative decay, though it is possible to get higher energy photons if the excitation is from a higher vibrational state compared to the emission end state. Also shown in the figure, is the absorption of another photon from the excited state to a higher excited state, known as an

## 2. Background and Theory

excited state absorption (ESA). ESA will be discussed in appendix A. The last process shown is second harmonic generation (SHG), where two photons are absorbed at the same time and a single photon with twice the energy is emitted. This is a second order nonlinear scattering process, meaning that the intensity of the scattering is proportional with the square of the incoming intensity, as well as having a short lifetime.

Outside of the effects presented in figure 2.3, there are many other ways to excite or deexcite an atom or molecule. For excitation, this includes electroluminescence (light emitting diode (LED) [74]), chemiluminescence and bioluminescence (glow sticks [75, 76] and fireflies [77]), particle interactions (northern lights [71–73]) and nonlinear optical effects like four wave mixing processes (e.g. coherent anti-Raman spectroscopy [78–80]). In case of a de-excitation, the same is possible with the energy being transferred in chemical reactions (laser burns), phonon excitation (heating of the sample), and the photovoltaic effect, where a semiconductor, e.g. a solar cell or CCD, captures the excited electron and converts it into an electric current.

### 2.3.2. Fluorescence spectroscopy

The goal of carrying out optical spectroscopy, which comprises of measuring intensity as a function of wavelength, is to characterise and understand the sample. There are a range of different techniques for performing optical spectroscopy, all with their different uses and requirements for the optical setup.

Fluorescence is a well known process, first discovered by Sir John Frederick William Herschel in 1845, when studying an acidic solution containing quinine using light from a window [81]. He observed blue light upon viewing the solution perpendicular to the direction of sunlight. After the discovery of fluorescence, it has become a useful tool, from the use of fluorescent dyes poured into the water, to demonstrate that the rivers Danube and Rhine were connected via underground streams in 1877, to today's single molecule detection techniques [39]. Single molecule detection is possible as a consequence of the high quantum yield present in fluorescent dyes. Quantum yield is a measure of the number of emitted photons per absorbed photon [39]. In medical sciences, fluorescence is a common tool, due to the possibility of selectively staining certain parts of a cell or specific proteins, enabling imaging of amongst others cell membranes, amyloids and DNA [39, 41].

Fluorescence spectroscopy involves measuring the emission spectrum from a sample, under excitation of either a single wavelength, such as a laser, or a narrow wavelength range, for example a LED or lamp with an optical band pass filter. When exciting a molecule or atom, there is only a certain range of wavelengths that correspond to an excited state. This range is known

### 2.3. Spectroscopy

as the excitation spectrum of the sample. The resulting emission from a given excitation is a broad range of wavelengths. Figure 2.4 shows a 2D scan of the emission and excitation from pFTAA stained amyloid insulin. The figure shows typical spectra, where the spectrum consisting of one or more broad features. These features make it harder to distinguish several different molecules from each other if they are mixed together. One way of distinguishing the molecules is to use statistical methods and unmixing techniques, which will be discussed in section 3.2.

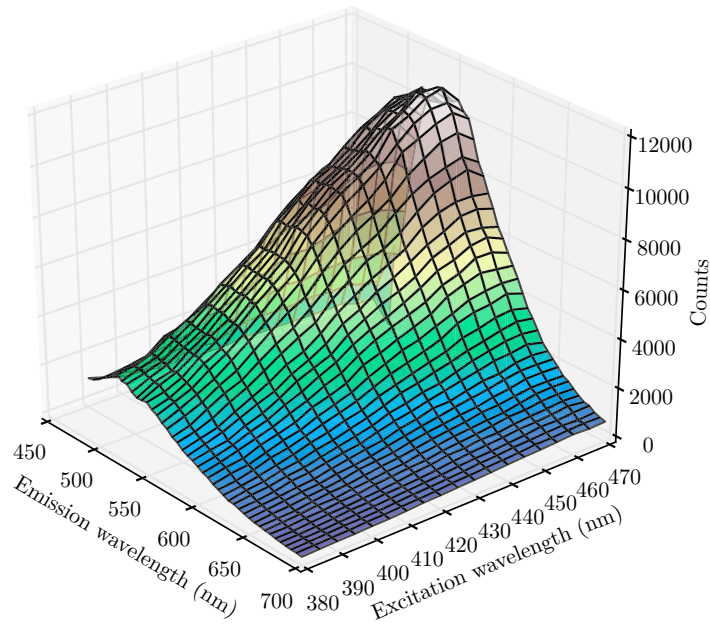


Figure 2.4.: Excitation and emission (fluorescence) spectra for pFTAA stained amyloid insulin fibrils. The data from the figure is from Psonka-Antonczyk et al. [82].

## 2. Background and Theory

### 2.3.3. Raman spectroscopy

Raman scattering was first observed in 1928 by C.V. Raman [36]. Since its discovery it has become a useful technique for characterising molecules. Compared to fluorescence spectroscopy, Raman spectroscopy can be used to fingerprint a molecule without the need for staining, making it easier to separate out different molecules. The reason that Raman spectra can be regarded as fingerprints is that the vibrational levels will result in a formation of narrow spectral peaks, with a discrete nature, see figure 3.8. As the excitation is normally performed by a monochromatic laser, the broadening of the peaks due to the excitation is small. Due to being an inelastic scattering effect, it is a weak effect, orders of magnitude weaker than for example fluorescence. Raman scattering is a linear effect with respect to the intensity, though it scales as the fourth order of the excitation frequency [37, 83]. If the excitation is to an excited state, instead of a “virtual state”, it results in a resonance with the electronic transition. [48]. It is likely to happen in the UV, where it is known as UV resonance Raman. The resonance can also be characterised as a much larger Raman cross section [48], and has an enhancement factor as large as  $10^8$ .

UV Raman resonance is not the only way to increase the Raman signal. It is possible to increase it by exploiting plasmonic effects. These effects can be surface-enhanced Raman spectroscopy (SERS) [37, 84] or nonlinear optical processes driving the Raman signal between different transitions. Examples of nonlinear processes are stimulated Raman spectroscopy and Coherent anti-Stokes Raman spectroscopy [78–80].

## 3. Methods and results

*“Strap a piece of toast -battered side up- to the back of a cat. Throw the cat out of the window. Will the cat land on its feet or will Murphy’s law apply?”*

— Alan Fletcher, *The Art of Looking Sideways*

The established background and theory will now be applied to experimental setups in order to study silicon-, bio- and nanomaterials. Different materials require specific techniques in order to investigate certain properties. As the presented work was conducted on a variety of samples, different methods have been required to study them. As a consequence, this chapter will be split between the different techniques. Under each measurement technique the experimental setup is explained, together with a selection of the core results found during the work.

### 3.1. Mueller matrix imaging

Measurement of the polarisation properties of a given material can be done in a range of ways, from the simple crossed polarisers, popular in biomedical microscopy, to ellipsometry (thin film industry [67, 85]) and polarimetry (astronomy [86–88]), where retarding elements are used to modulate the incoming and/or outgoing polarisation. The work presented here was done on a custom built Mueller matrix imaging (MMI) ellipsometer. This setup was used to study the structure of biological tissue sections, since these structures were known to change the incoming polarisation [69].

#### 3.1.1. Experimental Mueller matrix imaging setup

The Mueller matrix imaging setup was developed over several years and published by Ladstein et al. [33] and in papers 3, 4, 5 and 6. In addition, it has been the subject of two doctoral theses [31, 89]. Only a brief description of the setup will be given here. For the details see the given references. Currently the setup consists of a LED source (either a 940 nm LED or a 1300 nm LED), a polarisation state generator (PSG), a filter wheel with calibration

### 3. Methods and results

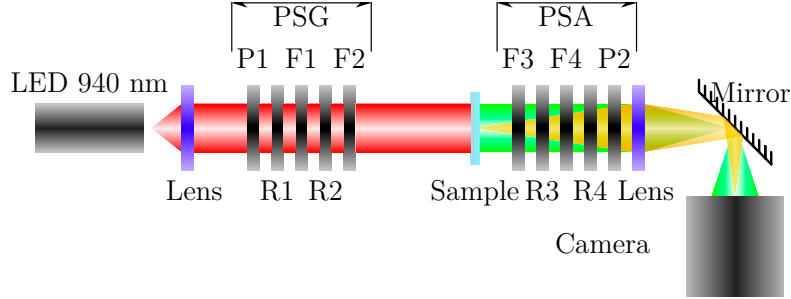


Figure 3.1.: The Mueller matrix imaging setup. Here R stands for retarder, P for polariser and F for FLC. When used in the NIR, a flip mirror (not shown) is used to change the source to a 1300 nm LED. Another flip mirror is used to change the camera to an InGaAs camera. The filter wheel with the calibration samples (not shown) is placed after the PSG, before the sample.

samples, a polarisation state analyser (PSA) and a camera (either a silicon or an InGaAs camera). The PSG and PSA, which each generate/analyse four different Stokes vectors, both consist of a polariser, two ferroelectric liquid crystals (FLCs) and two wave plates, as presented in figure 3.1. The calibration is done using air, a vertical polariser, a horizontal polariser and a zero order wave plate, together with the eigenvalue calibration method (ECM) proposed by Compain et al. [90].

The sample is mounted on a motorised stage, capable of moving in the horizontal and vertical image plane, enabling acquisition of large areas by stitching images together, as demonstrated by Kildemo et al. [10]. When doing 3D directional imaging the samples were placed on a motorized rotation stage, such that the angle of incidence upon the sample could be changed. The details of the rotation setup can be found in paper 6.

#### 3.1.2. Overview of results from MMI

The MMI setup was, and is, a good setup for doing experiments, with a large range of possibilities for modifications and tailoring for special samples. As a consequence, it has produced results for a range of different samples. The main ones found during the work presented here are related to the optimisation of Mueller matrix polarimeters, imaging of strain in multicrystalline silicon and collagen fibres embedded in biological tissue. Included in these results are the development and implementation of state of the art data analysis methods. This includes decomposition methods and the 3D directional imaging used to image collagen fibre directions in tendon. In addition, imaging of colloidal

clay solutions was done by Kildemo et al. [10]. It will not be discussed here.

#### **Genetic algorithms for optimisation of broadband polarimeters**

As mentioned earlier, a Mueller matrix ellipsometer consists of a polarisation state generator (PSG) and a polarisation state analyser (PSA). When building such a system, it is typical to use the same components in the PSG and the PSA, just with inverse ordering in the PSA compared to the PSG, see figure 3.1. A polarimeter is just the PSA on its own, used to measure the Stokes vector, or parts of the Stokes vector, for the incoming light. An optimal polarimeter can be quantified by the condition number of the system matrix, see paper 1. In the designs we have been studying, the components are a polariser, two or more wave plates and two or more liquid crystals. The liquid crystals can change their state according to the applied voltage. For FLCs, the change is between two discrete states, while for liquid crystal variable retarders (LCVRs) the retardance can be changed continuously between a maximum and minimum by adjusting the applied voltage.

As wave plates and liquid crystals all have retardance dispersion, and a broadband system is desired, the optimisation of the number of components, their thickness and orientation is nontrivial, spanning a search space that can contain more than  $10^{12}$  solutions. Traditional optimisation algorithms are hard to use, both due to the size of the search space and the number of local minima present in the search space (see Aas et al. [12] for a figure showing two dimensions in the search space). Previous solutions have included qualified guesses, that sometimes have then been run through local gradient searches in order to maximise the condition number [33, 91]. As a solution, we choose to use genetic algorithms, see paper 1 and Aas et al. [12], which use evolutionary processes [35], like mutation, breeding and competition to find the best solution. Coding of the algorithm was done in Python using the open source library Pyevolve [92]. Solutions are evaluated with respect to minimising the inverse condition number of the system. The best inverse condition number that can be achieved by such a system is  $1/\sqrt{3}$  and it can be used to calculate the noise propagation in the system [34, 93, 94]. Due to the nature of the genetic algorithm, it is not possible to know if the solution is the global minimum, though we found the solutions to be good. Compared to a commercial instruments, (MM16, Horiba Ltd., 2006), see figure 3.2 and Aas et al. [12], the designed system had a wider spectral coverage and a significantly higher inverse condition number. Another design was demonstrated to be better than the setup we were using, presented in figure 3.2.

### 3. Methods and results

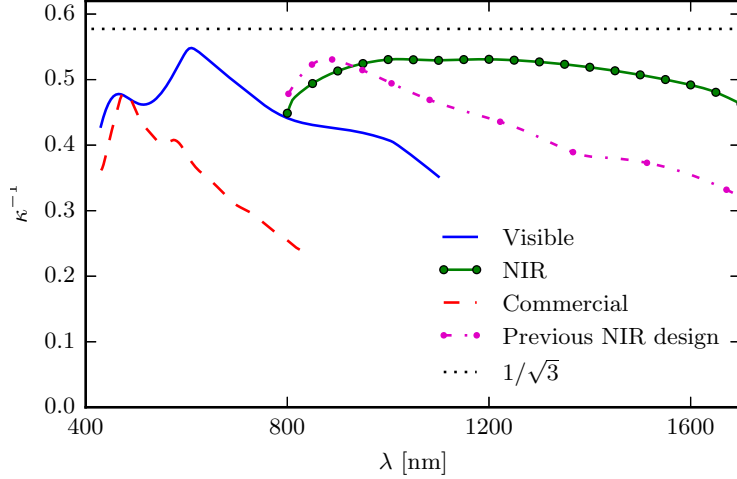


Figure 3.2.: Two different 2 FLC designs compared to a commercial (MM16, Horiba, 2006) system and a previous design used in the MMI system [33]. Figure redrawn from paper 1.

#### Overdetermined polarimeter

Due to dispersion effects present in most optical components, there is a limit to how broad a polarimeter it is possible to design with 4 states in the PSA/PSG. Something which can be amended by adding more states in the PSA/PSG, and thereby oversampling the Mueller matrix. Additionally, the mathematics for the calibration and inversion of the system must then be reworked. In a Mueller matrix ellipsometer, the  $\mathbf{W}$  and  $\mathbf{A}$  matrices, which characterise the PSG and the PSA, are used to calculate the measured Mueller matrix,  $\mathbf{M}$  from the intensity measurements  $\mathbf{B}$  made by the detector via

$$\mathbf{M} = \mathbf{A}^{-1}\mathbf{B}\mathbf{W}^{-1}.$$

In an overdetermined system, the  $\mathbf{W}$  and  $\mathbf{A}$  matrices are non-square, and therefore one needs to use the Moore-Penrose pseudoinverse [95] method for inverting the matrices. This was done in paper 1 and by Aas et al. [12], where a 3 FLC overdetermined polarimeter with a broad spectral range of 430 nm to 2000 nm was optimised.

When implementing an overdetermined system, it is necessary to modify the ECM calibration method [90]. Such a modification is presented in paper 2, which in addition includes an experimental verification on a 2 LCVR (with  $2 \times 3$  states) setup. The paper shows that the correspondence between the optimised system found by the genetic algorithm, using the measured dis-



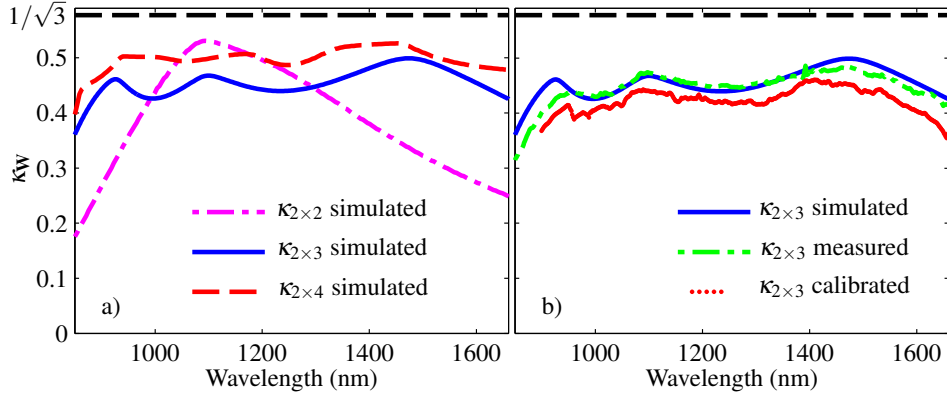


Figure 3.3.: Inverse generalised condition number of  $\mathbf{W}$ . In (a) it is shown for different number of states in two LCVRs and in (b) the comparison between the designed, measured and calibrated  $2 \times 3$  system is shown. Figure from paper 2.

person relation for each LCVR, and the implemented setup is good, as can be seen in figure 3.3. This system has a broad spectral range covering the range of an InGaAs camera, making it useful for imaging for instance silicon in transmission. It is significantly slower than the FLC system, due to the time it takes to switch the LCVRs and more than twice the number of states ( $6 \times 6 = 36$  versus  $4 \times 4 = 16$  states), but it has good optical transmission due to the reduced number of optical surfaces compared to a 3 FLC system, see Aas et al. [12]. In addition, it is compact and easier to adjust to different applications, because the voltage levels can be reoptimised without the need to rotate the components.

### 3.1.3. Retardance imaging of strain

Production of solar cells from multicrystalline silicon has become a global industry with large investments and large production quantities. In the production, the margins are being squeezed all the time, and as a consequence the yield should be as high as possible. One of the larger losses in production is breakage due to residual strain in multicrystalline wafers. If one were able to sort out the potential weak wafers at an earlier stage in the production, the losses from breakage could be reduced. Paper 4 presents the Mueller matrix imaging setup based upon FLCs and uses it to image the strain field in a multicrystalline silicon wafer. The basis for the paper is that the strain fields are proportional to the retardance measured in the sample [96].

The results in paper 4 present both the magnitude of the strain, in terms

### 3. Methods and results

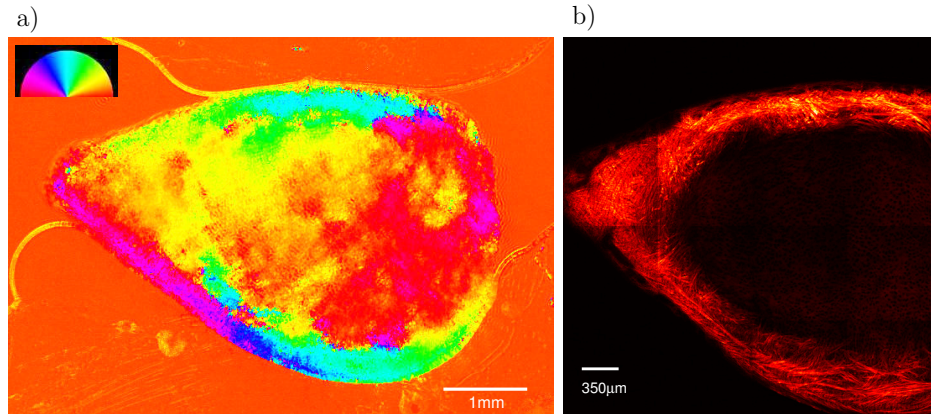


Figure 3.4.: a) Visualisation of the direction of the slow axis for collagen fibres in cartilage. The colour wheel indicates the direction of the fibres. b) SHG image of the same area. Figures from paper 5.

of the retardance, and its direction. Calculation of the direction from the linear retardance is done with the method that was used for collagen fibres, as presented in the next subsection. Being able to image the strain helps give input to numeric models simulating the grain boundaries and the strain present there. Furthermore, it should be possible to refine the technique for potential use in quality control for solar cell production lines.

#### 3.1.4. Collagen fibres in biological tissue

A main focus in the work presented here was the imaging of the directions of collagen fibres in different biological tissue. Imaging of the directions is, as described in paper 5, possible by modeling the collagen fibres as an uniaxial effective medium, with the slow axis along the fibre direction. The direction of the fast axis (perpendicular to the slow axis) is a result in both decomposition methods (forward polar decomposition, subsection 2.2.3, and differential decomposition, subsection 2.2.4), and gives a direct measurement of the direction of the collagen fibres within a pixel, as demonstrated in paper 5.

After successfully finding the direction of the collagen fibres in chicken articular cartilage, using forward polar decomposition, and comparing with SHG images, see figure 3.4, the method was further developed by using the differential decomposition and rotation of the sample, enabling the characterisation of the 3D direction of the collagen fibres, see paper 6. The method uses two images, taken at different angles of incidence (similar to how we observe the world with our eyes), to calculate the direction of the collagen fibres. The re-

### 3.1. Mueller matrix imaging

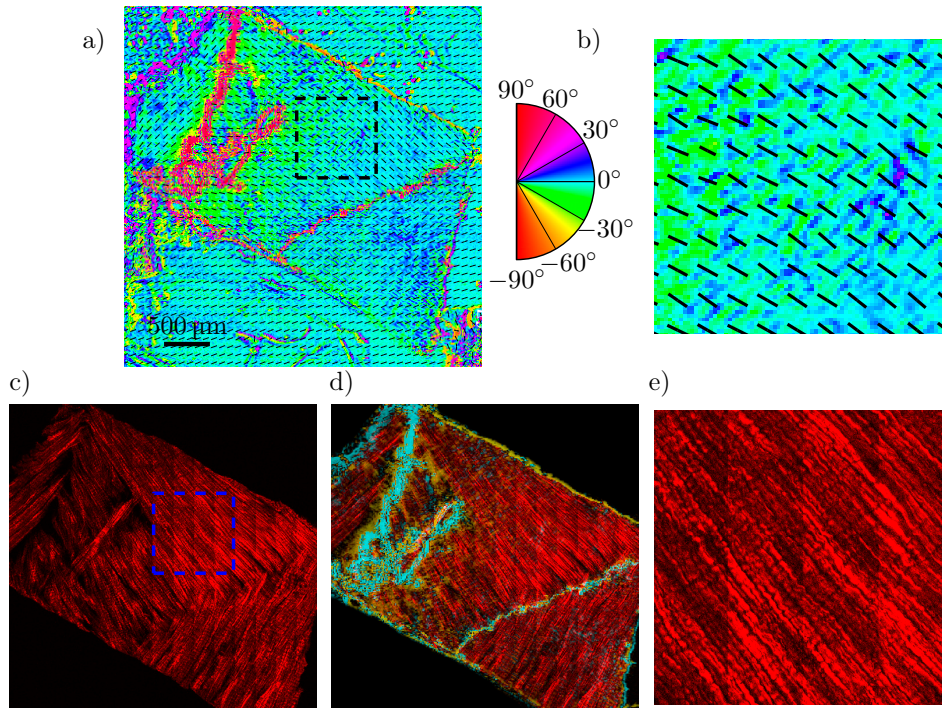


Figure 3.5.: 3D directional image (a) with a zoomed view (b), a SHG image (c) with a zoomed in view (e) and an overlay of the SHG and the out of plane direction of the tendon (d). The colourwheel beside the directional image shows the out of plane direction in degrees, with  $0^\circ$  being in the image plane and  $\pm 90^\circ$  normal to the image plane.  $+90^\circ$  is the direction towards the reader (positive  $x$ ). The overlay (d) (area outside of the sample masked for clarity) shows the SHG and out of plane directions overlain. The yellow colour represent the negative out of plane direction and the cyan the positive direction. No colour represents an in plane direction and increasing colour more out of plane. Figure from paper 6

### 3. *Methods and results*

sulting 3D direction of the collagen fibres, this time in tendon, was compared with SHG images. Such a comparison can be seen in figure 3.5. Differential decomposition, which was not available for paper 5, was used as it is much better at decomposing simultaneous occurring polarisation effects, compared to the forward polar decomposition. The 3D direction method works well on the collagen fibres in tendon and is envisaged to work well on other birefringent media, like for instance liquid crystals, multicrystalline silicon and other tissue containing collagen.

## 3.2. Spectroscopic characterisation

Polarisation is good at characterising the structure and physical properties of some samples, however for a lot of samples, polarisation sensitive techniques are not the best way of characterisation. This section will explain the work done with techniques for measuring the spectral response of the samples as a result of an excitation. The techniques will be hyperspectral fluorescence imaging (biological tissue) and Raman spectroscopy (nanomaterials and liquids). In addition to these techniques, a new way of analysing spectral data, the correlation analysis, will be presented. The correlation analysis was developed for the hyperspectral fluorescence imaging, yet it was successfully applied to Raman spectroscopy.

### 3.2.1. Hyperspectral fluorescence imaging

As described in the theory section, subsection 2.3.2, fluorescence spectroscopy is suitable for characterising biological samples. A hyperspectral fluorescence microscope was used to characterise the amyloid plaques studied here. It consisted of a standard fluorescence microscope from Leica equipped with a xenon lamp together with filters for excitation and filtering the emission. Mounted on top of the microscope was a hyperspectral camera from Applied Spectral Imaging. The hyperspectral camera is based upon a Sagnac interferometer, which is a common path interferometer [97]. Difference in path length, and thereby different interference fringes, is achieved by changing the angles travelled by the two light beams through the system. By scanning the angle, and recording the resulting interference pattern on the CCD, it is possible to calculate the wavelength spectrum in each pixel, via an inverse Fourier transform. Such an interferometer is different to the push broom [98, 99], in that the area of acquisition is given by the field of view, and not by how far you scan the line.

The main results, from the hyperspectral microscope and a similar one at Linköping University, are related to the LUPAS (Luminescent Polymers for in vivo imaging of Amyloid Signatures) project, which was an European union

### 3.2. Spectroscopic characterisation

project within the Seventh Framework Programme. One of the project goals was to study the progression of Alzheimer's in mice using new luminescent polymers. Specifically, this was done by imaging brain sections from mice, stained with two different luminescent polymers, qFTAA and hFTAA. It was established that these bind to different parts of the amyloid plaque, Nyström et al. [13], enabling the study of the change in microscopic structure. These changes were smaller than the resolution of the microscope and they were found using the spectral correlation analysis.

#### Spectral correlation analysis

In fluorescence spectroscopy, it is often a problem that the measured spectrum is a combination of several spectra. These spectra can be from autofluorescence and staining dyes. Methods used to unmix the spectra are for example linear spectral unmixing [100–103] and principal component analysis (PCA) [104]. Both of these methods have drawbacks. Linear spectral unmixing (LSU) assumes that the mixed spectrum is a linear combination of a set of reference spectra. Requirements for LSU are that the background needs to be removed and that the signal has a high signal-to-noise ratio. It does not take into account nonlinear effects. In PCA, reference spectra are not used. Instead it finds an orthogonal set of basis spectra. These basis spectra can be hard to relate to a specific source, as each of them can be a combination of several features, each from a different dye/source. For the amyloid plaques the signal was weak and it was advantageous not having to remove the background. As a consequence of the limitations for both LSU and PCA, a new method was developed.

From radar technology [105, 106] it is well known that it is possible to detect a signal in large amounts of noise by calculating the correlation coefficient between the reference pulse sent out and the returned signal. The correlation coefficient is given by [107]

$$\rho_{XY} = \frac{\sigma_{XY}}{\sigma_X \sigma_Y} \quad (3.1)$$

where  $X$  and  $Y$  are random variables,  $\sigma_{XY}$  the covariance between  $X$  and  $Y$ , and  $\sigma_X, \sigma_Y$  the standard deviations for  $X$  and  $Y$ , respectively. The power in the correlation method comes from the fact that it does not need any normalisation of the variables, due to the division by the standard deviation. In addition, the coefficient is limited to values in the interval  $-1 \leq \rho_{XY} \leq 1$ , where 1 corresponds to ( $Y = X$ ) and  $-1$  to  $Y = -X$ . The limit on the coefficient means that it is possible to do statistics on coefficients from different data sets.

The correlation method was found useful for separating signals in hyper-

### 3. Methods and results

spectral data, from either fluorescence or Raman spectroscopy. For spectral data it is calculated as

$$\rho_{XY} = \frac{\sum_{i=1}^N (X_i - \bar{X})(Y_i - \bar{Y})}{\sqrt{\sum_{i=1}^N (X_i - \bar{X})^2} \sqrt{\sum_{i=1}^N (Y_i - \bar{Y})^2}} \quad (3.2)$$

where  $X$  and  $Y$  are the two spectra, one from a pixel in the image or measurement and the other from a reference.  $\bar{X}, \bar{Y}$  are the mean values of the spectra, and  $N$  the number of data points in the spectrum. If comparing with more than one reference spectrum, like in papers 8 and 9, the calculation is repeated for every reference spectrum, and the resulting correlation values or images are compared. An example from paper 8 can be seen in figure 3.6. Figure 3.6 a) shows the intensity, and figure 3.6 b) shows the correlation with qFTAA and hFTAA. All the figures have been thresholded at 3500 counts, coloured as dark blue, to remove the background.

Figure 3.6 clearly reveals that the two stains bind to two different areas of the plaque. As a consequence, these two stains could be used to study the change in the microstructure over time, by looking at mice sacrificed at different ages, see Nyström et al. [13] and paper 8. Nyström et al. [13] used a comparison of spectra intensities at given wavelengths to distinguish the two probes. In paper 8, the correlation analysis is used in combination with an automated method for finding the centre of the plaques. This made it possible to calculate statistics over a normalised radial distance. Normalised radial distance was used as the plaques are all of different sizes. Statistical analysis revealed that the plaques continuously undergo structural changes, even after the structure can not be seen to change using wide field microscopy. The change was previously unreported, though the causes of it are not yet fully understood, as the goal of the experiment was to test the co-staining of these two new oligothiophenes, together with the hyperspectral analysis.

### 3.2. Spectroscopic characterisation

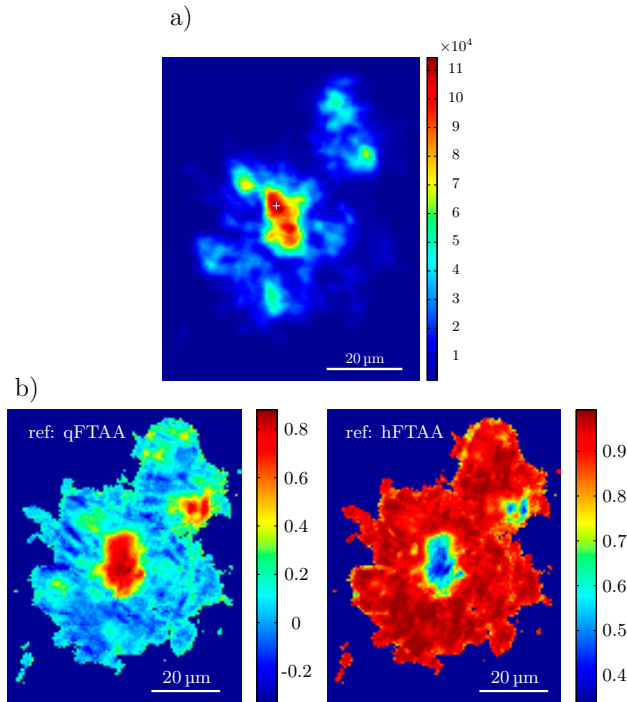


Figure 3.6.: a) Intensity image (sum over all wavelengths) for an amyloid plaque from a mouse. The white plus sign in the figure marks the center used for analysing the correlation values as a function of the radius. Colour scale is in counts. b) Two images showing the correlation between the qFTAA (left) or hFTAA (right) reference and the measured spectrum. Dark blue areas are masked using a) and a threshold of 3500 counts. The colour scale is here the correlation coefficient. The figures are from paper 8.

### 3. Methods and results

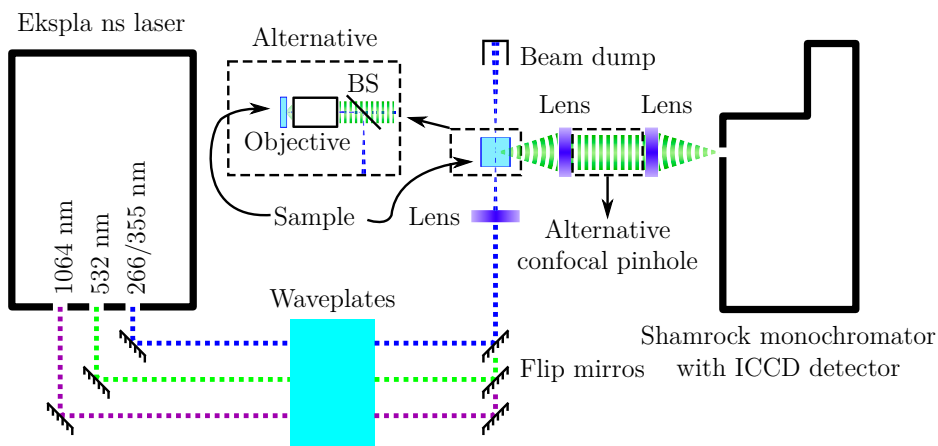


Figure 3.7.: Schematic drawing of the time-gated Raman setup. It shows two different configurations of the system. BS stands for beam splitter. The triggering connection between the laser and the ICCD detector is not shown. Also not shown, is the computer controlling the monochromator and the ICCD camera. The figure is from paper 9.

#### 3.2.2. Time gated Raman spectroscopy

In Raman spectroscopy, phosphorescence and fluorescence sometimes dominates the Raman signal. There are several ways for remedying this. One can for example use more excitation power and thereby burn out the fluorescence, or one can change the excitation wavelength. These are changes done with the acquisition parameters, but it is also possible to do baseline subtraction in post processing of the results [108, 109]. All of these methods have problems. Increasing the excitation power is not a possibility for all samples, as it will burn some of them. Changing wavelength requires the system to be equipped for excitation and detection at several different wavelength ranges, complicating the system. Baseline fitting requires the signal to noise ratio of the Raman signal to be strong enough for the resulting spectrum to be discernible. Furthermore, baseline fitting can induce spectral artifacts [108]. In trying to solve several of these problems we designed and built our own system for suppressing phosphorescence and long lifetime fluorescence by time gating the signal. The system, shown in figure 3.7, is based on a pulsed Nd:YAG laser and a monochromator with an ICCD. The Nd:YAG laser is an Ekspla laser with a pulse width of 2 ns, a repetition rate adjustable between 10 Hz and 55 Hz, and a pulse energy of 0.5 mJ to 2 mJ, depending on the harmonic used. By changing the nonlinear crystals it is possible to choose between out-



### 3.2. Spectroscopic characterisation

put wavelengths of 1024 nm, 532 nm, 355 nm and 266 nm. Originally it was not possible to adjust the output pulse energy from the laser, nevertheless it was made possible by inserting a motorised rotator on the wave plate situated prior to the harmonic crystals. By rotating the wave plate, the coupling efficiency in the crystals is changed, and by that the pulse energy. The system is described in paper 9.

Time gating in the Raman system is done by the Andor ICCD. An ICCD has an electric field in front of the phosphor coupled CCD that amplifies electrons from the photocathode. As it is an electric field, it is possible to switch the amplification on and off with less than a 2 ns gate width, enabling precise gating of the signal. In addition, the electric field allows for adjustment of the amplification level up to  $\approx 10000\times$ . The ICCD is UV enhanced, enabling detection of wavelengths from 180 nm to 850 nm. Furthermore, by thresholding above the dark count of the CCD and counting a signal above as a photon, it is possible to do photon counting. The advantage of photon counting is that it removes the need for background subtraction. For dispersing the wavelengths across the ICCD, a Shamrock monochromator is used. It is a monochromator with a focal length of 500 mm equipped with notch filters for the removing the Rayleigh line, and three different gratings.

The optical setup for the excitation of the sample, see figure 3.7, consists of wave plates for controlling the polarisation, flip mirrors, a lens or alternatively an objective and a beam splitter made from a glass slide for excitation. On the detection side of the setup, it is possible to use a 200  $\mu\text{m}$  pinhole, making the detection confocal. A confocal detection means that the signal detected arises from a small volume in the sample, limiting the amount of background noise and signal from other parts of the sample and the surroundings [83,110]. The objective is a normal long working distance 32 $\times$  objective, meaning that it will not transmit light below 350 nm.

#### **Calibration of the Raman system**

Calibration of the Raman instrument is done by using spectroscopic grade cyclohexane as a reference. Cyclohexane is chosen as a reference, based upon the ATSM (American Society for Testing and Materials) 2007 standard [111]. The mapping from measured wavelength to actual wavelength is done in post processing in a custom Python script. By selecting the measured peaks and comparing them to the actual peak positions from the standard, it is possible to fit a polynomial to the conversion from measured wavelengths to actual wavelengths. The calibration is done after each measurement series, with the same acquisition properties, as the different gratings/excitation wavelength and their position change the mapping.

### 3. Methods and results

#### Results from the Raman system

Paper 9 presents the main results found using the time-gated Raman setup. These include a proof of principle, where a long lifetime luminescence is gated away from a Raman spectra using a Pt-acetylide chromophore abbreviated Z3 [112] dissolved in tetrahydrofuran (THF) and degassed. Degassing, by freeze-thawing (with liquid nitrogen) under vacuum, was done to remove quenching of the luminescence due to dissolved oxygen. The results are presented in figure 3.8. As the figure reveals, the short gate width of 5 ns removes

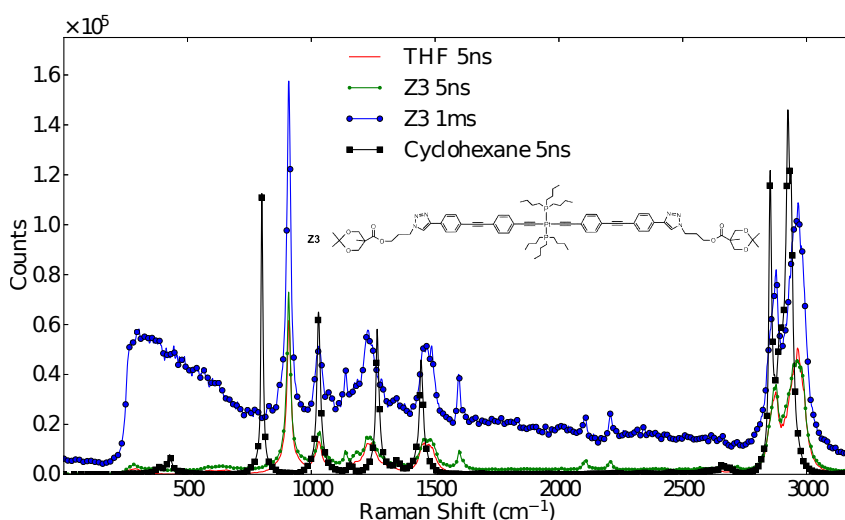


Figure 3.8.: Measured Raman spectra for THF and Z3 dissolved in THF, at excitation of 532 nm. The cyclohexane spectrum was used to calibrate the wavelength and is shown for reference. Z3 was measured with a both a 5 ns gate and a 1 ms gate in order to assess the advantage of the time gate. In addition, the chemical structure of Z3 is shown. The figure is from paper 9.

the luminescence seen in the 1 ms spectrum. The spectra were recorded with the same settings, but since the ICCD does not reach maximum amplification for short gate widths, the Raman peaks have different heights for the different gate widths. This then establishes that the system is capable of removing luminescence with longer lifetime than the minimum gate width of 2 ns.

Another result presented in paper 9, is the UV resonance Raman effect for cyclohexane. It is tested by exciting cyclohexane with the different harmonics

### 3.2. Spectroscopic characterisation

available in the setup. As expected from [113, 114], and the scaling of the Raman scattering with wavelength, the signal becomes significantly stronger the further one moves into the UV. As a consequence, the signal to noise ratio becomes better and it is easier to acquire a good spectrum.

The last result presented in paper 9, is the application of the spectral correlation analysis, explained in subsection 3.2.1, to Raman spectra. The method was originally developed for analysing hyperspectral fluorescence images, papers 7 and 8, however due to its characteristics (good noise tolerance, no need for normalisation and statistical nature) it was tested for analysing Raman spectra. As paper 9 demonstrates, it was possible to distinguish volume fractions of THF in water of  $\approx 1/1000$  with the maximum number of counts in the spectrum being  $\approx 1000$ . It is envisaged that this could be useful for analysing hyperspectral Raman images and for detecting trace substances in chemical mixtures.



## 4. Summary

*“It seems to me that the natural world is the greatest source of excitement; the greatest source of visual beauty; the greatest source of intellectual interest. It is the greatest source of so much in life that makes life worth living.”*

— David Attenborough

In this thesis several fields have been studied, using different techniques, all with a common framework of polarimetry and spectroscopy. As a result of the diverse number of problems and collaborations, the work was able to combine knowledge from different fields into new methods for characterising interesting effects. The conclusions of these will be presented below, however personally the most interesting part is what the work done here can lead to in future work.

### 4.1. Conclusion

Biomedical and nanoscale research is a field in rapid growth, where techniques are developed and improved continuously. In this thesis several new methods for data analysis have been presented, in addition to improvements to known techniques. Firstly, Mueller matrix imaging has been improved upon, by designing an enhanced broadband system, which propagates less noise and covers a larger spectral area. Such a system was implemented and tested using liquid crystals variable retarders. The development of the setup required an extension of the eigenvalue calibration method.

Using a Mueller matrix imaging setup, based on ferroelectric liquid crystals, collagen fibres in tendon and cartilage were studied by applying effective medium modeling and stereoscopic techniques to map the orientation of the fibres in the tissue. This type of technique can be useful when modeling collagen fibres, as well as studying injuries related to structural changes in the collagen. Furthermore, the technique is believed to have applications in other effective media and crystals. For the two-dimensional case, the method was tested on strain imaging of a multicrystalline silicon wafer.

#### 4. Summary

Additionally, work was done on developing spectroscopic techniques, where an instrument for time gated Raman spectroscopy was designed and implemented. The time gated Raman spectrometer enabled reduction of luminescence by gating the Raman scattering from pulsed excitation. In addition, the instrument enabled UV resonance Raman spectroscopy.

Lastly a spectral correlation method was developed and tested on hyperspectral fluorescence images of double stained amyloid plaques from mice. The method was demonstrated to solve several of the major problems with other unmixing techniques, including the need for normalisation and background removal. It was further suitable for doing statistical analyses, due to self normalisation, making it easier to compare different samples.

### 4.2. Possible future work

The work presented here has resulted in some interesting findings, but as always in life, there is something new and interesting just beyond the horizon. Only by exploring the world will you discover it, but remember to bring a map, as it contains prior knowledge, which makes it less likely that you will find yourself utterly lost.

Several areas are left unexplored during the work presented here. For instance, the application of Mueller matrix imaging is still in its infancy, with its full potential not yet known. One field left for exploration is wide field microscopy, which is used for studying biophysical problems. In addition, the method for finding 3D directions should be applicable to thin film materials, as well as the characterisation of 3D plasmonic materials and metamaterials.

With the current development of fast imaging spectrometers and high power (pulsed) lasers, the field of Raman spectroscopy is experiencing a renaissance with respect to identifying and studying chemicals, biological material and solid state materials. Here the step from doing spectroscopy, into doing hyperspectral Raman microscopy is one that carries an advantage. This has already been done commercially by amongst others Renishaw plc, Horiba Ltd., WITec GmbH and Nanophoton Corp., but the techniques used here for suppression of luminescence could still be of importance in these new systems.

With the development of new hyperspectral techniques, the amount of recorded data is growing at a rapid rate. Understanding the data requires more and more use of automated software for the analysis. In this respect, the correlation method developed here definitely has uses within spectroscopy, where it gives an easy way of getting statistical numbers for the images. Possible extensions of the method is the application to larger sets of references and the automatic comparison of correlation coefficients. One interesting use will be in the field of hyperspectral Raman imaging where the method should be able to distinguish small spectral differences in noisy signals.

## Bibliography

- [1] P. A. Letnes, I. S. Nerbø, L. M. S. Aas, P. G. Ellingsen, and M. Kildemo, “Fast and optimal broad-band Stokes/Mueller polarimeter design by the use of a genetic algorithm,” *Opt. Express* **18**, 10 (2010).
- [2] L. M. S. Aas, P. G. Ellingsen, B. E. Fladmark, P. A. Letnes, and M. Kildemo, “Overdetermined broadband spectroscopic Mueller matrix polarimeter designed by genetic algorithms,” *Opt. Express* **21**, 8753 – 8762 (2013).
- [3] L. M. S. Aas, P. G. Ellingsen, M. Kildemo, and M. Lindgren, “Dynamic response of a fast near infra-red Mueller matrix ellipsometer,” *J. Mod. Opt.* **57**(17), 1603–1610 (2010).
- [4] L. M. S. Aas, P. G. Ellingsen, and M. Kildemo, “Near infra-red Mueller matrix imaging system and application to retardance imaging of strain,” *Thin Solid Films* **519**, 2737–2741 (2011).
- [5] P. G. Ellingsen, M. B. Lilledahl, L. M. S. Aas, C. D. L. Davies, and M. Kildemo, “Quantitative characterization of articular cartilage using Mueller matrix imaging and multiphoton microscopy,” *J. Biomed. Opt.* **16**, 116002 (2011).
- [6] P. G. Ellingsen, L. M. S. Aas, V. S. Hagen, R. Kumar, M. B. Lilledahl, and M. Kildemo, “Mueller matrix three-dimensional directional imaging of collagen fibers,” *J. Biomed. Opt.* **19**, 26002 (2014).
- [7] P. G. Ellingsen, N. K. Reitan, B. D. Pedersen, and M. Lindgren, “Hyperspectral analysis using the correlation between image and reference,” *J. Biomed. Opt.* **18**, 20501 (2013).
- [8] P. G. Ellingsen, S. Nyström, N. K. Reitan, and M. Lindgren, “Spectral correlation analysis of amyloid  $\beta$  plaque inhomogeneity from double staining experiments,” *J. Biomed. Opt.* **18**, 101313 (2013).
- [9] P. G. Ellingsen and M. Lindgren, “Design and test of a Raman spectroscopic system based on a time-gated intensified CCD,” *Submitt. to Opt. Express* *4. June 2014* (2014).

## Bibliography

- [10] M. Kildemo, L. M. S. Aas, P. G. Ellingsen, H. Hemmen, E. L. Hansen, and J. O. Fossum, "Mueller matrix imaging of nematic textures in colloidal dispersions of Na-fluorohectorite synthetic clay," in *Proc. SPIE*, P. H. Lehmann, W. Osten, and K. Gasteringer, Eds., **8082**, 808221–808221–8 (2011).
- [11] M. Kildemo, J. Maria, P. G. Ellingsen, and L. M. S. Aas, "Parametric model of the Mueller matrix of a Spectralon white reflectance standard deduced by polar decomposition techniques," *Opt. Express* **21**(15), 1071–1086 (2013).
- [12] L. M. S. Aas, D. G. Skåre, P. G. Ellingsen, P. A. Letnes, and M. Kildemo, "Design, optimization and realization of a ferroelectric liquid crystal based Mueller matrix ellipsometer using a genetic algorithm," *Thin Solid Films* **In press** (2014).
- [13] S. Nyström, K. M. Psonka-Antonczyk, P. G. Ellingsen, L. B. G. Johansson, N. Reitan, S. Handrick, S. Prokop, F. L. Heppner, B. M. Wegenast-Braun, M. Jucker, M. Lindgren, B. T. Stokke, P. Hammarström, and K. P. R. Nilsson, "Evidence for age-dependent in vivo conformational rearrangement within A $\beta$  amyloid deposits," *ACS Chem. Biol.* **8**, 1128–33 (2013).
- [14] T. Kindahl, P. G. Ellingsen, C. Lopes, C. Brännlund, M. Lindgren, and B. Eliasson, "Photophysical and DFT characterization of novel Pt(II)-coupled 2,5-diaryloxazoles for nonlinear optical absorption," *J. Phys. Chem. A* **116**, 11519–30 (2012).
- [15] R. J. Whitaker, "Physics of the Rainbow," *Phys. Teach.* **12**(5), 283 (1974).
- [16] L. Cowley, "Atmospheric Optics - Rainbows." <http://www.atoptics.co.uk/bows.htm> visited 18.03.2014.
- [17] R. L. Lee, "Mie Theory, Airy Theory, and the Natural Rainbow," *Appl. Opt.* **37**, 1506 (1998).
- [18] E. Hecht, *Optics*, Addison Wesley, 4th ed. (2002).
- [19] A. Hielscher, A. Eick, J. Mourant, D. Shen, J. Freyer, and I. Bigio, "Diffuse backscattering Mueller matrices of highly scattering media," *Opt. Express* **1**, 441 (1997).
- [20] S. L. Jacques, J. R. Roman, and K. Lee, "Imaging superficial tissues with polarized light," *Lasers Surg. Med.* **26**, 119–29 (2000).



- [21] S. L. Jacques, J. C. Ramella-Roman, and K. Lee, “Imaging skin pathology with polarized light,” *J. Biomed. Opt.* **7**, 329 (2002).
- [22] J. S. Baba, J.-R. Chung, A. H. DeLaughter, B. D. Cameron, and G. L. Coté, “Development and calibration of an automated Mueller matrix polarization imaging system,” *J. Biomed. Opt.* **7**, 341–9 (2002).
- [23] B. Laude-Boulesteix, A. De Martino, B. Drévilion, and L. Schwartz, “Mueller polarimetric imaging system with liquid crystals,” *Appl. Opt.* **43**, 2824–2832 (2004).
- [24] V. V. Tuchin, *Tissue optics: light scattering methods and instruments for medical diagnosis*, SPIE Press, Bellingham, WA, 2nd ed. (2007).
- [25] J. Chung, W. Jung, M. J. Hammer-Wilson, P. Wilder-Smith, and Z. Chen, “Use of polar decomposition for the diagnosis of oral precancer,” *Appl. Opt.* **46**, 3038–45 (2007).
- [26] N. Ghosh, M. F. G. Wood, and I. A. Vitkin, “Mueller matrix decomposition for extraction of individual polarization parameters from complex turbid media exhibiting multiple scattering, optical activity, and linear birefringence,” *J. Biomed. Opt.* **13**(4), 044036 (2008).
- [27] N. Ghosh, M. F. G. Wood, S. Li, R. D. Weisel, B. C. Wilson, R. Li, and I. A. Vitkin, “Mueller matrix decomposition for polarized light assessment of biological tissues,” *J. Biophotonics* **2**(3), 145–56 (2009).
- [28] M.-R. Antonelli, A. Pierangelo, T. Novikova, P. Validire, A. Benali, B. Gayet, and A. De Martino, “Mueller matrix imaging of human colon tissue for cancer diagnostics: how Monte Carlo modeling can help in the interpretation of experimental data,” *Opt. Express* **18**, 10200 (2010).
- [29] I. S. Nerbø, M. Kildemo, S. Le Roy, I. Simonsen, E. Søndergård, L. Holt, and J. C. Walmsley, “Characterization of nanostructured GaSb: comparison between large-area optical and local direct microscopic techniques,” *Appl. Opt.* **47**, 5130–9 (2008).
- [30] M. Richert, X. Orlik, and A. De Martino, “Adapted polarization state contrast image,” *Opt. Express* **17**(16), 14199–14210 (2009).
- [31] F. Stabo-Eeg, *Development of instrumentation for Mueller matrix ellipsometry*. Doctoral thesis, NTNU (2009).
- [32] I. S. Nerbø, S. Le Roy, M. Foldyna, M. Kildemo, and E. Søndergård, “Characterization of inclined GaSb nanopillars by Mueller matrix ellipsometry,” *J. Appl. Phys.* **108**(1), 014307 (2010).

## Bibliography

- [33] J. Ladstein, F. Stabo-Eeg, E. Garcia-Caurel, and M. Kildemo, “Fast near-infra-red spectroscopic Mueller matrix ellipsometer based on ferroelectric liquid crystal retarders,” *Phys. Status Solidi* **5**(5), 1097–1100 (2008).
- [34] F. Stabo-Eeg, J. Ladstein, and M. Kildemo, “Product decomposition of measured Mueller matrices from the FLC based NIR Mueller Matrix Ellipsometer,” *Phys. Status Solidi* **5**(5), 1093–1096 (2008).
- [35] S. Nolfi and D. Floreano, *Evolutionary Robotics: The Biology, Intelligence, and Technology of Self-Organizing Machines*, MIT press (2004).
- [36] C. V. Raman and K. S. Krishnan, “A new type of secondary radiation,” *Nature* **121**, 501–502 (1928).
- [37] I. Lewis and H. Edwards, *Handbook of Raman spectroscopy: from the research laboratory to the process line*, CRC Press (2001).
- [38] R. a. Schultz, T. Nielsen, J. R. Zavaleta, R. Ruch, R. Wyatt, and H. R. Garner, “Hyperspectral imaging: a novel approach for microscopic analysis,” *Cytometry* **43**, 239–47 (2001).
- [39] J. R. Lakowicz, *Principles of Fluorescence Spectroscopy*, Springer US, Boston, MA (2006).
- [40] K. P. R. Nilsson, P. Hammarström, F. Ahlgren, A. Herland, E. a. Schnell, M. Lindgren, G. T. Westermark, and O. Inganäs, “Conjugated polyelectrolytes–conformation-sensitive optical probes for staining and characterization of amyloid deposits,” *Chembiochem* **7**, 1096–104 (2006).
- [41] K. P. R. Nilsson, A. Åslund, I. Berg, S. Nyström, P. Konradsson, A. Herland, O. Inganäs, F. Stabo-Eeg, M. Lindgren, G. T. Westermark, L. Lanfolt, L. N. G. Nilsson, and P. Hammarström, “Imaging distinct conformational states of amyloid-beta fibrils in Alzheimer’s disease using novel luminescent probes,” *ACS Chem. Biol.* **2**, 553–60 (2007).
- [42] A. Åslund, C. J. Sigurdson, T. Klingstedt, S. Grathwohl, T. Bolmont, D. L. Dickstein, E. Glimsdal, S. Prokop, M. Lindgren, P. Konradsson, D. M. Holtzman, P. R. Hof, F. L. Heppner, S. Gandy, M. Jucker, A. Aguzzi, P. Hammarström, and K. P. R. Nilsson, “Novel pentameric thiophene derivatives for in vitro and in vivo optical imaging of a plethora of protein aggregates in cerebral amyloidoses,” *ACS Chem. Biol.* **4**, 673–84 (2009).

- [43] F. Stabo-Eeg, M. Lindgren, K. P. R. Nilsson, O. Inganäs, and P. Hammarström, “Quantum efficiency and two-photon absorption cross-section of conjugated polyelectrolytes used for protein conformation measurements with applications on amyloid structures,” *Chem. Phys.* **336**, 121–126 (2007).
- [44] M. Gaft and L. Nagli, “UV gated Raman spectroscopy for standoff detection of explosives,” *Opt. Mater. (Amst)*. **30**, 1739–1746 (2008).
- [45] A. Åslund, K. P. R. Nilsson, and P. Konradsson, “Fluorescent oligo and poly-thiophenes and their utilization for recording biological events of diverse origin-when organic chemistry meets biology,” *J. Chem. Biol.* **2**, 161–75 (2009).
- [46] P. Matousek, M. Towrie, C. Ma, W. M. Kwok, D. Phillips, W. T. Toner, and a. W. Parker, “Fluorescence suppression in resonance Raman spectroscopy using a high-performance picosecond Kerr gate,” *J. Raman Spectrosc.* **32**, 983–988 (2001).
- [47] N. Everall, T. A. S. Hahn, P. M. Atousek, and A. W. Parker, “Picosecond Time-Resolved Raman Spectroscopy of Solids: Capabilities and Limitations for Fluorescence Rejection and the Influence of Diffuse Reflectance,” **55**(12), 1701–1708 (2001).
- [48] S. A. Asher, “UV resonance Raman spectroscopy for analytical, physical, and biophysical chemistry. Part 1,” *Anal. Chem.* **65**, 59A–66A (1993).
- [49] D. J. Griffiths, *Introduction to Electrodynamics*, Pearson Education, 3rd ed. (2008).
- [50] D. Goldstein, *Polarized light*, Marcel Dekker, Inc., 2nd ed. (2003).
- [51] C. Foot, *Atomic Physics*, OUP Oxford (2005).
- [52] H. Goldstein, C. Poole, and J. Safko, *Classical Mechanics*, Addison Wesley, San Francisco, CA, 3rd ed. (2002).
- [53] G. P. Misson, “A Mueller matrix model of Haidinger’s brushes,” *Ophthalmic Physiol. Opt.* **23**, 441–447 (2003).
- [54] T. Labhart and E. P. Meyer, “Detectors for polarized skylight in insects: a survey of ommatidial specializations in the dorsal rim area of the compound eye,” *Microsc. Res. Tech.* **47**, 368–79 (1999).

## Bibliography

- [55] H. Wang, L. Shi, B. Lukyanchuk, C. Sheppard, and C. T. Chong, "Creation of a needle of longitudinally polarized light in vacuum using binary optics," *Nat. Photonics* **2**, 501–505 (2008).
- [56] Q. Zhan, "Cylindrical vector beams: from mathematical concepts to applications," *Adv. Opt. Photonics* **1**, 1 (2009).
- [57] M. Zhu, Q. Cao, and H. Gao, "Creation of a  $50,000\lambda$  long needle-like field with  $0.36\lambda$  width," *J. Opt. Soc. Am. A. Opt. Image Sci. Vis.* **31**, 500–4 (2014).
- [58] P. S. Hauge, R. H. Muller, and C. G. Smith, "Conventions and formulas for using the Mueller-Stokes calculus in ellipsometry," *Surf. Sci.* **96**(1-3), 81107 (1980).
- [59] S.-Y. Lu and R. A. Chipman, "Interpretation of Mueller matrices based on polar decomposition," *J. Opt. Soc. Am. A* **13**, 1106 – 1113 (1996).
- [60] R. Azzam, "Propagation of partially polarized light through anisotropic media with or without depolarization: a differential 4 x 4 matrix calculus," *J. Opt. Soc. Am.* **68**(12), 1756–1767 (1978).
- [61] S. Manhas, M. K. Swami, P. Buddhiwant, N. Ghosh, P. K. Gupta, and J. Singh, "Mueller matrix approach for determination of optical rotation in chiral turbid media in backscattering geometry," *Opt. Express* **14**(1), 190 – 202 (2006).
- [62] J. Morio and F. Goudail, "Influence of the order of diattenuator, retarder, and polarizer in polar decomposition of Mueller matrices," *Opt. Lett.* **29**, 2234–6 (2004).
- [63] R. Ossikovski, A. De Martino, and S. Guyot, "Forward and reverse product decompositions of depolarizing Mueller matrices," *Opt. Lett.* **32**(6), 689691 (2007).
- [64] S. Kumar, H. Purwar, R. Ossikovski, I. A. Vitkin, and N. Ghosh, "Comparative study of differential matrix and extended polar decomposition formalisms for polarimetric characterization of complex tissue-like turbid media," *J. Biomed. Opt.* **17**, 105006 (2012).
- [65] R. Ossikovski, "Differential matrix formalism for depolarizing anisotropic media," *Opt. Lett.* **36**, 2330–2 (2011).
- [66] J. J. Gil and E. Bernabeu, "Depolarization and polarization indices of an optical system," *Opt. Acta (Lond)*. **33**(2), 185–189 (1986).

- [67] H. G. Tompkins and E. A. Irene, *Handbook of Ellipsometry*, no. 1, William Andrew Publishing/Noyes, Norwich, NY 13815 (2005).
- [68] O. Arteaga, A. Canillas, R. Purrello, and J. M. Ribó, “Evidence of induced chirality in stirred solutions of supramolecular nanofibers,” *Opt. Lett.* **34**, 2177 (2009).
- [69] V. V. Tuchin, L. V. Wang, and D. A. Zimnyakov, *Optical Polarization in Biomedical Applications*, Springer, Berlin (2006).
- [70] R. J. McNichols and G. L. Coté, “Optical glucose sensing in biological fluids: an overview.,” *J. Biomed. Opt.* **5**, 5–16 (2000).
- [71] J. C. McLennan and G. M. Shrum, “On the Origin of the Auroral Green Line 5577 Angstrom, and Other Spectra Associated with the Aurora Borealis,” *Proc. R. Soc. London. Ser. A* **108**, 501–512 (1925).
- [72] N. Bone, *Aurora*, Patrick Moore’s Practical Astronomy Series, Springer New York, New York, NY (2007).
- [73] P. Brekke and F. Broms, *Nordlyset - En guide*, Forlaget Press (2013).
- [74] N. Zheludev, “The life and times of the LED — a 100-year history,” *Nat. Photonics* **1**, 189–192 (2007).
- [75] E. A. Chandross, “A new chemiluminescent system,” *Tetrahedron Lett.* **4**, 761–765 (1963).
- [76] M. M. Rauhut, “Chemiluminescence from concerted peroxide decomposition reactions,” *Acc. Chem. Res.* **2**, 80–87 (1969).
- [77] A. Roda, Ed., *Chemiluminescence and Bioluminescence*, Royal Society of Chemistry, Cambridge (2010).
- [78] C. L. Tang and T. F. Deutsch, “Generation of Anti-Stokes Radiation in the Higher Order Coherent Raman Processes,” *Phys. Rev.* **138**, A1–A8 (1965).
- [79] R. F. Begley, “Coherent anti-Stokes Raman spectroscopy,” *Appl. Phys. Lett.* **25**(7), 387 (1974).
- [80] F. Träger, Ed., *Springer Handbook of Lasers and Optics*, Springer Berlin Heidelberg, Berlin, Heidelberg (2012).
- [81] S. J. F. W. Herschel, “Ἀμόρφωτα No. I. On a Case of Superficial Colour Presented by a Homogeneous Liquid Internally Colourless,” *Philos. Trans. R. Soc. London* **135**, 143–145 (1845).

## Bibliography

- [82] K. M. Psonka-Antonczyk, J. Duboisset, B. T. Stokke, T. Zako, T. Kobayashi, M. Maeda, S. Nyström, J. Mason, P. Hammarström, K. P. R. Nilsson, and M. Lindgren, “Nanoscopic and photonic ultrastructural characterization of two distinct insulin amyloid States,” *Int. J. Mol. Sci.* **13**, 1461–80 (2012).
- [83] T. Dieing, O. Hollricher, and J. Toporski, *Confocal Raman Microscopy*, vol. 158 of *Springer Series in Optical Sciences*, Springer Berlin Heidelberg, Berlin, Heidelberg (2011).
- [84] K. Kneipp, M. Moskovits, and H. Kneipp, Eds., *Surface-Enhanced Raman Scattering*, vol. 103 of *Topics in Applied Physics*, Springer Berlin Heidelberg (2006).
- [85] L. Aas, M. Kildemo, Y. Cohin, and E. Søndergård, “Determination of small tilt angles of short GaSb nanopillars using UV–visible Mueller matrix ellipsometry,” *Thin Solid Films* **541**, 97–101 (2013).
- [86] A. M. Gandorfer, “Ferroelectric retarders as an alternative to piezoelectric modulators for use in solar Stokes vector polarimetry,” *Opt. Eng.* **38**, 1402 (1999).
- [87] P. Collins, R. M. Redfern, B. Sheehan, D. Phelan, O. Ryan, and A. Shearer, “Design, Construction and Calibration Of The Galway Astronomical Stokes Polarimeter (GASP),” in *AIP Conf. Proc.*, **984**, 241–246, AIP (2008).
- [88] A. Alvarez-Herrero, V. Martínez-Pillet, J. del Toro Iniesta, and V. Domingo, “The IMaX polarimeter for the solar telescope SUNRISE of the NASA long duration balloon program,” *EPJ Web Conf.* **5**, 05002 (2010).
- [89] L. M. S. Aas, *Mueller Matrix Imaging and Spectroscopy*. PhD thesis, Norwegian University of Science and Technology (2013).
- [90] E. Compain, S. Poirier, and B. Drevillon, “General and self-consistent method for the calibration of polarization modulators, polarimeters, and mueller-matrix ellipsometers,” *Appl. Opt.* **38**, 3490–502 (1999).
- [91] E. Garcia-Caurel, “Spectroscopic Mueller polarimeter based on liquid crystal devices,” *Thin Solid Films* **455-456**, 120–123 (2004).
- [92] C. S. Perone, “Pyevolve.” <http://pyevolve.sourceforge.net/>.
- [93] J. S. Tyo, “Noise equalization in Stokes parameter images obtained by use of variable-retardance polarimeters,” *Opt. Lett.* **25**, 1198 (2000).

- [94] F. Stabo-Eeg, “Well-conditioned multiple laser Mueller matrix ellipsometer,” *Opt. Eng.* **47**, 073604 (2008).
- [95] A. Ben-Israel and T. N. Greville, *Generalized Inverses: Theory and Applications*, CMS Books in Mathematics, Springer, New York, 2nd. ed. (2003).
- [96] A. Shtukenberg and Y. O. Punin, *Optically Anomalous Crystals*, Springer Netherlands, Dordrecht (2007).
- [97] P. Hariharan, *Optical Interferometry*, Electronics & Electrical, Academic Press (2003).
- [98] P. Mouroulis, R. O. Green, and T. G. Chrien, “Design of Pushbroom Imaging Spectrometers for Optimum Recovery of Spectroscopic and Spatial Information,” *Appl. Opt.* **39**, 2210 (2000).
- [99] P. Mouroulis and M. M. McKerns, “Pushbroom imaging spectrometer with high spectroscopic data fidelity: experimental demonstration,” *Opt. Eng.* **39**, 808 (2000).
- [100] R. Lansford, G. Bearman, and S. E. Fraser, “Resolution of multiple green fluorescent protein color variants and dyes using two-photon microscopy and imaging spectroscopy,” *J. Biomed. Opt.* **6**, 311–8 (2001).
- [101] M. E. Dickinson, G. Bearman, S. Tille, R. Lansford, and S. E. Fraser, “Multi-spectral imaging and linear unmixing add a whole new dimension to laser scanning fluorescence microscopy,” *Biotechniques* **31**, 1272, 1274–6, 1278 (2001).
- [102] T. Zimmermann, “Spectral imaging and its applications in live cell microscopy,” *FEBS Lett.* **546**, 87–92 (2003).
- [103] T. Zimmermann, “Spectral imaging and linear unmixing in light microscopy,” *Microsc. Tech.* **95**, 245–265 (2005).
- [104] I. T. Jolliffe, *Principal Component Analysis*, Springer Series in Statistics, Springer-Verlag, New York, 2nd ed. (2002).
- [105] P. Tait, *Introduction to Radar Target Recognition*, IEE radar, sonar, navigation, and avionics series, The Institution of Engineering and Technology (2005).
- [106] J. A. Richards, *Remote Sensing with Imaging Radar*, Signals and Communication Technology, Springer Berlin Heidelberg, Berlin, Heidelberg (2009).

## Bibliography

- [107] R. E. Walpole, R. H. Myers, S. L. Myers, and K. Ye, *Probability and Statistics for Engineers and Scientists*, Pearson Education, 7th intern ed. (2002).
- [108] G. Schulze, A. Jirasek, M. M. L. Yu, A. Lim, R. F. B. Turner, and M. W. Blades, "Investigation of selected baseline removal techniques as candidates for automated implementation," *Appl. Spectrosc.* **59**, 545–74 (2005).
- [109] H. G. Schulze, R. B. Foist, K. Okuda, A. Ivanov, and R. F. B. Turner, "A small-window moving average-based fully automated baseline estimation method for Raman spectra," *Appl. Spectrosc.* **66**, 757–64 (2012).
- [110] J. B. Pawley, *Handbook Of Biological Confocal Microscopy*, Springer US, Boston, MA, 3rd ed. (2006).
- [111] ASTM, "Standard Guide for Raman Shift Standards for Spectrometer Calibration," *Annu. B. ASTM Stand.* **E1840-96**, 1–11 (2007).
- [112] R. Westlund, E. Glimsdal, M. Lindgren, R. Vestberg, C. Hawker, C. Lopes, and E. Malmström, "Click chemistry for photonic applications: triazole-functionalized platinum(ii) acetylides for optical power limiting," *J. Mater. Chem.* **18**(2), 166 (2008).
- [113] M. O. Trulson and R. A. Mathies, "Raman cross section measurements in the visible and ultraviolet using an integrating cavity: Application to benzene, cyclohexane, and cacodylate," *J. Chem. Phys.* **84**, 2068 (1986).
- [114] B. Li and A. B. Myers, "Absolute Raman cross sections for cyclohexane, acetonitrile, and water in the far-ultraviolet region," *J. Phys. Chem.* **94**, 4051–4054 (1990).
- [115] E. Glimsdal, I. Dragland, M. Carlsson, B. Eliasson, T. B. Melø, and M. Lindgren, "Triplet excited states of some thiophene and triazole substituted platinum(II) acetylide chromophores," *J. Phys. Chem. A* **113**, 3311–20 (2009).
- [116] E. Glimsdal, *Spectroscopic characterization of some platinum acetylide molecules for optical power limiting applications*. PhD thesis, NTNU (2009).



# A. Excited state absorption

*"I have always believed, and I still believe,  
that whatever good or bad fortune may come  
our way we can always give it meaning and  
transform it into something of value."*

— Hermann Hesse, *Siddhartha*

This appendix describes an excited state absorption setup designed and built during the work in the thesis. Due to unforeseen circumstances, the setup, which was built in another lab, was not published and no spectra exists from it. Since a similar system is present in our lab, and it was used during the thesis, this chapter is added to the appendix for future reference.

## A.1. Background and theory

Understanding the excited states of a molecule gives insight into how it behaves under high intensity excitation, were a large portion of them are in the excited state. This is for instance the case in optical power limiting materials used to protect eyes and sensors [112, 115, 116].

When studying the excited states of a molecule or an atom and how energy is transferred to or from it, excited state absorption spectroscopy is a useful tool. It measures the absorbance of the excited state, which is normally done in a four step procedure consisting of recording the background spectrum  $I_0$ , pump emission (only firing the pump)  $I_{em}$ , ground state absorption (only firing the probe)  $I_p$  and lastly the transient absorption (firing both pump and probe)  $I_t$ . The transient absorption can then be calculated by [115, 116]

$$\Delta A(\tau, \lambda) = \log \frac{I_p - I_0}{I_t - I_{em}}. \quad (\text{A.1})$$

Here  $\tau$  is the delay between firing the pump and the probe and  $\lambda$  the wavelength. In order to calculate the excited state absorption, knowledge of the ground state absorption

$$A_g(\lambda) = \epsilon_g CL = \log \frac{I_r - I_0}{I_p - I_0}, \quad (\text{A.2})$$

### A. Excited state absorption

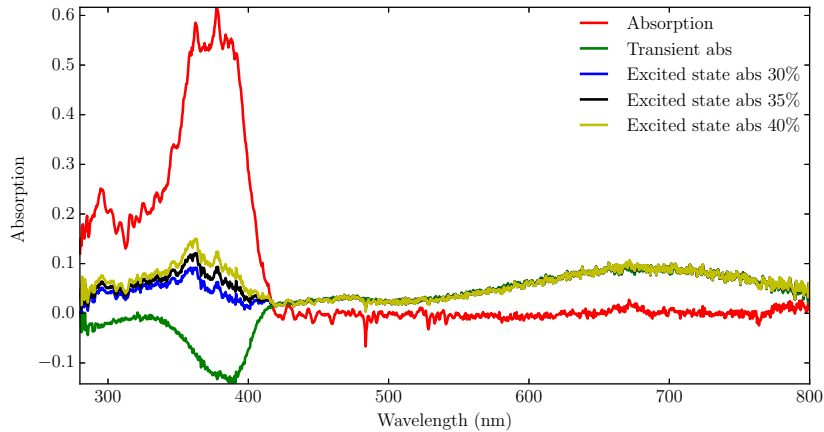


Figure A.1.: The “by eye” comparison of the addition of different amounts of ground state absorption to the excited state. Here the 35 % was chosen as the correct excited state absorption since it does not dip down in the transition at  $\approx 400$  nm. The plotted data are from Kindahl et al. [14].

is needed. In the equation  $C$  is the concentration,  $L$  the path length through the sample,  $\epsilon_g$  the ground state extinction coefficient, and  $I_r$  a reference spectrum taken of the reference sample (for example the solvent). The equation assumes that the background ( $I_0$ ) is the same for both the reference and the sample.  $\Delta A(\tau)$  will contain absorption from the ground state due to molecules not being excited by the pump or have decayed during the delay ( $\tau$ ).  $\Delta A(\tau)$  is given by Glimsdal et al. [115,116] as

$$\Delta A(\tau, \lambda) = A(\tau, \lambda) - A_g(\lambda) = [\epsilon_t - \epsilon_g] C_t L, \quad (\text{A.3})$$

with  $\epsilon_t$  being the excited state (triplet-triplet) extinction coefficient. As one is normally interested in the excited state absorption  $A(\tau, \lambda)$  in order to calculate  $\epsilon_t$ , it is necessary to remove the influence of the ground state absorption. This is done by adding a certain amount of the ground state absorption until the ground state depletion disappears from the spectrum. As it has to be done “by eye”, it induces some additional uncertainty. An example of such an uncertainty can be observed in figure A.1.

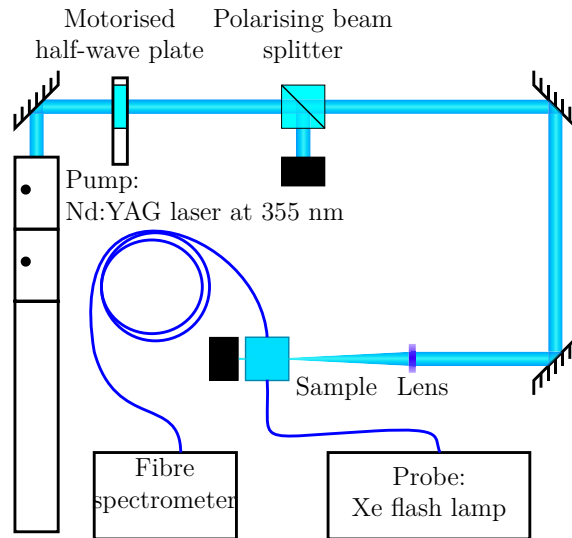


Figure A.2.: The excited state absorption setup. The pump is a Nd:YAG tripled laser. Probing is done with a microsecond pulsed xenon lamp coupled to an optical fibre. An Ocean optics spectrometer is used to detect the absorbance. The black boxes are beam dumps.

## A.2. Methods and result

The measurement of the excited state absorption, requires a pump-probe setup. During the work presented here, two different setups were used. One was a previous developed setup, briefly explained in Kindahl et al. [14] and in detail by Glimsdal et al. [115]. For the pump excitation, the setup uses a high intensity xenon lamp. A low power xenon lamp is used for the probe and a fibre spectrometer for the detection. The other setup is similar and is presented in figure A.2. It was custom built during this work, and uses a pulsed laser for the pump and a data acquisition card for the timing instead of the pulse delay generator used in the first setup.

As seen in figure A.2 the setup uses a motorised half-wave plate in combination with a polarising beam splitter to adjust the pump power from the 355 nm pulsed laser. Continuing along the beam, the focal volume of the beam in the sample is adjusted in such a way that the probe volume is inside of the pump volume. This ensures that the detected molecules have been excited by the pump. The system produced good results during development, however due to circumstances out of my control, it has not been possible to retrieve test spectra taken with it.

### *A. Excited state absorption*

The instrument explained by Glimsdal et al. [115], was used to study the excited state absorption (ESA) of platinum(II) complexes for nonlinear optical absorption. In understanding the absorption of energy in the excited state under high intensity illumination ESA is a useful tool as it is possible to calculate the  $\epsilon_t$  and  $A(\tau, \lambda)$  using equation A.3. For the platinum complexes studied by Kindahl et al. [14], this meant that it was possible to see that the absorption of energy in the UV, lead to a possibility of an excited state absorption in the range 550 nm to 800 nm.

## **B. Papers**



P. A. Letnes, I. S. Nerbø, L. M. S. Aas, P. G. Ellingsen,  
and M. Kildemo, “Fast and optimal broad-band Stokes/Mueller  
polarimeter design by the use of a genetic algorithm,”  
*Opt. Express* **18**, 10 (2010)

**Paper 1**





# Fast and optimal broad-band Stokes/Mueller polarimeter design by the use of a genetic algorithm

Paul Anton Letnes,\* Ingar Stian Nerbø, Lars Martin Sandvik Aas, Pål Gunnar Ellingsen, and Morten Kildemo

Department of Physics, The Norwegian University of Science and Technology (NTNU), N-7491 Trondheim, Norway

\*[paul.anton.letnes@gmail.com](mailto:paul.anton.letnes@gmail.com)

**Abstract:** A fast multichannel Stokes/Mueller polarimeter with no mechanically moving parts has been designed to have close to optimal performance from 430 – 2000 nm by applying a genetic algorithm. Stokes (Mueller) polarimeters are characterized by their ability to analyze the full Stokes (Mueller) vector (matrix) of the incident light (sample). This ability is characterized by the condition number,  $\kappa$ , which directly influences the measurement noise in polarimetric measurements. Due to the spectral dependence of the retardance in birefringent materials, it is not trivial to design a polarimeter using dispersive components. We present here both a method to do this optimization using a genetic algorithm, as well as simulation results. Our results include fast, broad-band polarimeter designs for spectrographic use, based on 2 and 3 Ferroelectric Liquid Crystals, whose material properties are taken from measured values. The results promise to reduce the measurement noise significantly over previous designs, up to a factor of 4.5 for a Mueller polarimeter, in addition to extending the spectral range.

© 2010 Optical Society of America

**OCIS codes:** (120.2130) Ellipsometry and polarimetry; (120.4570) Optical design of instruments; (300.0300) Spectroscopy.

---

## References and links

1. A. M. Gandorfer, "Ferroelectric retarders as an alternative to piezoelectric modulators for use in solar Stokes vector polarimetry," *Opt. Eng.* **38**, 1402–1408 (1999).
2. P. Collins, R. Redfern, and B. Sheehan, "Design, construction and calibration of the Galway astronomical Stokes polarimeter (GASP)," in *AIP Conference Proceedings*, D. Phelan, O. Ryan, and A. Shearer, eds. (AIP, Edinburgh (Scotland), 2008), vol. 984, p. 241.
3. A. Alvarez-Herrero, V. Martínez-Pillet, J. del Toro Iniesta, and V. Domingo, "The IMAx polarimeter for the solar telescope SUNRISE of the NASA long duration balloon program," in *Proceedings of AIP '09*, E. Garcia-Caurel, ed. (EPJ Web of Conferences, 2010), vol. 5, p. 05002.
4. J. D. Howe, M. A. Miller, R. V. Blumer, T. E. Petty, M. A. Stevens, D. M. Teale, and M. H. Smith, "Polarization sensing for target acquisition and mine detection," in *Polarization Analysis, Measurement, and Remote Sensing III*, D. B. Chenault, M. J. Duggin, W. G. Egan, and D. H. Goldstein, eds., *Proc. SPIE* **4133**, 202–213 (2000).
5. M. H. Smith, P. D. Burke, A. Lompadó, E. A. Tanner, and L. W. Hillman, "Mueller matrix imaging polarimetry in dermatology," in *Biomedical Diagnostic, Guidance, and Surgical-Assist Systems II*, T. Vo-Dinh, W. S. Grundfest, and D. A. Benaron, eds., *Proc. SPIE* **3911**, 210–216 (2000).
6. R. N. Weinreb, S. Shakiba, and L. Zangwill, "Scanning laser polarimetry to measure the nerve fiber layer of normal and glaucomatous eyes," *Am. J. Ophthalmol.* **119**, 627–636 (1995).

7. M. Foldyna, A. D. Martino, R. Ossikovski, E. Garcia-Caurel, and C. Licitra, "Characterization of grating structures by Mueller polarimetry in presence of strong depolarization due to finite spot size," *Opt. Commun.* **282**, 735–741 (2009).
8. I. S. Nerbø, S. Le Roy, M. Foldyna, M. Kildemo, and E. Søndergård, "Characterization of inclined GaSb nanopillars by Mueller matrix ellipsometry," *J. Appl. Phys.* **108**, 014307 (2010).
9. L. Jin, M. Kasahara, B. Gelloz, and K. Takizawa, "Polarization properties of scattered light from macrorough surfaces," *Opt. Lett.* **35**, 595–597 (2010).
10. T. A. Germer, "Polarized light scattering by microroughness and small defects in dielectric layers," *J. Opt. Soc. Am. A* **18**, 1279–1288 (2001).
11. T. Germer, "Measurement of roughness of two interfaces of a dielectric film by scattering ellipsometry," *Phys. Rev. Lett.* **85**, 349–352 (2000).
12. F. Stabo-Eeg, M. Kildemo, I. Nerbø, and M. Lindgren, "Well-conditioned multiple laser Mueller matrix ellipsometer," *Opt. Eng.* **47**, 073604 (2008).
13. J. S. Tyo, "Noise equalization in Stokes parameter images obtained by use of variable-retardance polarimeters," *Opt. Lett.* **25**, 1198–1200 (2000).
14. D. S. Sabatke, M. R. Descour, E. L. Dereniak, W. C. Sweatt, S. A. Kemme, and G. S. Phipps, "Optimization of retardance for a complete Stokes polarimeter," *Opt. Lett.* **25**, 802–804 (2000).
15. R. M. A. Azzam and A. De, "Optimal beam splitters for the division-of-amplitude photopolarimeter," *J. Opt. Soc. Am. A* **20**, 955–958 (2003).
16. R. M. A. Azzam, "Photopolarimetric measurement of the Mueller matrix by Fourier analysis of a single detected signal," *Opt. Lett.* **2**, 148 (1978).
17. J. M. Bueno, "Polarimetry using liquid-crystal variable retarders: theory and calibration," *J. Opt. A: Pure Appl. Opt.* **2**, 216–222 (2000).
18. E. Garcia-Caurel, A. D. Martino, and B. Drévilion, "Spectroscopic Mueller polarimeter based on liquid crystal devices," *Thin Solid Films* **455–456**, 120–123 (2004).
19. J. Ladstein, M. Kildemo, G. Svendsen, I. Nerbø, and F. Stabo-Eeg, "Characterisation of liquid crystals for broadband optimal design of Mueller matrix ellipsometers," in *Liquid Crystals and Applications in Optics*, M. Glogarova, P. Palfy-Muhoray, and M. Copic, eds. Proc. SPIE **6587**, 65870D (2007).
20. L. M. S. Aas, P. G. Ellingsen, M. Kildemo, and M. Lindgren, "Dynamic Response of a fast near infra-red Mueller matrix ellipsometer," *J. Mod. Opt.* (**accepted**) (2010).
21. D. Cattelan, E. Garcia-Caurel, A. De Martino, and B. Dreivilion, "Device and method for taking spectroscopic polarimetric measurements in the visible and near-infrared ranges," Patent application 2937732, France (2010).
22. J. H. Holland, "Genetic algorithms," *Scientific American* **267**, 44–50 (1992).
23. D. Floreano and C. Mattiussi, *Bio-Inspired Artificial Intelligence: Theories, Methods, and Technologies* (The MIT Press, 2008).
24. A. Kudla, "Application of the genetic algorithms in spectroscopic ellipsometry," *Thin Solid Films* **455–456**, 804–808 (2004).
25. G. Cormier and R. Boudreau, "Genetic algorithm for ellipsometric data inversion of absorbing layers," *J. Opt. Soc. Am. A* **17**, 129–134 (2000).
26. V. R. Fernandes, C. M. S. Vicente, N. Wada, P. S. André, and R. A. S. Ferreira, "Multi-objective genetic algorithm applied to spectroscopic ellipsometry of organic-inorganic hybrid planar waveguides," *Opt. Express* **18**, 16580–16586 (2010).
27. F. Stabo-Eeg, M. Kildemo, E. Garcia-Caurel, and M. Lindgren, "Design and characterization of achromatic 132° retarders in CaF<sub>2</sub> and fused silica," *J. Mod. Opt.* **55**, 2203–2214 (2008).
28. W. H. Press, S. A. Teukolsky, W. T. Vetterling, and B. P. Flannery, *Numerical Recipes: The Art of Scientific Computing* (Cambridge University Press, 2007).
29. E. Compain, S. Poirier, and B. Dreivilion, "General and self-consistent method for the calibration of polarization modulators, polarimeters, and Mueller-matrix ellipsometers," *Appl. Opt.* **38**, 3490–3502 (1999).
30. J. Ladstein, F. Stabo-Eeg, E. Garcia-Caurel, and M. Kildemo, "Fast near-infra-red spectroscopic Mueller matrix ellipsometer based on ferroelectric liquid crystal retarders," *Phys. Status Solidi C* **5**, 1097–1100 (2008).

## 1. Introduction

Polarimeters are applied in a wide range of fields, from astronomy [1–3], remote sensing [4] and medical diagnostics [5, 6] to applications in ellipsometry such as characterizing gratings [7], nanostructures [8] and rough surfaces [9–11]. As all polarimeters are based on inverting so-called system matrices, it is well known that the measurement error from independent Gaussian noise is minimized when the condition number ( $\kappa$ ) of these system matrices is minimized [12, 13]. It has been shown that  $\kappa = \sqrt{3}$  is the best condition number that can be achieved for such a system, and that this optimal condition number can be achieved by several different

approaches using various optical components (*e.g.* rotating retarders [14], division of amplitude [15, 16], and liquid-crystal variable retarders [17]). In many applications it is necessary to perform fast spectroscopic measurements (*e.g.* by using a Charge-Coupled Device (CCD) based spectrograph) [18]. In that case, the wavelength dependence of the optical elements will cause the polarimeter not to be optimally conditioned over the full range simultaneously. A system based on two Ferroelectric Liquid Crystals (FLC) has been reported to be fast and reasonably well conditioned over the visible or near infrared spectral range [18–20]. By introducing a third FLC a similar system has been proposed to have an acceptable condition number from the visible to the near infra-red (430 – 1700 nm) [21]. The design of a system having the best possible condition number over a broad spectrum is a challenging optimization problem due to the large number of parameters; many optimization algorithms are prone to return local optimums, and a direct search is too time consuming. To avoid this time-consuming exhaustive search, we decided to employ the Genetic Algorithm (GA). A GA simulates evolution on a population of individuals in order to find an optimal solution to the problem at hand. Genetic Algorithms were pioneered by Holland [22], and are discussed in detail in *e.g.* Ref. [23]. GAs have previously been applied in ellipsometry to solve the inversion problem for the thickness and dielectric function of multiple thin layers, see *e.g.* Ref. [24–26].

## 2. Overdetermined polarimetry

A Stokes polarimeter consists of a polarization state analyzer (PSA) capable of measuring the Stokes vector of a polarization state, see Fig. 1. The PSA is based on performing at least 4 different measurements along different projection states. A measured Stokes vector  $\mathbf{S}$  can then be expressed as  $\mathbf{S} = \mathbf{A}^{-1}\mathbf{b}$ , where  $\mathbf{A}$  is a system matrix describing the PSA and  $\mathbf{b}$  is a vector containing the intensity measurements.  $\mathbf{A}^{-1}$  denotes the matrix inverse of  $\mathbf{A}$ , which in the case of overdetermined polarimetry with more than 4 projection states will denote the Moore–Penrose *pseudoinverse*. The analyzing matrix  $\mathbf{A}$  is constructed from the first rows of the Mueller matrices of the PSA for the different states. The noise in the measurements of  $\mathbf{b}$  will be amplified by the condition number of  $\mathbf{A}$ ,  $\kappa_{\mathbf{A}}$ , in the inversion to find  $\mathbf{S}$ . Therefore  $\kappa_{\mathbf{A}}$  should be as small as possible, which correspond to do as independent measurements as possible (*i.e.* to use projection states that are as orthogonal as possible).

A Mueller matrix  $\mathbf{M}$  describes how an interaction changes the polarization state of light, by transforming an incoming Stokes vector  $\mathbf{S}_{\text{in}}$  to the outgoing Stokes vector  $\mathbf{S}_{\text{out}} = \mathbf{M}\mathbf{S}_{\text{in}}$ . To measure the Mueller matrix of a sample it is necessary to generate at least 4 different polarization states by a polarization state generator (PSG) and measure the outgoing Stokes vector by at least 4 measurements for each generated state. The measured intensities can then be arranged in a matrix  $\mathbf{B} = \mathbf{A}\mathbf{W}$ , where the system matrix  $\mathbf{W}$  of the PSG contains the generated Stokes vectors as its columns. These generated Stokes vectors are found simply as the first column of the Mueller matrix of the PSG in the respective states.  $\mathbf{M}$  can then be found by inversion as  $\mathbf{M} = \mathbf{A}^{-1}\mathbf{B}\mathbf{W}^{-1}$ . The error  $\Delta\mathbf{M}$  in  $\mathbf{M}$  is then bounded by the condition numbers according to [27]

$$\frac{\|\Delta\mathbf{M}\|}{\|\mathbf{M}\|} \lesssim \kappa_{\mathbf{W}}\kappa_{\mathbf{A}} \frac{\|\Delta\mathbf{B}\|}{\|\mathbf{B}\|} + \kappa_{\mathbf{A}} \frac{\|\Delta\mathbf{A}\|}{\|\mathbf{A}\|} + \kappa_{\mathbf{W}} \frac{\|\Delta\mathbf{W}\|}{\|\mathbf{W}\|}. \quad (1)$$

The condition number is given as  $\kappa_{\mathbf{A}} = \|\mathbf{A}\|\|\mathbf{A}^{-1}\|$ , which for the 2-norm can be calculated from the ratio of the largest to the smallest singular value [28].  $\Delta\mathbf{A}$  and  $\Delta\mathbf{W}$  are calibration errors, which increase with  $\kappa$  when calibration methods using matrix inversion are applied. The PSG can be constructed from the same optical elements as the PSA, placed in the reverse order, which would give  $\kappa_{\mathbf{A}} = \kappa_{\mathbf{W}} \equiv \kappa$ . As the error in Mueller matrix measurements is proportional

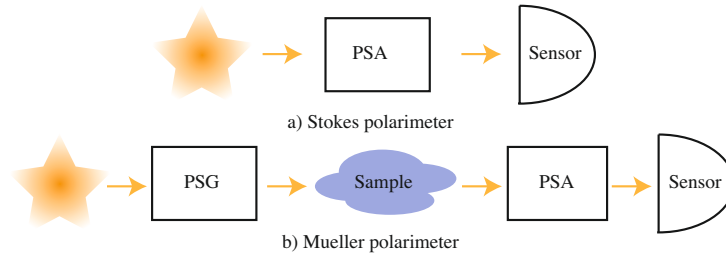


Fig. 1. (a) A Stokes polarimeter measures the polarization state of an arbitrary light source using a Polarization State Analyzer (PSA). (b) A Mueller polarimeter measures how the polarization state of light, generated by with a Polarization State Generator (PSG), is changed by a sample.

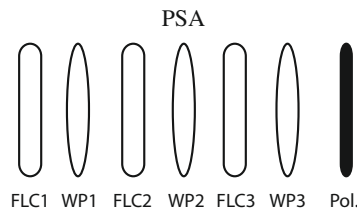


Fig. 2. Sketch of a PSA consisting of 3 FLC's, 3 waveplates (WP), each with a retardance  $\delta$  and an orientation  $\theta$  relative to the transmission axis of a polarizer.

to  $\kappa^2$ , it is very important to keep this value as low as possible.

If 4 optimal states can be achieved (giving  $\kappa = \sqrt{3}$ ), no advantage is found by doing a larger number of measurements with different states, compared to repeated measurements with the 4 optimal states [14]. If, however, these optimal states can not be produced ( $\kappa > \sqrt{3}$ ), the condition number, and hence the error, can be reduced by performing more than 4 measurements. For a FLC based polarimeter this can be done by using 3 FLCs followed by a polarizer as PSA, with up to 3 waveplates (WP) between the FLCs to increase the condition number (see Fig. 2). A PSG can be constructed with the same elements in the reverse order. Since each FLC can be switched between two states (this switching can be described as a rotation of the fast axis of a retarder by  $+45^\circ$ ),  $2^3 = 8$  different states can be analyzed (generated) by the PSA (PSG). To accurately measure the Stokes vector, the system matrix  $\mathbf{A}$  needs to be well known. For a Mueller polarimeter generating and analyzing 4 states in the PSG and PSA, the eigenvalue calibration method (ECM) [29] can be applied. The ECM allows the measuring of the actual produced states by the PSA and PSG ( $\mathbf{A}$  and  $\mathbf{W}$ ), without relying on exact knowledge or modeling of the optical components. However, the ECM is based on the inversion of a product of measured intensity matrices  $\mathbf{B}$  for measurements on a set of calibration samples. This product becomes singular for a system analyzing and generating more than four states. A workaround of this problem is to choose the subset of 4 out of 8 states which gives the lowest  $\kappa$  value, and build a  $\mathbf{B}$  matrix of those states to find 4 of the 8 rows (columns) of  $\mathbf{A}$  ( $\mathbf{W}$ ). More rows (columns) of  $\mathbf{A}$  ( $\mathbf{W}$ ) can then be found by calibrating on a different subset of the 8 states, giving the second lowest  $\kappa$  value, and so on. By repeating the calibration on different subsets of states, all the 8 rows (columns) of  $\mathbf{A}$  ( $\mathbf{W}$ ) can be found with low relative error  $\|\Delta\mathbf{A}\|/\|\mathbf{A}\|$  ( $\|\Delta\mathbf{W}\|/\|\mathbf{W}\|$ ).

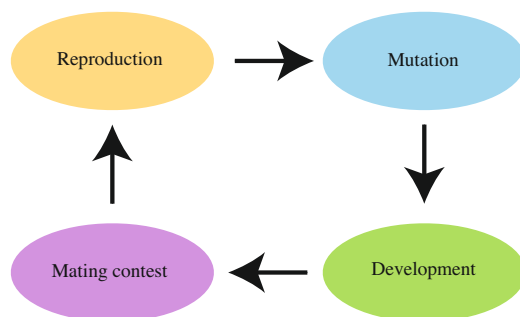


Fig. 3. The four essential processes in a genetic algorithm are shown above. Sexual reproduction is performed by multi-point genetic crossover, giving rise to the next generation of individuals. Mutation can be simulated with simple bit negation (e.g.  $0 \rightarrow 1$  and *vice versa*). Development is the process where a genotype is interpreted into its phenotype, *i.e.* the binary genome is interpreted as a polarimeter design. In the mating contest, one evaluates the fitness of each individual's phenotype, and let the more fit individuals reproduce with higher probability than the less fit individuals.

### 3. Genetic optimization

In order to optimize  $\kappa(\lambda)$ , one can conceivably employ a variety of optimization algorithms, from simple brute-force exhaustive search to more advanced algorithms, such as *e.g.* Levenberg–Marquardt, simulated annealing, and particle swarm optimization. Our group has previously performed optimization of a polarimeter design based on fixed components, namely, two FLCs and two waveplates. In this case, the optimization problem reduces to searching the space of 4 orientation angles. With a resolution of  $1^\circ$  per angle, this gives a search space consisting of  $180^4 \approx 10^9$  states to evaluate; on modern computer hardware, this direct search can be performed. In order to optimize the retardances of the components as well, the total number of states increases to about  $(10^9)^2 = 10^{18}$ . Obviously, brute force exhaustive search is unfeasible for such large search spaces.

A GA performs optimization by simulating evolution in a population of individuals (here: simulated polarimeters). The three pillars of evolution are variation, heritability, and selection. Our initial population must have some initial genetic variation between the individuals; hence, we initialize our population by generating random individuals. Heritability means that the children have to carry on some of the traits of their parents. We simulate this by either cloning parents into children (asexual reproduction) or by performing genetic crossover (sexual reproduction) in a manner that leave children with some combination of the traits of their parents. Finally, selection is done by giving more fit individuals a larger probability of survival. For this purpose, we used the tournament selection protocol, described in Ref. [23]. For a sketch of the essential processes involved in a GA, see Fig. 3.

Our GA builds directly on the description given by Holland [22], using a binary genome as the genetic representation. In this representation, a string of 0s and 1s represent the genome of the individual. To simulate mutation in our genetic algorithm, we employ logical bit negation; *i.e.*  $0 \rightarrow 1$  or *vice versa*. Sexual reproduction is simulated by using multi-point crossover, *i.e.* simply cutting and pasting two genomes together, as described by Holland [22].

The interpretation of the genome into a phenotype (development), in this case a polarimeter design, is done in a straightforward way. For each variable in the polarimeter's configuration,

*i.e.* for each orientation angle and each retardance, we select  $m$  bits in the genome (typically,  $m = 8$ ) and interpret this number as an integer in the range from 1 to  $2^m$ . The integer is subsequently interpreted as a real number in a predefined range, *e.g.*,  $\theta \in [0^\circ, 180^\circ]$ . In order to avoid excessively large jumps in the search space due to mutations, we chose to implement the interpretation of bits into integers by using the Gray code, also known as the reflected binary code. The most important parameter values in our GA are shown in Table 2. Making good choices for each of these parameters is often essential in order to ensure good convergence.

After determining the phenotype, we must assign to each simulated polarimeter individual a fitness function (also known as the objective function). In order to do this, we first calculate  $\kappa(\lambda)$ . As discussed,  $\kappa^{-1}(\lambda)$  maximally takes on the value  $1/\sqrt{3}$ . Hence, we define an error function,  $e$ , as

$$e = \frac{1}{N_\lambda} \sum_{n=1}^{N_\lambda} \left( \kappa^{-1}(\lambda_n) - 1/\sqrt{3} \right)^4. \quad (2)$$

In Eq. (2),  $\lambda_n = \lambda_{\min} + (n-1)\Delta\lambda$ , with  $n = 1, 2, \dots, N_\lambda$  and  $\Delta\lambda = 5$  nm.  $\lambda_{\min}$  and  $N_\lambda$  are determined by the wavelength range we are interested in. The choice of taking the difference between  $\kappa^{-1}(\lambda)$  and the optimal value to power 4 is done in order to “punish” peaks in the condition number more severely. As GAs conventionally seek to maximize the fitness function, we define an individual’s fitness as

$$f = \frac{1}{e}. \quad (3)$$

This definition is convenient because  $f$  takes on real and positive values where higher values represents more optimal polarimeter designs.

#### 4. Results

For the case of a polarimeter based on 3 FLCs and 3 WPs, we have minimized  $\kappa(\lambda)$  by varying the orientation angle,  $\theta$ , and the retardance,  $\delta$ , of all the elements. This yields a 12-dimensional search space, *i.e.*, 6 retardances and 6 orientation angles.  $\theta$  is the angle between the fast axis of the retarder (WP or FLC) and the transmission axis of the polarizer (see Fig. 2), taken to be in the range  $\theta \in [0^\circ, 180^\circ]$ . The retardance,  $\delta$ , is modeled using a modified Sellmeier equation,

$$\delta \approx 2\pi L \left[ \frac{A_{UV}}{(\lambda^2 - \lambda_{UV}^2)^{1/2}} - \frac{A_{IR}}{(\lambda_{IR}^2 - \lambda^2)^{1/2}} \right], \quad (4)$$

where  $A_{UV}$ ,  $A_{IR}$ ,  $\lambda_{UV}$ , and  $\lambda_{IR}$  are experimentally determined parameters for an FLC ( $\lambda/2@510$  nm, Displaytech Inc.) and a Quartz zero order waveplate ( $\lambda/4@465$  nm) taken directly from Refs. [19] (for the FLCs,  $A_{IR} = 0$ ).  $L$  is a normalized thickness, with  $L = 1$  corresponding to a retardance of  $\lambda/2@510$  nm for the FLCs and  $\lambda/4@465$  nm for the waveplates. Each  $L$  and  $\theta$  are represented by 8 bits each in the genome. We use experimental values to ensure that our design is based on as realistic components as possible.

The 3-FLC polarimeter design scoring the highest fitness function is shown in Table 1. The wavelength range for which we optimized the polarimeter was from 430 to 2000 nm. To visualize the performance of this design, we show a plot of  $\kappa^{-1}(\lambda)$  in Fig. 4. The inverse condition number,  $\kappa^{-1}$ , is larger than 0.5 over most parts of the spectrum, which is close to the optimal inverse condition number ( $\kappa^{-1} = 1/\sqrt{3} = 0.577$ ). This is a great improvement compared to the earlier reported 3-FLC design [21], which oscillates around  $\kappa^{-1} \approx 0.33$ . The new design promise a decrease in noise amplification by up to a factor of 2.1 for a Stokes polarimeter, and up to factor of 4.5 for a Mueller polarimeter. In addition the upper spectral limit is extended

Table 1. Orientation angles,  $\theta$ , and normalized thicknesses  $L$ , of the components of the best 3-FLC polarimeter. (WP = (fixed) waveplate)

Component	$\theta$ [°]	$L$
FLC1	56.5	2.44
WP1	172.9	1.10
FLC2	143.3	1.20
WP2	127.1	1.66
FLC3	169.4	1.42
WP3	110.1	4.40

from 1700 nm to 2000 nm. Shorter wavelengths than 430 nm were not considered as the FLC material will be degraded by exposure to UV light. Previous designs often suffer from  $\kappa^{-1}(\lambda)$  oscillating as a function of wavelength, whereas our solution is more uniform over the wavelength range we are interested in. This uniformity in  $\kappa(\lambda)$  will, according to Eq. (1), give a more uniform noise distribution over the spectrum.

To give some idea of how fast the GA converges, a plot of  $f$  [see Eq. (3)] as a function of the generation number is shown in Fig. 5. The mean population fitness ( $\mu$ ) and standard deviation ( $\sigma$ ) is also shown. As so often happens with genetic algorithms, we see that the maximal and average fitness increases dramatically in the first few generations. Following this fast initial progress, evolution slows down considerably, before it finally converges after 600 generations. The parameters used in our GA to obtain these results are shown in Table 2.

A design using fewer components, in particular 2 FLCs and 2 waveplates, does have advantages. These advantages include increased transmission of light, as well as reduced cost and complexity with respect to building and maintaining the instrument. In addition some applications have weight and volume restrictions [3]. For these reasons, we have performed genetic optimization of the 2-FLC design. In Fig. 6, we show the performance of two polarimeter designs for the wavelength ranges 430 – 1100 nm (compatible with an Si detector) and 800 – 1700 nm. Both of these polarimeter designs show condition numbers which are considerably better

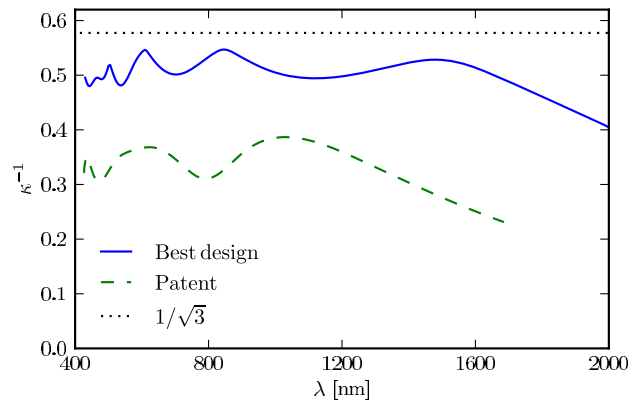


Fig. 4. Inverse condition number for the best GA-generated 3-FLC design. For comparison, we show the inverse condition number of the patented 3-FLC design [21].

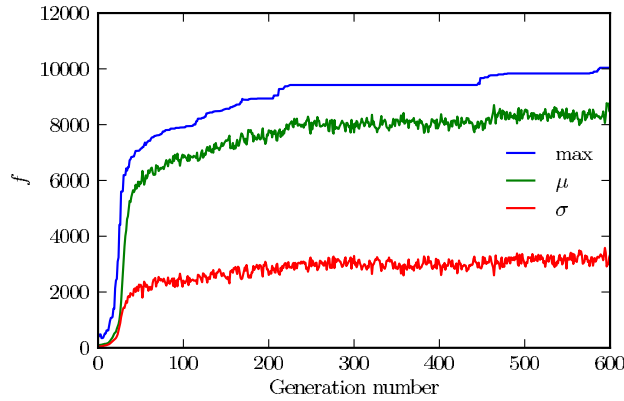


Fig. 5. Convergence of fitness as a function of generation number.  $\mu$  and  $\sigma$  refer to the average and standard deviation of the population's fitness, respectively. The best result from this simulation is the one shown in Fig. 4.

Table 2. Genetic Algorithm parameters. The “crossover rate” is the probability for two parents to undergo sexual reproduction (the alternative being asexual reproduction). The parameter “crossover points” refer to the number of points where we cut the genome during crossover (sexual reproduction). “Mutation rate” is the probability for any given individual to undergo one or several bit flip mutations in one generation

Parameter	Value
Crossover rate	0.7
Crossover points	2
Mutation rate	0.2
Population size	500

Table 3. Orientation angle,  $\theta$ , and normalized thickness,  $L$ , of the 2-FLC polarimeters shown in Fig. 6

Component	Visible design		NIR design	
	$\theta$ [°]	$L$	$\theta$ [°]	$L$
FLC 1	90.4	1.17	177.9	2.60
WP 1	3.5	3.58	112.9	2.94
FLC 2	92.5	1.02	74.8	1.75
WP 2	19.8	3.52	163.1	4.71

than previously reported designs. The numerical parameters of the two designs based on 2 FLCs are shown in Table 3.

Our optimization algorithm can, with little effort, be applied to a wider range of polarimeter design. Any optical component can be included into our GA; for example, one can include fixed waveplates of different materials, prisms, mirrors, and other types of liquid crystal devices. The material of each component could also be a variable, which could help alleviate the dispersion problem. The only requirement is that the retardance of the component in question must be



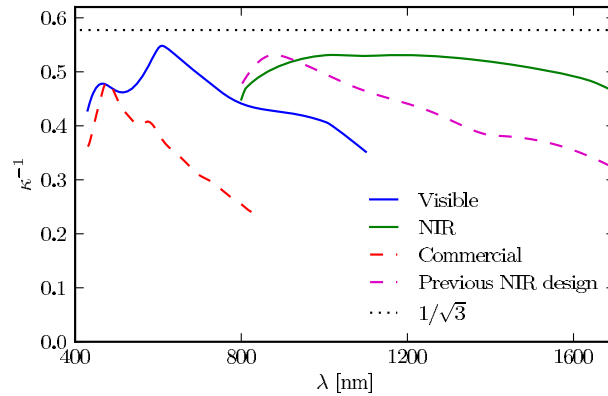


Fig. 6. Condition number for two designs using 2 FLC retarders and 2 waveplates. By optimizing  $\kappa(\lambda)$  over a narrower part of the spectrum, we can design good polarimeters with fewer components. The polarimeter designs labeled “Visible” and “IR” show our two designs, optimized for  $430 \text{ nm} < \lambda < 1100 \text{ nm}$  and  $800 \text{ nm} < \lambda < 1700 \text{ nm}$ , respectively. For comparison with our “NIR” design, we show the previous simulated design from Ref. [30]. The curve labeled “Commercial” shows the measured condition number of a commercial instrument (MM16, Horiba, 2006) based on the same (FLC) technology.

possible to either model theoretically or measure experimentally. It is possible to optimize a polarimeter for a different wavelength range, simply by changing program inputs. Focusing on a wavelength range which is as narrow as possible typically results in higher condition numbers than reported here. Evaluating different technologies, materials and components for polarimetry should thus be relatively straightforward. The task is not computationally formidable: we have used ordinary desktop computers in all our calculations.

## 5. Conclusion

In conclusion, we have used genetic algorithms to optimize the design of a fast multichannel spectroscopic Stokes/Mueller polarimeter, using fast switching ferroelectric liquid crystals. We have presented three polarimeter designs which promise significant improvement with respect to previous work in terms of noise reduction and spectral range. Our approach requires relatively little computational effort. One can easily generate new designs if one should wish to use other components and materials, or if one wishes to focus on a different part of the optical spectrum. We hope that our designs will make polarimetry in general, and ellipsometry in particular, a less noisy and more efficient measurement technique.

## Acknowledgements

The authors would like to thank professor Keith Downing at the Department of Computer and Information Science at NTNU for helpful discussions regarding genetic algorithms and their implementation.



L. M. S. Aas, P. G. Ellingsen, B. E. Fladmark, P. A. Letnes, and M. Kildemo, “Overdetermined broadband spectroscopic Mueller matrix polarimeter designed by genetic algorithms,” *Opt. Express* **21**, 8753 – 8762 (2013)

**Paper 2**



# Overdetermined broadband spectroscopic Mueller matrix polarimeter designed by genetic algorithms

Lars Martin Sandvik Aas,\* Pål Gunnar Ellingsen, Bent Even Fladmark, Paul Anton Letnes, and Morten Kildemo

Department of Physics, The Norwegian University of Science and Technology (NTNU),  
N-7491 Trondheim, Norway

\*[lars.martin.aas@gmail.com](mailto:lars.martin.aas@gmail.com)

**Abstract:** This paper reports on the design and implementation of a liquid crystal variable retarder based overdetermined spectroscopic Mueller matrix polarimeter, with parallel processing of all wavelengths. The system was designed using a modified version of a recently developed genetic algorithm [Letnes et al. *Opt. Express* **18**, 22, 23095 (2010)]. A generalization of the eigenvalue calibration method is reported that allows the calibration of such overdetermined polarimetric systems. Out of several possible designs, one of the designs was experimentally implemented and calibrated. It is reported that the instrument demonstrated good performance, with a measurement accuracy in the range of 0.1% for the measurement of air.

© 2013 Optical Society of America

**OCIS codes:** (120.2130) Ellipsometry and polarimetry; (120.4570) Optical design of instruments; (300.0300) Spectroscopy.

---

## References and links

1. P. G. Ellingsen, M. B. Lilledahl, L. M. S. Aas, C. d. L. Davies, and M. Kildemo, "Quantitative characterization of articular cartilage using Mueller matrix imaging and multiphoton microscopy," *J. Biomed. Opt.* **16**, 116002 (2011).
2. M. H. Smith, P. D. Burke, A. Lompadó, E. A. Tanner, and L. W. Hillman, "Mueller matrix imaging polarimetry in dermatology," *Proc. SPIE* **3911**, 210–216 (2000).
3. R. N. Weinreb, S. Shakiba, and L. Zangwill, "Scanning laser polarimetry to measure the nerve fiber layer of normal and glaucomatous eyes," *Am. J. Ophthalmol.* **119**, 627–636 (1995).
4. J. D. Howe, M. A. Miller, R. V. Blumer, T. E. Petty, M. A. Stevens, D. M. Teale, and M. H. Smith, "Polarization sensing for target acquisition and mine detection," *Proc. SPIE* **4133**, 202–213 (2000).
5. A. Alvarez-Herrero, V. Martínez-Pillet, J. del Toro Iniesta, and V. Domingo, "The IMaX polarimeter for the solar telescope SUNRISE of the NASA long duration balloon program," in *AP1'09*, (2010), pp. 05002.
6. R. Azzam and N. Bashara, *Ellipsometry and Polarized light* (North-Holland, 1977).
7. H. Fujiwara, *Spectroscopic Ellipsometry: Principles and Applications* (John Wiley & Sons, Chichester, England; Hoboken, NJ, 2007).
8. H. Tompkins and E. A. Irene, *Handbook of Ellipsometry* (William Andrew, 2005).
9. M. Foldyna, A. D. Martino, R. Ossikovski, E. Garcia-Caurel, and C. Licitra, "Characterization of grating structures by Mueller polarimetry in presence of strong depolarization due to finite spot size," *Opt. Commun.* **282**, 735–741 (2009).
10. D. Schmidt, A. C. Kjerstad, T. Hofmann, R. Skomski, E. Schubert, and M. Schubert, "Optical, structural, and magnetic properties of cobalt nanostructure thin films," *J. Appl. Phys.* **105**, 113508 (2009).
11. L. M. S. Aas, M. Kildemo, Y. Cohan, and E. Søndergård, "Determination of small tilt angles of short gasb nanopillars using uv-visible mueller matrix ellipsometry," *Thin Solid Films* (2012).

12. I. S. Nerbø, S. Le Roy, M. Foldyna, M. Kildemo, and E. Søndergård, "Characterization of inclined GaSb nanopillars by Mueller matrix ellipsometry," *J. Appl. Phys.* **108**, 014307 (2010).
13. T. Oates, H. Wormeester, and H. Arwin, "Characterization of plasmonic effects in thin films and metamaterials using spectroscopic ellipsometry," *Prog. Surf. Sci.* **86**, 328–376 (2011).
14. B. Gallas, K. Robbie, R. Abdeddaïm, G. Guida, J. Yang, J. Rivory, and a. Priou, "Silver square nanospirals mimic optical properties of U-shaped metamaterials," *Opt. Express* **18**, 16335–16344 (2010).
15. T. A. Germer, "Polarized light scattering by microroughness and small defects in dielectric layers," *J. Opt. Soc. Am. A* **18**, 1279–1288 (2001).
16. T. Germer, "Measurement of roughness of two interfaces of a dielectric film by scattering ellipsometry," *Phys. Rev. Lett.* **85**, 349–352 (2000).
17. Ø. Svensen, M. Kildemo, J. Maria, J. J. Stammes, and O. Frette, "Mueller matrix measurements and modeling pertaining to Spectralon white reflectance standards," *Opt. Express* **20**, 15045–15053 (2012).
18. J. M. Bennet, R. Chipman, and R. M. A. Azzam, "Polarized light," in *Handbook of Optics*, M. Bass and V. Mahajan, eds. (McGraw-Hill, Inc., 2010), pp. 12.3–16.21.
19. F. Stabo-Eeg, M. Kildemo, I. Nerbø, and M. Lindgren, "Well-conditioned multiple laser Mueller matrix ellipsometer," *Opt. Eng.* **47**, 073604 (2008).
20. E. Compain and B. Drevillon, "Complete high-frequency measurement of Mueller matrices based on a new coupled-phase modulator," *Rev. Sci. Instrum.* **68**, 2671 (1997).
21. O. Arteaga, J. Freudenthal, B. Wang, and B. Kahr, "Mueller matrix polarimetry with four photoelastic modulators: theory and calibration," *Appl. Optics* **51**, 6805–6817 (2012).
22. G. E. Jellison and F. a. Modine, "Two-channel polarization modulation ellipsometer," *Appl. Optics* **29**, 959–974 (1990).
23. E. Garcia-Caurel, A. D. Martino, and B. Drevillon, "Spectroscopic Mueller polarimeter based on liquid crystal devices," *Thin Solid Films* **455**, 120–123 (2004).
24. L. Aas, P. Ellingsen, and M. Kildemo, "Near infra-red Mueller matrix imaging system and application to retardance imaging of strain," *Thin Solid Films* **519**, 2737–2741 (2010).
25. P. Letnes, I. Nerbø, L. Aas, P. Ellingsen, and M. Kildemo, "Fast and optimal broad-band Stokes/Mueller polarimeter design by the use of a genetic algorithm," *Opt. Express* **18**, 23095–23103 (2010).
26. J. H. Holland, "Genetic algorithms," *Sci. Am.* **267**, 44–50 (1992).
27. D. Floreano and C. Mattiussi, *Bio-Inspired Artificial Intelligence: Theories, Methods, and Technologies* (The MIT Press, 2008).
28. E. Compain, S. Poirier, and B. Drevillon, "General and self-consistent method for the calibration of polarization modulators, polarimeters, and mueller-matrix ellipsometers," *Appl. Optics* **38**, 3490–3502 (1999).
29. S. B. Hatit, M. Foldyna, A. De Martino, and B. Drevillon, "Angle-resolved Mueller polarimeter using a microscope objective," *Phys. Stat. Sol. (a)* **205**, 743–747 (2008).
30. A. Ben-Israel and T. N. E. Greville, *Generalized Inverses: Theory and Applications* (Springer-Verlag, 2003).
31. R. Hagen, S. Roch, and B. Silbermann, *C\* Algebras Numerical Analysis* (Marcel Dekker, 2001).
32. L. Aas, P. Ellingsen, M. Kildemo, and M. Lindgren, "Dynamic Response of a fast near infra-red Mueller matrix ellipsometer," *J. Mod. Opt.* **57**, 1603–1610 (2010).
33. C. S. Perone, "Pyevolve," <http://pyevolve.sourceforge.net/>.

## 1. Introduction

Polarimeters measure the polarization state of electromagnetic waves. Methods based on polarimetry are thus non-invasive and have the possibility for remote sensing applications, which makes them attractive in many fields of science. In the range of optical frequencies, polarimetry has proven to be useful and promising in e.g. biomedical diagnostics [1–3], remote sensing [4] and astronomy [5]. The sample measuring polarimeter (ellipsometer) is a key characterization technique for thin films [6–8], with recent applications to e.g. gratings [9], nanostructures [10–12], plasmonics [13], metamaterials [14] and scattering from rough surfaces [15–17].

A Mueller matrix ellipsometer/polarimeter consists of a complete polarization state generator (PSG) and polarization state analyzer (PSA), which determines all the polarization altering properties of a sample both in reflection and in transmission. A Stokes polarimeter consist only of a PSA and is used to determine the complete polarization state of partially polarized light.

A PSA/PSG generally consists of a diattenuating polarizer and an active birefringent optical component either modulated by azimuthal rotation or by an externally applied electric field [18]. Typical examples are rotating (wave-plate/bi-prism) retarders [6, 19], electro-optical modulation [20], photoelastic modulators [21, 22], and liquid crystal retarders [23, 24]. Disper-

sion in the optical components is usually limiting the wavelengths range of the polarimeters, but novel system designs may overcome this problem for at least a limited spectral range [23].

Certain wide band achromatic polarimeters (from the ultraviolet to the infrared) may be constructed using near non-dispersive retarders, by exploiting the total internal reflection from Fresnel prisms [19]. These retarders do commonly have a small aperture, are sensitive to alignment and require mechanical azimuth rotation for operation, and are thus not really suitable for imaging and space applications. On the other hand, liquid crystal retarders have no moving parts and can easily be made with large apertures, but they are strongly dispersive and a liquid crystal based wide band polarimeter requires a more advanced design.

A common way of designing polarimeters with dispersive components, is to first choose components based on a previous design or use a qualified guess. Secondly, the orientations of the components and the electrically controlled states are estimated by a local exhaustive or a gradient search. Due to a large search space, these latter search methods are computationally expensive and require particularly good starting guesses in order not to converge to a local minimum. Furthermore, for liquid crystal based wide spectral range multichannel polarimeters, it is necessary to add more modulating components [25], or states in the original components, in order to improve the conditioning of the system. The polarization state measurement is then said to be overdetermined. This makes the system design even more complex, due to the addition of more dimensions to the search space, hence requiring an efficient design algorithm [25].

Evolutionary algorithms are inspired by how nature evolves and how natural selection occurs. Genetic algorithms [26] are a subcategory of these and are based on the use of a genome, commonly a series of binary numbers, to evaluate, breed and compare different solutions. Genetic algorithms have proven to be effective at solving certain types of problems and are especially effective in large search spaces with a number of local minima. However, it is important to note that the algorithm does not search every solution and it cannot be guaranteed that the global optimum is found, though with well configured parameters it should be a good one [27].

Advantages of overdetermined polarimeters and the use of genetic algorithms to design them, was proven theoretically for a broadband system based on ferroelectric liquid crystal components in [25]. The genetic algorithm was generically implemented in order to create designs using any polarization modulating component with known dispersive properties. We here report for the first time an experimental implementation and testing of a genetic algorithm designed wide-band liquid crystal variable retarder Mueller matrix polarimeter.

## 2. Theory

Let us first briefly review the theory and notation used to describe the measurement of Stokes vectors and Mueller matrices using a PSA and a PSG, both for determined and overdetermined systems. The calibration of overdetermined Mueller matrix polarimeters is thereafter explained using a generalization of the eigenvalue calibration method (ECM) [28].

The polarization state of light, can generally be represented in vector form by the four element Stokes vector defined by

$$\mathbf{S} = \begin{bmatrix} s_1 \\ s_2 \\ s_3 \\ s_4 \end{bmatrix} = \begin{bmatrix} \langle E_x(t)^2 \rangle + \langle E_y(t)^2 \rangle \\ \langle E_x(t)^2 \rangle - \langle E_y(t)^2 \rangle \\ 2 \langle E_x(t) E_y(t) \cos \delta(t) \rangle \\ 2 \langle E_x(t) E_y(t) \sin \delta(t) \rangle \end{bmatrix},$$

where  $E_x(t)$  and  $E_y(t)$  are time dependent, electric field amplitudes of the  $x$ - and  $y$ -components, of an electric field propagating in the  $z$ -direction.  $\langle \cdot \rangle$  denotes time averages and  $\delta(t)$  is the time dependent phase difference between the  $x$ - and  $y$ -components of the

electric field. Note that the averaging of time varying amplitudes and phases, results in a reduced degree of polarization.

The Mueller matrix is a  $4 \times 4$  transfer matrix transforming an initial Stokes vector to the final by  $\mathbf{S}_{\text{final}} = \mathbf{M}_{\text{sample}} \mathbf{S}_{\text{initial}}$ . A Mueller matrix can describe all changes in the polarization state of light upon the interaction with a sample, with quantifiable effects, like for instance polarizance, diattenuation, retardance and depolarization [18].

In order to measure  $\mathbf{M}$ , one needs at least four probing Stokes vectors [18]. Consequently these Stokes vectors need to be measured by a polarimeter/PSA. A polarimeter/PSA projects the incoming intensity to at least four carefully selected polarization states. These states are the Stokes vectors in the PSA, organized into the rows of the PSA matrix  $\mathbf{A}$ . The intensity vector,  $\mathbf{b} = \mathbf{A}\mathbf{S}$ , for an incoming Stokes vector can then be measured, and the Stokes vector found by inversion;  $\mathbf{S} = \mathbf{A}^{-1}\mathbf{b}$ . Similarly, for the PSG in the Mueller matrix polarimeter/ellipsometer, the generated Stokes vectors are organized as columns in the  $\mathbf{W}$  matrix. The product  $\mathbf{M}\mathbf{W}$  gives the Stokes vectors for the PSA to analyze, yielding the total intensity measurement matrix  $\mathbf{B} = \mathbf{A}\mathbf{M}\mathbf{W}$ . As a result, the Mueller matrix can then, in principle, readily be calculated by inversion of  $\mathbf{A}$  and  $\mathbf{W}$ ,  $\mathbf{M} = \mathbf{A}^{-1}\mathbf{B}\mathbf{W}^{-1}$ . There are several ways of finding  $\mathbf{A}$  and  $\mathbf{W}$  for a system, but a common method is the robust and increasingly popular ECM [28]. It uses the measurement of a set of calibration samples to account for all systematic errors, such as alignment errors and time/temperature dependent variations in components of the system [23,24,29]. Prior knowledge is only required for the form of the reference sample Mueller matrix (i.e. if it is a polarizer or retarder) and an initial qualified guess of the azimuth orientation, for solving the system with the ECM. In our case,  $\mathbf{A}$  and  $\mathbf{W}$  result from six states in the PSA and PSG, corresponding to 12 specific Stokes vectors  $\mathbf{S}_{W1-6}$  and  $\mathbf{S}_{A1-6}$

$$\begin{aligned}\mathbf{W} &= [\mathbf{S}_{W1}, \mathbf{S}_{W2}, \mathbf{S}_{W3}, \mathbf{S}_{W4}, \mathbf{S}_{W5}, \mathbf{S}_{W6}], \\ \mathbf{A} &= [\mathbf{S}_{A1}, \mathbf{S}_{A2}, \mathbf{S}_{A3}, \mathbf{S}_{A4}, \mathbf{S}_{A5}, \mathbf{S}_{A6}]^T.\end{aligned}$$

The ECM is explained in the original paper [28] for systems using four Stokes vectors in the PSG and PSA. Here we present the generalization needed to calibrate a system with  $n$  Stokes vectors in the PSA and  $m$  Stokes vectors in the PSG. We start with a set of reference Mueller matrices,  $\{\mathbf{M}\}$ , corresponding to a set of intensity measurements,  $\{\mathbf{B}\}$ .  $\mathbf{B}_i$  is of size  $n \times m$  and is given by

$$\mathbf{B}_i = \mathbf{A}\mathbf{M}_i\mathbf{W}.$$

For convenience, reference sample  $\mathbf{M}_0$  is chosen to be air, such that  $\mathbf{B}_0 = \mathbf{A}\mathbf{W}$ . Next, two sets of matrices,  $\{\mathbf{C}\}$  and  $\{\mathbf{C}'\}$ , are constructed using

$$\mathbf{C}_i = \mathbf{B}_0^\dagger \mathbf{B}_i = \mathbf{W}^\dagger \mathbf{M}_i \mathbf{W} \quad \text{and} \quad \mathbf{C}'_i = \mathbf{B}_i \mathbf{B}_0^\dagger = \mathbf{A} \mathbf{M}_i \mathbf{A}^\dagger, \quad (1)$$

where  $^\dagger$  denotes the Moore-Penrose pseudoinverse, which is the common way of defining the inverse of a non-square matrix with noise [30]. In the case where  $\mathbf{B}_i$  is of size four by four, the sets  $\{\mathbf{C}\}$  and  $\{\mathbf{C}'\}$  have the same eigenvalues as the set of Mueller matrices  $\{\mathbf{M}\}$ . As  $\mathbf{C}_i$  is independent of  $\mathbf{A}$ , and  $\mathbf{C}'_i$  is independent of  $\mathbf{W}$ ,  $\mathbf{A}$  and  $\mathbf{W}$  may be found independently, and  $\{\mathbf{M}\}$  may be found both from  $\{\mathbf{C}\}$  and  $\{\mathbf{C}'\}$  independently.

In an overdetermined system  $\mathbf{C}_i$  and  $\mathbf{C}'_i$  holds more eigenvalues than the corresponding Mueller matrix  $\mathbf{M}_i$ . One way of finding which of the eigenvalues that correspond to the Mueller matrix  $\mathbf{M}_i$ , is to do a search in the eigenvalues of  $\mathbf{C}_i$  and  $\mathbf{C}'_i$  and compare them with expected values. However, in a real measurement including noise, the latter approach did in our experience not appear robust. The noise is related to the relative error in  $\mathbf{M}$ , shown by Stabo-Eeg et



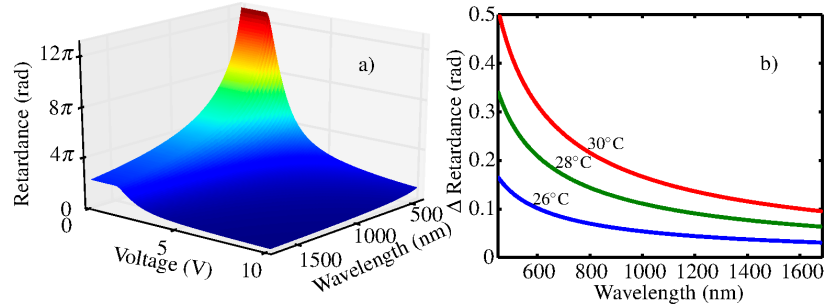


Fig. 1. (a) The measured retardance of a LCVR as a function of wavelength and the voltage applied. (b) The retardance of the LCVR measured at 0 V with the temperature stabilized at 26°C, 28°C and 30°C. The figure shows the relative difference to the LCVR retardance at 24°C.

al. [19] to be

$$\frac{\|\Delta \mathbf{M}\|}{\|\mathbf{M}\|} \lesssim \kappa_W \kappa_A \frac{\|\Delta \mathbf{B}\|}{\|\mathbf{B}\|} + \kappa_A \frac{\|\Delta \mathbf{A}\|}{\|\mathbf{A}\|} + \kappa_W \frac{\|\Delta \mathbf{W}\|}{\|\mathbf{W}\|}, \quad (2)$$

where  $\kappa_W$  and  $\kappa_A$  are the condition numbers of  $\mathbf{W}$  and  $\mathbf{A}$  respectively. For a square non-singular matrix the condition number is defined as  $\kappa_A = \|\mathbf{A}\| \|\mathbf{A}^{-1}\|$ , while for a non-square matrix the generalized condition number is given by  $\kappa_A = \|\mathbf{A}\| \|\mathbf{A}^\dagger\|$  [31], where  $\|\cdot\|$  denotes the second norm of the matrix. From Eq. (2) it is seen that in order to minimise the noise in  $\mathbf{M}$ , it is necessary to reduce the condition numbers of  $\mathbf{A}$  and  $\mathbf{W}$ .

A robust solution to finding the correct eigenvalues of  $\{\mathbf{M}\}$  from  $\{\mathbf{C}\}$  and  $\{\mathbf{C}'\}$ , is to (at each wavelength) reduce  $\mathbf{B}_0$  and  $\mathbf{B}_i$  in Eq. (1) to the  $4 \times 4$  subset of  $\mathbf{B}_0$  and  $\mathbf{B}_i$  resulting in the lowest condition number for the reduced  $\mathbf{B}_0$ . When inverting  $\mathbf{B}_0$ , this ensures minimal noise propagation into  $\mathbf{C}_i$  and to the eigenvalues of  $\mathbf{M}_i$ . After finding the eigenvalues of  $\{\mathbf{M}\}$ , the remainder of the calibration procedure follows the original paper by Compain et al. [28], using the non reduced  $\{\mathbf{B}\}$ .

Also worth noting is that the noise equation, Eq. (2), is the basis for the genetic optimisation, which tries to maximise the inverse condition number.

### 3. Experimental

The essential optical components in the Mueller matrix polarimeter presented here, are polarizers and liquid crystal variable retarders (LCVR). In the calibration, a polarizer and a waveplate was used. We used a high extinction ratio near infra-red polarizer (*LPNIR*) from *Thorlabs* and a true zero-order quarter waveplate at 1310 nm from *Casix*. The LCVRs were custom made for the near infrared from *Meadowlark Optics*.

LCVRs are wave retarders having the retardance as a function of applied voltage. Compared to ferroelectric liquid crystal retarders (previously proposed overdetermined polarimeter design [25]) which have only one fixed retardance, but with two stable azimuth orientations, they typically have much longer transition times between two states [32], but have the advantage of allowing the selection of all retardation values between a maximum and minimum value.

In order to design the optimal polarimeter, the retardance as a function of voltage and wavelength needs to be known with reasonable precision. Although the calibration routine handles small deviations in dispersive optical properties, high accuracy of the Mueller matrix elements

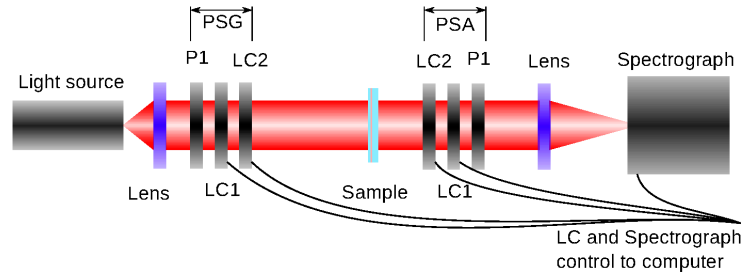


Fig. 2. Schematic drawing of a typical spectroscopic Mueller matrix polarimeter using liquid crystal variable retarders (LCVR), a broad band light source and spectrometer.

is only insured as long as the condition number is not strongly degraded with respect to the design. In the instrument reported here, it was also found that there were, due to manufacturing uncertainties, differences in thickness between the individual crystals. The crystals were therefore characterized individually in the range of 450 – 1680 nm using a commercial available Mueller matrix polarimeter *RC2* from *J.A. Woollam Co.*. Figure 1(a) shows as an example, a surface plot of the resulting retardance as a function of voltage and wavelength for one of the LCVRs. It is noted that for lower voltages the retardance reaches a threshold at the critical voltage 1.5 V, while it approaches a low residual retardance for high voltages. The large retardance in the visible insures the possibility for a reasonable retardance variation in the longer wavelengths of the NIR spectrum.

It was found that the retardance was reduced significantly with the increased ambient temperature. Figure 1(b) shows the deviation in the wavelength dependent retardance for 26°C, 28°C and 30°C, relative to the retardance at 24°C at 0 V. Thus, for reproducible and accurate measurements, the LCVRs must be operated in an environment with a stable temperature.

Figure 2 shows a schematic drawing of a typical LCVR Mueller matrix polarimeter system design, based on a broadband white light source, a spectrograph and four temperature controlled LCVRs. The polarizer and the two crystals on the left side of the sample makes up the PSG, while the components in the opposite order on the right side of the sample makes up the PSA (i.e. a Stokes polarimeter).

The system design was done using a genetic algorithm based on the *Pyevolve* library [33]. The algorithm tries to maximize a fitness function, which was defined as

$$f = \frac{1}{e},$$

where  $e$  is the error function defined as

$$e = \sum_{n=1}^{N_\lambda} \left( \frac{1}{\sqrt{3}} - \frac{1}{\kappa(\lambda_n)} \right)^4.$$

Here  $N_\lambda$  is the total number of wavelengths and  $\kappa(\lambda_n)$  is the generalized condition number of  $\mathbf{A}$  or  $\mathbf{W}$  for a given wavelength  $\lambda_n$ . This fitness function is similar to the one previously defined in [25] and incorporates experimentally measured optical properties of the components using the Mueller formalism to calculate the generalized condition number of  $\mathbf{A}$  or  $\mathbf{W}$ . As for the previous fitness function, it punishes inverse condition numbers far away from the theoretical maximum inverse condition number ( $1/\sqrt{3}$ ), by taking the difference to the fourth power. Fi-

nally, it is noted that since the genetic algorithm is based on bit strings, the conversion from bits to numbers will not always yield a voltage, or wavelength where the LCVRs were experimentally characterized, in these cases the closest measured retardance value was used.

The genetic optimization was performed using the settings given in Table 1. 8 bits was considered sufficient to represent the voltage and the rotation angle, i.e. a step size of 0.04 V and  $0.7^\circ$ . The wavelength range was selected to be 900 – 1700 nm, the range of a typical indium gallium arsenide (InGaAs) near infrared detector. In particular, we used the *NirQuest512* spectrograph from *Ocean Optics*. The number of generations, population size and mutation rate were found by trial and error, by encouraging diversity and avoiding formation of large groups of individuals focused around one minimum. Elitism (copying of the best individual from one generation to the next), two point crossover and tournament were also used.

Table 1. General settings for the genetic optimization

Property	Values
Voltage bits per LCVR	8
Rotation bits per LCVR	8
Wavelength range	850 – 1700 nm in 200 equal steps
Number of generations	500
Population size	200
Crossover method	Two point crossover
Crossover rate	70%
Selection method	Tournament with 4 individuals
Elitism	The best individual
Mutation rate	4%

#### 4. Results and discussion

Several Mueller matrix polarimeters were optimized in order to cover the near infrared spectral range. By using two LCVRs in both the PSG and the PSA, one may in principle generate a large number of states. However, a system that approaches the theoretically optimal inverse condition number  $1/\sqrt{3}$  will need 16 states for every measured wavelength, as long as a retardance of  $\pi/2$  is available. For a large number of wavelengths (typically  $> 500$ ), such a system results in an unreasonable high total measurement time. Therefore, several Mueller matrix polarimeters were designed and evaluated with only a limited number of states in the PSG and the PSA, in order to keep the measurement time low. Three Mueller matrix polarimeter designs were optimized and evaluated. All designs used an equal number of states in the PSG and the PSA. The first design used two states in each of the LCVRs, totaling 4 ( $2 \times 2$ ) states for the PSA or the PSG, and 16 ( $4^2$ ) states for the complete system. The second design had two states in the first LCVR and three in the second LCVR, totaling 6 ( $2 \times 3$ ) states for the PSA/PSG and 36 ( $6^2$ ) in the complete system. Similarly the last design had two states in the first and four in the second LCVR, resulting in a total of 8 ( $2 \times 4$ ) states for the PSA/PSG, and 64 ( $8^2$ ) for the complete polarimeter. For simplicity, these three designs will from now on be denoted as  $2 \times 2$ ,  $2 \times 3$  and  $2 \times 4$ . The resulting designs are summarized in Table 2, whereas the resulting inverse condition numbers are shown in Fig. 3. It is evident that by going from a  $2 \times 2$  to a  $2 \times 3$  design the condition number is increased on the two edges of the spectrum. By moving to  $2 \times 4$  states, the condition number increases over the whole spectrum. It is clear that there will be a trade-off between the measurement time and the gain in the increased condition number, and hence the

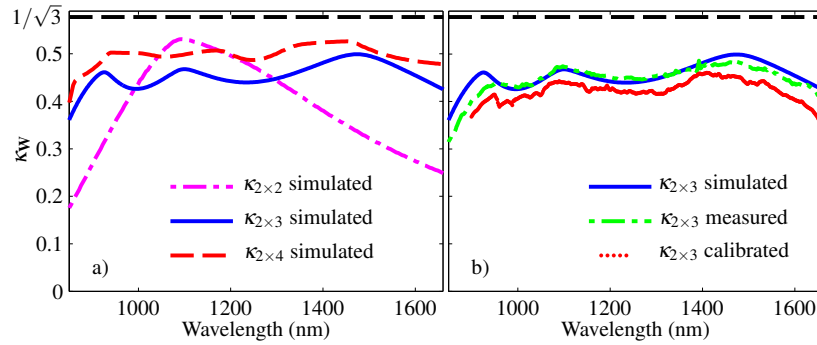


Fig. 3. The inverse of the generalized condition number of  $\mathbf{W}$  as a function of wavelength. Figure (a) shows the comparison between the best designs for a  $2 \times 2$ ,  $2 \times 3$  and  $2 \times 4$  states system, where the systems are presented in terms of the number of retardance (voltage) states for each of the two LCVRs making up the PSG or the PSA. Figure (b) shows both the simulated, measured and calibrated inverse condition number of the experimentally realized polarimeter with  $2 \times 3$  states.

noise reduction at the edges of the spectrum. As a compromise, we found it practical to use the  $2 \times 3$  design for the experimental realization of the Mueller matrix polarimeter.

Table 2. Configuration of the optimal polarimeters

Component property	Polarimeter type		
	$2 \times 2$	$2 \times 3$	$2 \times 4$
Orientation of LCVR1 ( $^\circ$ )	135.5	40.9	60.7
Orientation of LCVR2 ( $^\circ$ )	112.9	105.7	101.6
Voltages of LCVR1 (V)	3.6, 9.7	3.8, 9.9, 2.8	3.7, 1.6, 2.6, 2.1
Voltages of LCVR2 (V)	2.6, 6.8	2.9, 8.8	8.5, 2.7

In comparison to previously reported ferroelectric liquid crystal (FLC) designs [25] obtained using a similar genetic algorithm, the  $2 \times 3$  LCVR design has a much narrower wavelength range and a slightly lower inverse condition number. This is as expected, since the design using three FLCs has three compensating wave-plates in addition to the liquid crystals, giving extra degrees of freedom. Specifically, these degrees of freedom arise from the fact that both the thickness (birefringence) and the azimuthal orientation of each component can be selected, and as a result one would expect an overall higher inverse generalized condition number. However, more optical components reduce the transmitted intensity, which in some cases results in a greatly reduced signal to noise ratio. A high signal to noise ratio is particularly important for applications with a limited flux, for example a large field of view imaging or space applications.

The  $2 \times 3$  design was mounted in custom made temperature controlled holders, one for the PSG and one for the PSA. These were then separately mounted in the beam-path of the RC2, and by switching through all the  $2 \times 3$  states of the LCVRs, the Stokes vectors of the  $\mathbf{W}$  and  $\mathbf{A}$  matrix was determined in the range 350 – 1680 nm, by selecting the first column of the measured Mueller matrix. The resulting inverse generalized condition number is shown in Fig. 3(b) (in green stippled lines), together with the simulated inverse generalized condition number

resulting from the design obtained by the genetic algorithm (solid line). As seen, the correspondence between the experimental and simulated inverse generalized condition numbers is excellent. This demonstrates the power of such a system design and implementation, utilizing genetic algorithms and re-characterization of the optical components after arrival. The PSG and the PSA were then mounted in the transmission geometry shown in Fig. 2, making up the complete LCVR based Mueller matrix polarimeter.  $\mathbf{A}$  and  $\mathbf{W}$  were found using the ECM, as discussed in section 2. The generalized condition number of the calibrated  $\mathbf{W}$  matrix is plotted in Fig. 3(b). It is observed from the figure that the general spectral features in the optimized condition number are reproduced in the experimental version, although it suffers from small offsets in some parts of the spectrum. The latter offsets are possible due to that the components of the PSA/PSG were slightly realigned between the measurement using the commercial Mueller matrix ellipsometer compared to the final implementation of the LCVR Mueller matrix polarimeter. On the other hand, it shows that the modified ECM automatically compensates for alignment errors during assembly, and the final system calibrates correctly with only minor changes in the propagation of noise.

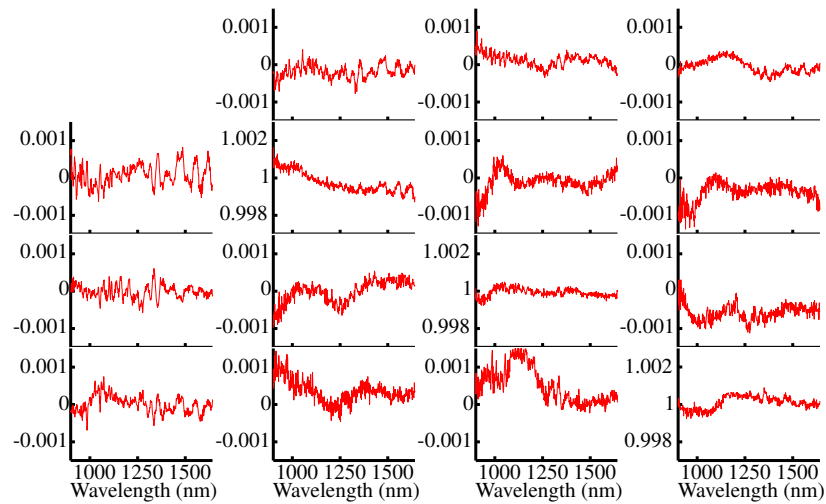


Fig. 4. The measured spectroscopic Mueller matrix of air normalized to the  $m_{11}$  element.

An important measure of the Mueller matrix polarimeter accuracy is the measurement of air, whose Mueller matrix is simply the  $4 \times 4$  identity matrix. Figure 4 shows the spectroscopic Mueller matrix measurement of air (normalized to the  $m_{11}$  element). The deviation from the identity matrix is small, since the error is less than 0.1% over most of the spectrum, and is never more than 0.17%.

It is recalled that the wide band LVCR design uses few components and thereby has small reflection losses from the optical interfaces. Hence, the designed Mueller matrix polarimeter should also be well suited for a fast imaging setup with low loss of light, compared to a FLC based setup, while insuring small measurement errors across the spectral range of operation, even suitable for hyperspectral imaging. The reduction in number of components also enables a more compact design. Another advantage of the setup will be the possibility to redesign the spectral characteristics without having to rotate the components, since the voltage of the LCVRs

is software controlled. By using the genetic algorithm, it is possible to fix the rotation angles and only optimize on the LVCR voltage in order to fulfill other system specifications. Finally, one may envisage a system that can improve itself by self-characterization and intelligent design by implementing an in-line version of the genetic algorithm.

## 5. Conclusion

Genetic algorithms have been used to design multichannel Mueller matrix polarimeters based on liquid crystal variable retarders for the near infrared with  $2 \times 2$ ,  $2 \times 3$  or  $2 \times 4$  voltage states for the polarization state generator and analyzer. The design using  $2 \times 3$  states was experimentally realized and calibrated, based on its advantageous trade-off between total measurement time and overall performance with respect to error propagation (optimized inverse condition number). The resulting Mueller matrix polarimeter demonstrated here, shows good performance in the design wavelength range (900-1700 nm) with less than 0.1% error on the Mueller matrix of air, making it suitable in for example hyperspectral or multispectral imaging applications.

## Acknowledgment

L.M.S.A acknowledges support from The Norwegian Research Center for Solar Cell Technology (project num. 193829).

L. M. S. Aas, P. G. Ellingsen, M. Kildemo, and M. Lindgren, “Dynamic response of a fast near infra-red Mueller matrix ellipsometer,” *J. Mod. Opt.* **57**(17), 1603–1610 (2010)

## **Paper 3**





## Dynamic response of a fast near infra-red Mueller matrix ellipsometer

Lars M.S. Aas\*, Pål G. Ellingsen, Morten Kildemo and Mikael Lindgren

Department of Physics, Norwegian University of Science and Technology (NTNU),  
N-7491 Trondheim, Norway

(Received 8 June 2010; final version received 26 July 2010)

The dynamic response of a near infra-red ferroelectric liquid crystal-based Mueller matrix ellipsometer (NIR FLC-MME) is presented. A time-dependent simulation model, using the measured time response of the individual FLCs, is used to describe the measured temporal response. Furthermore, the impulse response of the detector and the pre-amplifier is characterized and included in the simulation model. The measured time-dependent intensity response of the MME is reproduced in simulations, and it is concluded that the switching time of the FLCs is the limiting factor for the Mueller matrix measurement time of the FLC-based MME. Based on measurements and simulations, our FLC-based NIR-MME system is estimated to operate at the maximum speed of approximately 16 ms per Mueller matrix measurement. The FLC-MME may be operated several times faster, since the switching time of the crystals depends on the individual crystal being switched, and to what state it is switched. As a demonstration, the measured temporal response of the Mueller matrix and the retardance of a thick liquid crystal variable retarder upon changing state is demonstrated.

**Keywords:** Mueller matrix; ellipsometer; polarimeter; near infra-red; FLC

### 1. Introduction

Fast Mueller matrix ellipsometers (MME) may have a wide range of applications in biology, medicine, and various monitoring and control systems, supplying additional polarimetric information in imaging and spectroscopic applications. A variety of high performance MMEs has been reported [1–8], but they are usually of considerable complexity or not suitable for use with CCD or CMOS stripe-spectrographs and imaging sensors. We are also considering the limit of non-reversible processes not covered by, for example, the pump-probe techniques used for ultrafast birefringence or dichroism measurements. Some authors have reported on fast Mueller matrix measurements [1–2,9,10]. A typical solution uses a division of amplitude polarimeter and four detectors to work as the polarimeter or polarization state analyzer (PSA). The modulation may be performed with a fast electro-optic [1,3] or photo-elastic modulator [2]. However, such systems require a considerable increased complexity in instrumentation and signal processing. A recent development is the Snapshot Mueller matrix polarimeter based on spectral polarization coding, which enables Mueller matrix measurements within a microsecond [9,10]. However, this system does not allow for spectroscopic measurements, as the technique requires small spectral variations in the Mueller matrix of the sample. A rotating Fresnel prism retarder with a

retardation of  $132^\circ$  across a wide spectral range (including UV) is probably the most optimal conditioned system around [5,11]. However, the latter system is inherently slow due to the mechanical rotation of the retarders, thus making it less suitable for fast MME purposes.

Liquid crystal (LC) spatial light modulators have been developed over the past decades for a variety of applications. The LCs are of course most widely used in display applications where the amplitude mode of operation is desired, but phase control can be used in, for example, beam-steering and shaping [12–13], adaptive optics [14], optical tweezers [15], to mention a few. The ferroelectric LCs are fast and allow for a rapid determination of the Mueller matrix. Several FLC-based MME designs have been proposed, although the first proposal of a polarimeter system similar to the one reported on here, appears to have been by Gandorfer and co-workers [16]. However, as shown here, the FLCs are still the limiting factor for the switching speeds, contrary to the findings reported recently [17,18]. The main disadvantage of liquid crystals, and in particular the current FLCs, is the well known degradation of the crystals upon ultra-violet radiation [19]. Applications of this technology in MME are currently thus limited to the visible and the infra-red. In this paper we investigate the dynamic response of a novel NIR-MME operating from 700

\*Corresponding author. Email: lars.aas@ntnu.no

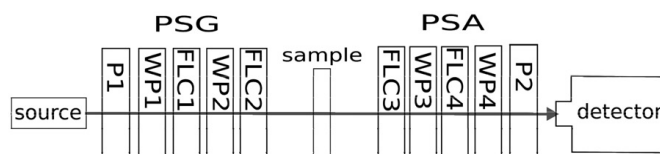


Figure 1. Layout of the FLC-based NIR-MME studied in this paper. The source is either a tungsten halogen white incoherent source or a 980 nm diode laser source. The FLC switching, timing and the signal acquisition are controlled through a computer. The optical components are ordered as a polarizer (P1), quartz waveplate (WP1), ferroelectric liquid crystal 1 (FLC1), waveplate (WP2), sample (e.g. air), FLC3, waveplate (WP3), FLC4 and waveplate (WP4). The details of the optical components are given in Table 1.

to 1600 nm. In a follow up paper we report on the features and applications of a FLC-based NIR-MME imaging system based around the same design.

A key issue when designing a Mueller matrix ellipsometer is optimization of the modulation or analyzer matrix of a polarization state generator (PSG) or a PSA in terms of their matrix condition number [5,11–12]. In this respect, the variable liquid crystal retarder (VLCR) based Mueller matrix ellipsometer can be truly optimal, but only for a single wavelength at a time. Furthermore, the switching of a VLCR is slow compared with the FLC variant. In fact, the dynamic possibilities of the fast near infra-red ferroelectric liquid crystal-based MME are here demonstrated by characterization of the dynamic Mueller matrix of a VLCR during the switching.

## 2. Experimental details

The NIR-MME reported on here can be operated in spectroscopic mode from 750 nm to 1800 nm, using a grating monochromator and a single detector. A tungsten-halogen lamp (100 W) with a stabilized power supply was used for incoherent illumination. The system is alternatively operated by using a stable laser diode operating at 980 nm, with maximum output power of 300 mW (found particularly useful for high speed measurements with short integration time).

A purpose-built (by Elektron Manufaktur Mahlsdorf) extended InGaAs detector with a built-in pre-amplifier, having an overall well-designed flat frequency response and cut-off frequency at 150 kHz, was used in the spectroscopic mode.

A multifunctional NI-DAQ card with a maximum sampling rate of 1.25 Ms/s (mega samples per second), is both used to acquire measurements and to control the FLCs. The MME is operated with in-house made Labview-based software. The initial FLC-based MME design was chosen based on the design by Gandorfer and co-workers [16], and similar designs have later been reported elsewhere [7,18]. In particular, Gandorfer and co-workers proposed a sequence of

components such that the PSG and the PSA are composed of a polarizer – fixed waveplate (WP1) – ferroelectric liquid crystal (FLC1) – WP2 – FLC2. The remaining problem is then to determine the retardances and orientations of the waveplates and FLCs in order to optimize the condition number over the design spectral region. The PSA is, in this initial design, simply chosen with identical components in reverse order. Figure 1 shows a schematic drawing of the design.

The optical components in our design consist of a high contrast dichroic NIR polarizer, followed by a fixed ‘true zero-order’ quarter-wave retarder at 465 nm, a half-wave FLC at 510 nm, a fixed half-wave retarder at 1008 nm, and finally a half-wave FLC at 1020 nm. The true zero-order waveplates were manufactured in quartz, while the FLCs were custom-made versions of commercially available crystals (Displaytech Inc). The FLCs at 510 nm were the only elements fixed in the optimization, and originally chosen simply from cost considerations, while the fitted thicknesses of the remaining waveplates are the results of an optimization with respect to the condition number across the design spectral range.

The calibration samples were chosen as two NIR polarizers (similar to above) with azimuth orientation  $0^\circ$  and  $90^\circ$  relative to the first polarizer, and a zero-order waveplate at 1310 nm with azimuth orientation of the fast axis at  $60^\circ$  [18].

All the components were characterized individually, including retardance and azimuth orientation. The measurements were performed with collimated light and normal incidence to the optical polarization components. Simulation of the optical response of the full FLC-based Mueller matrix ellipsometer was compared to the measured response, using the characteristic properties of each characterized component.

Measurements were performed on air, and on a custom-made version of a commercially available VLCR (Meadowlark Inc.). The VLCR was designed to be a half-wave retarder at 2200 nm.

**3. Mueller matrix theory for FLC-based MME**

The MME is constructed by considering the Mueller matrix measurement theory proposed by Compain and colleagues [2,20,22–23]. In particular, the intensity matrix (**B**), which contains the 16 measured intensities, is given by the matrix product of the modulation matrix (**W**), the sample Mueller matrix (**M**) and the analyzer matrix (**A**)

$$\mathbf{B} = \mathbf{A}\mathbf{M}\mathbf{W}. \tag{1}$$

From the measured **B** matrix, and the known **W** and **A** matrices, the Mueller matrix can readily be calculated by matrix multiplication

$$\mathbf{M} = \mathbf{A}^{-1}\mathbf{B}\mathbf{W}^{-1}. \tag{2}$$

It is evident from basic matrix theory that **W** and **A**, for minimal error propagation, need to be as invertible as possible, i.e. as far from singular as possible. Specifically, it has been shown that the error in the intensity measurements, the calibration errors on **A** and **W**, are summed into the errors in the resulting Mueller matrix as follows [5]

$$\frac{\|\Delta\mathbf{M}\|}{\|\mathbf{M}\|} \leq \kappa_A \frac{\|\Delta\mathbf{A}\|}{\|\mathbf{A}\|} + \kappa_W \frac{\|\Delta\mathbf{W}\|}{\|\mathbf{W}\|} + \kappa_A\kappa_W \frac{\|\Delta\mathbf{B}\|}{\|\mathbf{B}\|}, \tag{3}$$

where  $\kappa_A$  and  $\kappa_W$  are the condition numbers of **A** and **W**, defined in our work by the  $L_2$  norm. This particular design method was originally proposed by Tyo [21], and later implemented and further developed by Compain and colleagues [1]. Compain and colleagues suggested an efficient and robust calibration technique (denoted the Eigenvalue Calibration Method) [20], which is also implemented here in order to determine the matrices **A** and **W**.

The modulation matrix **W** is constructed by defining each column vector as a unique Stokes vector generated by switching the two FLCs to one of their four different states. Let

$$\hat{\theta} = \{\theta_{1,FLC1}, \theta_{2,FLC1}, \theta_{1,FLC2}, \theta_{2,FLC2}, \theta_{1,FLC3}, \theta_{2,FLC3}, \theta_{1,FLC4}, \theta_{2,FLC4}\} \tag{4}$$

describe the set of azimuth angles of the FLCs. The two stable states  $\{\theta_{1,j}, \theta_{2,j}\}$  of crystal  $j$ , are nominally separated by  $45^\circ$  in this work. The modulation matrix is then given by

$$\mathbf{W} = [\vec{S}_1 \quad \vec{S}_2 \quad \vec{S}_3 \quad \vec{S}_4], \tag{5}$$

where each stokes vector  $\vec{S}_k$  is generated as:

$$\begin{aligned} \vec{S}_k &= \vec{S}(\lambda, \hat{\theta}) \\ &= \mathbf{M}_{ret}(\theta_{i,FLC2}, \delta_{FLC2}(\lambda), T_{f,s})\mathbf{M}_{ret}(\theta_{WP2}, \delta_{WP2}(\lambda), T_{f,s}) \\ &\quad \times \mathbf{M}_{ret}(\theta_{j,FLC1}, \delta_{FLC1}(\lambda), T_{f,s}) \\ &\quad \times \mathbf{M}_{ret}(\theta_{WP1}, \delta_{WP1}(\lambda), T_{f,s})\mathbf{M}_{pol}[1 \quad 0 \quad 0 \quad 0]^t \end{aligned} \tag{6}$$

where  $\mathbf{M}_{ret}$  are the Mueller matrices of the retarders, oriented at a given angle  $\theta$  with respect to the first polarizer (here used as a laboratory axis reference) with retardance  $\delta$ .  $\mathbf{M}_{pol}$  is the matrix of the polarizer horizontally aligned in our system. The index  $i$  denotes the state of FLC2, and  $j$  denotes the state of FLC1.

Similarly, the analyzer matrix is composed of the discrete analyser states

$$\mathbf{A} = [\vec{A}_1 \quad \vec{A}_2 \quad \vec{A}_3 \quad \vec{A}_4]^T. \tag{7}$$

Each analyzer state is then calculated as above, taking into account the reverse order of the optical components, resulting in

$$\begin{aligned} \vec{A}_k &= \vec{A}(\lambda, \hat{\theta}) = [1 \quad 0 \quad 0 \quad 0]^t \mathbf{M}_{pol}\mathbf{M}_{ret}(\theta_{i,FLC4}, \delta_{FLC4}(\lambda)) \\ &\quad \times \mathbf{M}_{ret}(\theta_{WP4}, \delta_{WP4}(\lambda))\mathbf{M}_{ret}(\theta_{j,FLC3}, \delta_{FLC3}(\lambda)) \\ &\quad \times \mathbf{M}_{ret}(\theta_{WP3}, \delta_{WP3}(\lambda)). \end{aligned} \tag{8}$$

The index  $i$  denotes the two stable states of FLC3, while  $j$  denotes the two stable states of FLC4.

**4. Results and discussion**

**4.1. Static polarization properties of the optical components and the MME system**

The current version of our NIR-MME system has the characteristics summarized in Table 1, where all orientations of the polarizers, waveplates and the FLCs were individually determined by separate Mueller matrix measurements in a commercial FLC-based visible MME instrument (Horiba Jobin Yvon). The analysis was performed by an implementation of the Lu–Chipman polar decomposition approach [24–26]. The dispersive retardances of each component in the NIR spectral region were determined by a simple crossed polarizer set-up, as no commercial spectroscopic NIR-MME was available. Similarly, the transmittances of the fast and slow axes of the fixed wave-plates and the FLCs were determined by transmission measurements, by orienting the fast or the slow axis of these components with the transmission axis of the polarizers. The details of the measured dispersive retardances and transmission coefficients have been reported elsewhere [17]. For completeness, some of the results are summarized here. The dispersive retardances were modeled by the following dispersion formula:

$$\Delta nd \approx \frac{A_{UV}\lambda}{(\lambda^2 - \lambda_{UV}^2)^{\frac{1}{2}}} - \frac{A_{IR}\lambda}{(\lambda_{IR}^2 - \lambda^2)^{\frac{1}{2}}} \tag{9}$$

where the retardances are given in nm at the wavelength  $\lambda$ . The constants  $A_{UV}$ ,  $A_{IR}$ ,  $\lambda_{UV}$  and  $\lambda_{IR}$  were determined by best fits to the data sets (Table 1).

Table 1. Static properties of polarization components in the order corresponding to Figure 1. The retardance is reported at a single wavelength, i.e. for WP1 then  $\Delta nd = 116.25$  nm at  $\lambda = 465$  nm. The wavelength dependent retardance is calculated from the fitted parameters  $A_{IR}$ ,  $A_{UV}$ ,  $\lambda_{IR}$  and  $\lambda_{UV}$ . All azimuth orientations ( $\theta$ ) of the fast axis of the stable state (denoted by '-'), are given with respect to the polarizers. Positive rotation of the azimuth axis is defined by anticlockwise rotation upon looking into the source [27].

	Retardance	$\theta$ (deg)	$\Delta\theta_{FLC}$	$A_{UV}$	$\lambda_{UV}$ [nm]	$A_{IR}$	$\lambda_{UV}$ [ $\mu$ m]
Polarizer		0					
WP1	$\lambda/4@465$ nm	129.2		110	134	50	11.16
FLC1	$\lambda/2@510$ nm	66.7(-)	44.0	202	280	0	
		110.7(+)					
WP2	$\lambda/2@1008$ nm	164.0		520	134	257	11.16
FLC2	$\lambda/2@1020$ nm	55.5(-)	45.4	505	283	0	
		100.9(+)					
FLC3	$\lambda/2@1020$ nm	55.1(-)	44.2	505	283	0	
		99.3(+)					
WP3	$\lambda/2@1008$ nm	163.1		520	134	257	11.16
FLC4	$\lambda/2@510$ nm	68.5(-)	42.2	202	280	0	
		110.7(+)					
WP4	$\lambda/4@465$ nm	129.4		110	134	50	11.16
Analyzer		0					

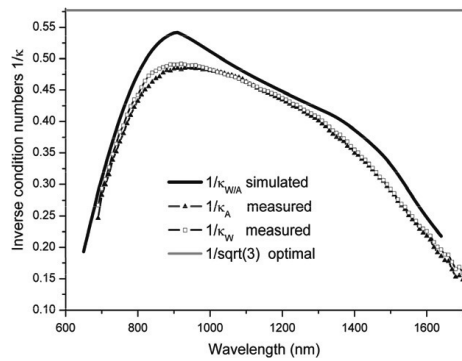


Figure 2. Simulated, measured and optimal inverse condition numbers for the polarization state generator and analyzer, of the FLC-based Mueller matrix system, with the components tabulated in Table 1, and the setup in Figure 1.

The real static dispersive response of the MME may be quantified through the measurement of the condition number of the PSA and the PSG. The simulated response of the MME, using the values in Table 1, can be used to calculate the theoretical condition number. Figure 2 shows both the measured and the simulated condition number of the PSG and the PSA. The system is in good correspondence with the simulations.

#### 4.2. Temporal optical response model for the fast FLC-based MME

The deviation from a step-like temporal response of the recorded intensities in the measured  $\mathbf{B}$  matrix arises

as the system cannot switch immediately from one state to another, and that the photo-detector unit and its preamplifier might have a finite frequency response. Many future real-time applications of a MME could require the temporal characteristics of a certain polarization changing phenomenon. Moving objects, phase transitions, growth of a film or nanostructures, or variable orientation of molecules as in a liquid crystal are mentioned as a few examples.

Consider as an example a linear mechanical rotation of a waveplate (instead of using a FLC) by  $45^\circ$ , and the resulting intensity recorded by the detector as the waveplate is rotating. The switching of a FLC takes time, as the molecules in the LC need to be moved to their new orientations, which causes a nonlinear response of the recorded intensity as a function of the average angle of orientation. Furthermore, it is typical to drive such liquid crystals by an initial voltage spike, in order to enhance the switching frequency. As this involves a collective movement of the molecules making up the liquid crystals, the exact effect of the temporal response of the crystals in terms of its optical properties is uncertain.

To study the limitations in terms of the speed of a FLC-based MME, the formalism in Section 3 (Equations (3)–(7)) was modified to include both the temporal characteristics of the rotating waveplates and the detector response. The results can readily be generalized to other discrete-state MME designs, e.g. one based on electro-optic crystals. The measured temporal response can be compared to simulations, which can increase the understanding of the temporal characteristics of such systems, as will be exemplified below.

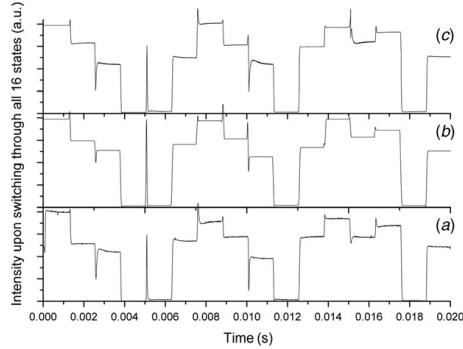


Figure 3. Measured and simulated temporal response of the recorded intensity upon switching through all 16 states of the FLCs: (a) shows the measured intensity upon switching through all 16 states; (b) shows the simulated intensity assuming a linear precession of the molecular director axis; (c) shows the simulated intensity using the time dependent angular rotation from Figure 4. In both simulations the impulse response of the detector is included, and the switching times given by  $t_{\text{up}}$  and  $t_{\text{down}}$  in Table 2 are used.

The generated Stokes vectors were modified in order to allow for the temporal characteristics of the time-dependent angle of orientation between two stable states of the FLC, i.e.  $\hat{\theta}(t)$ , giving

$$\vec{S}_k = \vec{S}(\lambda, \hat{\theta}(t)). \quad (10)$$

By switching the system through the 16 states i.e.  $4 \times 4$  different stable states of the FLCs, the recorded intensities are stored in the wavelength and time dependent, intensity matrix

$$\mathbf{B}(t, \lambda) = \mathbf{A}(t, \lambda)\mathbf{M}(\lambda)\mathbf{W}(t, \lambda).$$

If the temporal response of the sample Mueller matrix  $\mathbf{M}$  is to be determined, it is evidently of utter importance that the time constants involved in the  $\mathbf{A}$  and  $\mathbf{W}$  matrices are much shorter than the ones involved in the sample Mueller matrix.

Figure 3(a) shows the temporal measured intensity response of the NIR-MME system. To keep the signal level high, the 980 nm diode laser source was used in these experiments. The sample was air, modeled as the identity matrix. It is a peculiar intensity response, with overshoots and undershoots before going to the stable states.

The FLCs are nominally reported to switch in 55  $\mu\text{s}$ , and first it was investigated to what extent the overshoots could be due to the detector (and preamplifier) performance. This issue can easily be introduced into the simulations by introducing the impulse response of the preamplifier of the detector

$$\mathbf{B}(t, \lambda) = h(t) \otimes \mathbf{A}(t, \lambda)\mathbf{M}(\lambda)\mathbf{W}(t, \lambda), \quad (11)$$

where  $h(t)$  is the detector impulse response, and  $\otimes$  denotes the convolution. The detector pre-amplifier response was therefore characterized using the frequency modulation option of the diode laser and a lock-in amplifier. The frequency response analysis showed a flat response with an 80 dB/decade fall above 151 kHz. The results were fitted to the transfer function  $H(s) = (1 + sT)^{-4}$ , where the time constant  $T = 1.05 \mu\text{s}/\text{rad}$ , giving the impulse response in the time domain of  $h(t) = t^3(6Te^{t/T})^{-1}$ . Although systematically included in the simulations below, the detector-preamplifier combination is many orders faster than the observed overshoots, and can be neglected in the analysis for Mueller matrix measurement frequencies (i.e. 16 switches) below approximately 2.5 kHz. However, for even faster systems, the detector response will evidently affect the maximal Mueller matrix measurement frequency.

#### 4.2.1. Dynamic response of the FLCs

The FLCs can be regarded as waveplates with nominally two stable states, each separated by a rotation of the waveplate by  $45^\circ$ . In a more accurate model the switching between the stable states is obtained by rotating the molecular director axis of the molecules in the FLC by  $180^\circ$  in a cone around the normal axis of the molecular layer [19]. In order to understand the temporal limitations of the FLC-based MME it is most important to understand the collective dynamic response of the director axis. For simplicity, it is sufficient for our purposes to consider the approximation of crystal switching by assuming a simple rotation of a waveplate from the most stable state 1, to the second excited stable state 2. Let us denote 'up-switching' when switching from the more stable to the excited state ( $\theta_{1,j} \rightarrow \theta_{2,j}$ ), and 'down-switching' when switching from the excited state to the more stable state ( $\theta_{2,j} \rightarrow \theta_{1,j}$ ).

Since no fast Mueller matrix ellipsometer was available to measure the dynamic response of the switching of the crystals, a simple crossed polarizer setup was used. The FLCs were positioned with their fast axis at  $-20^\circ$  with respect to the input polarizer. The measurements were performed at 980 nm, using the flat response InGaAs detector-preamplifier and the intensity was measured as a function of time. The estimated FLC orientation retardance was solved by assuming the constant static retardance using Table 1, with the following equation:

$$I(t) = 1 - \cos^2 2\theta(t) - \cos \delta \sin^2 2\theta(t). \quad (12)$$

Figure 4 shows the dynamic response of the crystals used in this study, using the latter method. The more correct model for the switching is obtained by

precessing the tip of the molecular director in a cone around its axis of rotation. Then  $\chi(t) = 0 \dots \pi$  is related to the azimuth orientation angle by  $\tan \theta(t) = \tan \varphi \cdot \cos \chi(t)$ , with a fixed tilt angle of  $\varphi(t) = \pi/8$ . The latter precessing will also introduce a time-varying retardance. However, this model mainly modifies the centre of the switching curve, which is observed to be inaccurately determined in a crossed polarizer setup (see the discontinuous region around  $22.5^\circ$  in Figure 4). The details of the switching response obtained from Figure 4 are tabulated in Table 2, giving the transition times ( $t_{\text{up}}$  and  $t_{\text{down}}$ ) to the intensity first crossing the level of stable state, for up

and down switching, respectively. The transition times to steady state are given by  $t_{\text{ss-up}}$  and  $t_{\text{ss-down}}$ , for up and down switching, respectively. A detailed inspection of the insets in Figure 4, shows that that the azimuth angle of the crystals appears to pass the stable state before settling, resulting in an overshoot, which typically ranges from  $\Delta\theta = 0.5\text{--}1^\circ$ , corresponding to a precession overshoot of  $d\chi = 12\text{--}18^\circ$ . The switching times are found to vary from crystal to crystal, and the thicker crystals appear to have a 25% longer switching time when going up and a 35% longer switching time when going down, compared with the thinner FLCs.

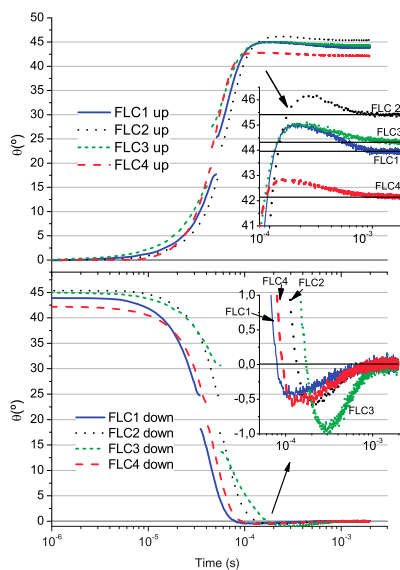


Figure 4. Measured temporal response of the azimuth angle  $\theta(t)$  of the FLCs used in this study. The upper figure shows the up-switching of the crystals (more stable to less stable state), while the bottom figure shows the down-switching (less stable to more stable state). The temporal characteristics, such as  $t_{\text{up}}$  (first crossover with steady state) and  $t_{\text{ss}}$  (time to reach steady state) and the overshoot are tabulated in Table 2. (The color version of this figure is included in the online version of the journal.)

#### 4.2.2. Simulation of the dynamic response of the FLC-based MME

The model for the optical intensities stored in  $\mathbf{B}$  was used to simulate a system that was, as far as possible, similar to the experimental set-up. In the first simulation, the crystals were imagined to switch semi-instantaneously between the states. It was observed that there were no overshoots, and the results were only slightly filtered by the response of the detector.

In a more realistic simulation, the crystals were linearly switched between the two stable states, using the measured up and down switching times tabulated in Table 2. The director axis was modeled to precess linearly in a cone towards the second state, i.e. by letting  $\chi(t) = \pi t / t_{\text{up/down}}$ . The retardance and the azimuth orientation were determined by using the standard Euler rotation of the dielectric tensor, which was assumed uniaxial with the extraordinary axis along the molecular director axis. Figure 3(b) shows the resulting simulated intensity response of the full MME upon switching through all the stable states. It is observed that the large overshoots and undershoots are well reproduced in the simulation, and we conclude that these are simply due to the time-varying intensity illuminating the detector upon changing the Stokes vector as a function of time. A simple linear rotation of the azimuth angle  $\theta(t)$  does not considerably modify the response. The simulated dynamic intensity response using the most advanced model for linear switching between the two states, Figure 3(b), is not fully

Table 2. Temporal switching characteristics of the FLCs used in the fast MME. The up switching and down switching times were used in the simulation in Figure 3.

	$t_{\text{up}}$ ( $\mu\text{s}$ )	$t_{\text{ss-up}}$ ( $\mu\text{s}$ )	Overshoot ( $^\circ$ )	$t_{\text{down}}$ ( $\mu\text{s}$ )	$t_{\text{ss-down}}$ ( $\mu\text{s}$ )	Overshoot ( $^\circ$ )
FLC1 (thin)	113	800	1.00	78	850	0.44
FLC2 (thick)	149	950	0.72	133	1050	0.57
FLC3 (thick)	120	1000	0.54	173	1072	1.00
FLC4 (thin)	91	756	0.68	92	920	0.62

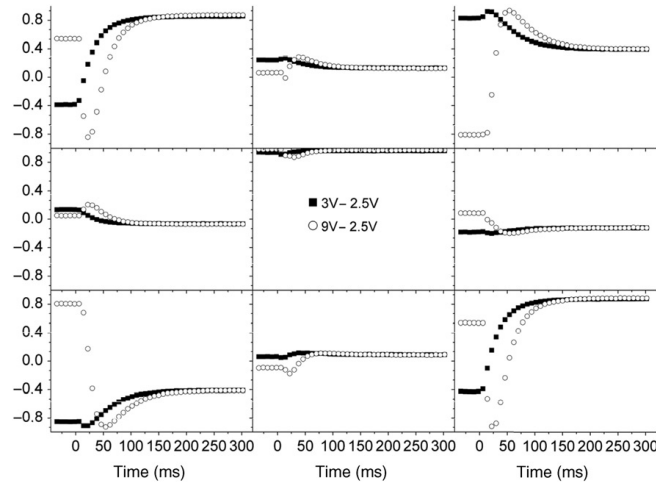


Figure 5. Temporal sub Mueller matrix ( $\hat{m}_R(t)$ ) of a thick VLCR upon switching from  $304^\circ$  to  $25^\circ$  (circle) and  $116^\circ$  to  $25^\circ$  (square). The system was operated at 8 ms per Mueller matrix.

coincident with the measured response shown in Figure 3(a). The crystals clearly have a more complex response of the average azimuth angle, as was already demonstrated by the overshoots in the switching measurements of the FLCs in Figure 4. In the final simulation, the measured switching response of each crystal was therefore carefully introduced into the simulation in an identical manner to the system. The resulting simulated intensity obtained upon switching through the 16 states is shown in Figure 3(c). It is observed that the simulation reproduces the measured response very well, and that the overall system response and its limitations may now be fully understood.

#### 4.3. Application example: dynamic characterization of a thick pneumatic variable liquid crystal retarder

As a demonstration of the operation of the fast FLC based NIR-MME, we have studied the temporal response of the Mueller matrix and the retardance of a thick variable liquid crystal retarder (VLCR), as a function of the switching time, at 980 nm. The full Mueller matrix was measured for each time sample. Since the transition between states occurs very quickly, the system was operated by sampling a Mueller matrix every 8 ms. For visualization purposes the measured Mueller matrix is approximated by

$$\mathbf{M}(t) = \begin{bmatrix} 1 & \vec{0}^T \\ \vec{0} & \hat{m}_R(t) \end{bmatrix},$$

where  $\hat{m}_R(t)$  is the measured time dependent ( $3 \times 3$ ) retardance sub-matrix and  $\vec{0} = [0, 0, 0]^T$  is the null vector. The resulting temporal retardance sub-matrix is shown in Figure 5. Figure 5 shows both  $\hat{m}_R(t)$  observed by switching the VLCR by  $277^\circ$  (9 V to 2.5 V,  $\Delta V = 6.5$  V) and by  $90^\circ$  (3 V to 2.5 V,  $\Delta V = 0.5$  V). The azimuth orientation of the fast axis was  $-50^\circ$ . The VLCR is observed to typically switch to its steady state in approximately 200 ms, independent of  $\Delta V$ . At maximum velocity, the VLCR switches with  $8.6^\circ$  per ms, the under-sampling will thus cause some errors in the measurements. The Lu-Chipman polar decomposition of the matrix gives the temporal evolution of the retardance, which is shown in Figure 6.

#### 5. Summary and conclusion

The dynamic response of a FLC-based Mueller matrix Ellipsometer operating in the near infra-red has been measured and accurately modelled. The dynamic response of the intensity recorded on the detector is a function of the time-dependent collective rotation of the molecular director axis and the impulse response of the detector. The simulations correspond well with the measurements, and it is concluded that using a flat and high-frequency cut-off preamplifier and InGaAs detector does not limit the response, while the dynamic response of the LC molecules rotating towards steady state is the limiting factor for switching speed.

The switching of the crystals from one state to another results in an optical driving signal that may

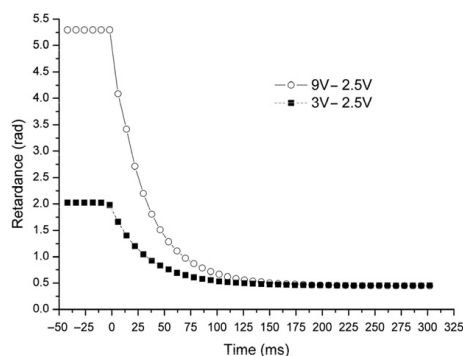


Figure 6. Dynamic response of the retardance (in radians) of a thick VLCR upon switching from 9 V to 2.5 V (circles), and 3V to 2.5 Volts (squares). The MME system was operated at 8 ms per Mueller matrix.

take various forms, and in the worst case has nearly the form of a delta-function. We have shown above, that this is a simple optical phenomenon that may be easily modelled by including a fast linear precession of the director axis of the molecules in the FLCs. Similar issues will be present in any fast operating MME. This response put certain requirements on the detector and preamplifier. However, the detector preamplifier designed for the current setup should be able to handle up to 2.5 kHz repetition rates of Mueller matrix measurements. It is therefore the transient response of the switching of the FLCs that is the critical issue in the FLC-based MME. For accurate measurements, the steady-state response requires a minimum complete Mueller matrix measurement time of 15 ms. A further margin for data acquisition may also be required in order to obtain a good signal-to-noise ratio, resulting in 16 ms as a typical minimum requirement. The system may be operated faster, e.g. by only waiting for the  $t_{\text{up}}$  and  $t_{\text{down}}$ , and allowing the additional measurement errors due to the overshoot. The system may then optimally be operated at a minimum measurement time of 2 ms in addition to acquisition times for each Mueller matrix.

As a demonstration, the system has been successfully used to study the dynamic Mueller matrix during switching of a custom-made thick variable liquid crystal, with a sampling of 8 ms per Mueller matrix.

## References

- [1] Compain, E.; Drevillon, B. *Rev. Sci. Instrum.* **1997**, *68*, 2671–2680.
- [2] Compain, E.; Drevillon, B. *Rev. Sci. Instrum.* **1998**, *69*, 1574–1580.
- [3] Lara, D.; Dainty, C. *Opt. Lett.* **2005**, *30*, 2879–2881.
- [4] Lee, J.; Koh, J.; Collins, R.W. *Rev. Sci. Instrum.* **2001**, *72*, 1742–1754.
- [5] Stabo-Eeg, F.; Kildemo, M.; Nerbo, I.S.; Lindgren, M. *Opt. Eng.* **2008**, *47*, 073604.
- [6] Collins, R.W.; Koh, J.J. *Opt. Soc. Am. A* **1999**, *16*, 1997–2006.
- [7] Garcia-Caurel, E.; De Martino, A.; Drevillon, B. *Thin Solid Films* **2004**, *455-56*, 120–123.
- [8] De Martino, A.; Kim, Y.K.; Garcia-Caurel, E.; Laude, B.; Drevillon, B. *Opt. Lett.* **2003**, *28*, 616–618.
- [9] Dubreuil, M.; Rivet, S.; Le Jeune, B.; Cariou, J. *Opt. Express* **2007**, *15*, 13660–13668.
- [10] Dubreuil, M.; Rivet, S.; Le Jeune, B.; Cariou, J. *Appl. Opt.* **2009**, *48*, 6501–6505.
- [11] Stabo-Eeg, F.; Kildemo, M.; Garcia-Caurel, E.; Lindgren, M. *J. Mod. Opt.* **2008**, *55*, 2203–2214.
- [12] Hallstig, E.; Stigwall, J.; Martin, T.; Sjoqvist, L.; Lindgren, M. *J. Mod. Opt.* **2004**, *51*, 1233–1247.
- [13] Hallstig, E.; Martin, T.; Sjoqvist, L.; Lindgren, M. *J. Opt. Soc. Am. A* **2005**, *22*, 177–184.
- [14] Shirai, T. *Appl. Opt.* **2002**, *41*, 4013–4023.
- [15] Curtis, J.E.; Koss, B.A.; Grier, D.G. *Opt. Commun.* **2002**, *207*, 169–175.
- [16] Gandorfer, A.M. *Opt. Eng.* **1999**, *38*, 1402–1408.
- [17] Ladstein, J.; Kildemo, M.; Svendsen, G.K.; Nerbo, I.S.; Stabo-Eeg, F. *Proc. SPIE* **2007**, *6587*, 65870D.
- [18] Ladstein, J.; Stabo-Eeg, F.; Garcia-Caurel, E.; Kildemo, M. *Phys. Status Solidi C* **2008**, *5*, 1097–1100.
- [19] Gu, C.; Yeh, P. *Optics of Liquid Crystal Displays*; Wiley: New York, 1999.
- [20] Compain, E.; Poirier, S.; Drevillon, B. *Appl. Opt.* **1999**, *38*, 3490–3502.
- [21] Tyo, J.S. *Opt. Lett.* **2000**, *25*, 1198–1200.
- [22] Compain, E.; Drevillon, B. *Appl. Opt.* **1998**, *37*, 5938–5944.
- [23] Compain, E.; Drevillon, B.; Huc, J.; Parey, J.Y.; Bouree, J.E. *Thin Solid Films* **1998**, *313*, 47–52.
- [24] Ossikovski, R.; Anastasiadou, M.; Ben Hatit, S.; Garcia-Caurel, E.; De Martino, A. *Phys. Status Solidi A* **2008**, *205*, 720–727.
- [25] Swami, M.K.; Manhas, S.; Buddhiwant, P.; Ghosh, N.; Uppal, A.; Gupta, P.K. *Opt. Express* **2006**, *14*, 9324–9337.
- [26] Lu, S.Y.; Chipman, R.A. *J. Opt. Soc. Am. A* **1996**, *13*, 1106–1113.
- [27] Hauge, P.S.; Muller, R.H.; Smith, C.G. *Surf. Sci.* **1980**, *96*, 81–107.



L. M. S. Aas, P. G. Ellingsen, and M. Kildemo, “Near infra-red Mueller matrix imaging system and application to retardance imaging of strain,” *Thin Solid Films* **519**, 2737–2741 (2011)

**Paper 4**



# Near infra-red Mueller matrix imaging system and application to retardance imaging of strain

Lars Martin Sandvik Aas, Pål Gunnar Ellingsen, Morten Kildemo

November 8, 2010

## Abstract

We report on the design and performance of a near infra-red Mueller matrix imaging ellipsometer, and apply the instrument to retardance imaging of strain in near infra-red transparent solids. Particularly, we show that the instrument can be used to investigate complex strain domains in multi-crystalline silicon wafers.

## 1 Introduction

In this paper the Near Infra-Red (NIR) Ferroelectric Liquid Crystal (FLC) based Mueller matrix ellipsometer (MME) design reported recently [1], is modified to an imaging set-up, and used to demonstrate the application to retardance imaging of strain. Neither a NIR imaging MME system nor an FLC based imaging MME has to our knowledge been previously reported.

Several non-scanning imaging MME systems based on Variable Liquid Crystal Retarders (VLCR) have recently been reported [2, 3]. These systems have so far only been operated in the visible range, and will generally be many orders slower than an FLC based system [1]. Using such systems, it has been reported that imaging MME is an interesting tool in both bio-applications [3, 4, 5, 6], and strain imaging [7]. Recent non-imaging Mueller matrix ellipsometric studies of bio-tissue demonstrate the usefulness of the Mueller matrix in combination with polar decomposition techniques [8, 9, 10, 11].

The advantage of the complete Mueller matrix measurement relies on the possibility to use polar decomposition techniques [11, 12, 13, 14, 15] and that the Eigenvalue Calibration Method (ECM) may be used for the calibration of the system [16, 17]. Furthermore, the Mueller matrix will not suffer from unexpected properties initially believed not to be part of the sample properties, such as polarization dependent scattering or depolarization, different types of diattenuation, and both circular and linear birefringence components.

Several FLC based designs have been proposed, although the first proposed system similar to the one reported here, appears to be by Gandorfer *et al.* [18]. FLC based MMEs are appealing since they involve no moving parts, and supply a highly stable beam. They are both suitable for direct imaging applications (hyper-spectral and monochrome), or in conjunction with for example stripe CCD spectrographs commonly used in spectroscopy. Furthermore, FLCs modulate rapidly for a fast determination of the Mueller matrix. The disadvantage of liquid crystals, and in particular the current FLCs is the well known degradation upon UV-radiation. Applications of liquid crystal technology in MME are so far limited to the visible and the infra-red.

Reducing material costs is a great concern for the silicon solar cell industry. One approach is to reduce the wafer thickness. A factor making the latter difficult, is the internal residual strain, which is often induced in the process of casting. To control and verify a successful wafer production with lower strain, effective instruments are needed to measure the residual strain. In addition to a report of the system instrumentation, we demonstrate the application of the FLC based NIR MME imaging system to make a map of two dimensional projections of strain fields in multi-crystalline silicon wafers. The strain fields are proportional to the retardance, when neglecting multiple reflections in the sample [24, 25].

## 2 Experimental

### 2.1 Overview of the system and concept

The NIR-MME imaging setup was designed in order to operate both in transmission and reflection mode. The applications demonstrated in this paper are only from transmission mode measurements. The system was designed to operate in the range 700 – 1600nm [1, 19]. A schematic drawing of the setup is shown in Figure 1. In particular, the Polarization State Analyzer (PSA) and the Polarization State Generator (PSG) are both composed of a NIR dichroic polarizer (P1/P2), a zero order quarter wave-plate at 465nm (R1/R4), a half wave-plate at 1020nm (R2/R3), an FLC half wave retarder at 510nm (F1/F4) and an FLC half wave retarder at 1020nm (F2/F3). The FLCs have fixed retardances and can switch between two orientations of the fast axis. A suitable combination of wave-plates and FLCs ensures that the PSG generates four sub-optimal Stokes vectors for all wavelengths in the design range. These four Stokes vectors define the column vectors of the PSG matrix ( $\mathbf{W}$ ). The four analyzer states of the PSA define the rows of the analyzer matrix ( $\mathbf{A}$ ). A Mueller matrix measurement is carried out by measuring the 16 intensities obtained when switching through all possible FLC combinations. The measurement and the calibration process is similar to the one proposed for the LCVR systems [20], and the rotating compen-

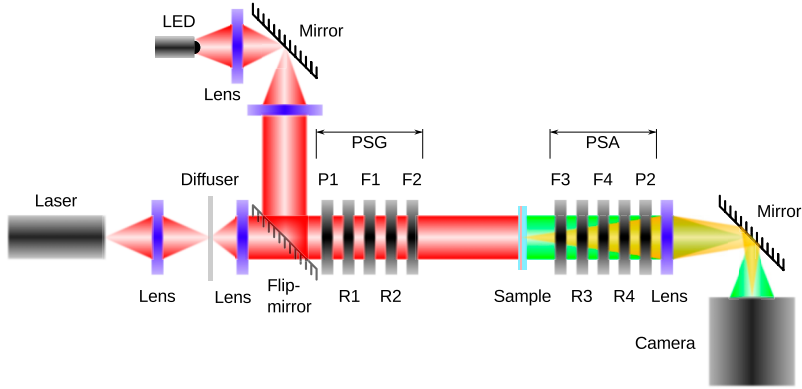


Figure 1: Schematic drawing of the Mueller matrix imaging system. The system consists of two sources, polarization state generator and analyzer, imaging optics and a camera.

sator systems [21]. The 16 measured intensities form a matrix  $\mathbf{B}$ , which correspond to the matrix product of  $\mathbf{A}$ , the sample Mueller matrix ( $\mathbf{M}$ ) and  $\mathbf{W}$

$$\mathbf{B} = \mathbf{WMA}. \quad (1)$$

$\mathbf{M}$  can then be found by multiplying  $\mathbf{B}$  by the inverse of  $\mathbf{W}$  and  $\mathbf{A}$  from each side

$$\mathbf{M} = \mathbf{W}^{-1}\mathbf{B}\mathbf{A}^{-1}. \quad (2)$$

It is evident from linear algebra that for equation 2 to be solvable,  $\mathbf{A}$  and  $\mathbf{W}$  need to be non-singular. Specifically, it has been shown that the error in the intensity measurements ( $\mathbf{B}$ ) and the calibration errors of  $\mathbf{A}$  and  $\mathbf{W}$  are amplified into the errors of a measured Mueller matrix as [21]

$$\frac{\|\Delta\mathbf{M}\|}{\|\mathbf{M}\|} \lesssim \kappa_{\mathbf{A}} \frac{\|\Delta\mathbf{A}\|}{\|\mathbf{A}\|} + \kappa_{\mathbf{W}} \frac{\|\Delta\mathbf{W}\|}{\|\mathbf{W}\|} + \kappa_{\mathbf{W}}\kappa_{\mathbf{A}} \frac{\|\Delta\mathbf{B}\|}{\|\mathbf{B}\|}, \quad (3)$$

where  $\kappa_{\mathbf{W}} = \|\mathbf{W}\|\|\mathbf{W}^{-1}\|$  and  $\kappa_{\mathbf{A}}$  are the matrix condition numbers of  $\mathbf{A}$  and  $\mathbf{W}$ , where we use the  $L_2$  norm which is the ratio of the largest to the smallest singular value [22].

In order to find  $\mathbf{W}$  and  $\mathbf{A}$ , an implementation of the ECM is used. The method allows  $\mathbf{W}$  and  $\mathbf{A}$  to be calculated without exact knowledge of the Mueller matrix of the calibration samples. More details about the FLC MME system and its calibration are reported elsewhere [1, 19].

### 2.1.1 Light sources and detectors

The system is operated with three different light sources. For spectroscopic, and for measurement of weakly scattering samples, a tungsten halogen white light source (150W) is used in combination with a grating monochromator or band pass filters. For samples with more absorption or scattering, higher intensity was needed and a 980nm diode laser (max 300mW) source or a LED array with center wavelength at 1300nm (110mW) was used. In all cases, the light is collimated before entering the PSG. In the case of the diode laser, a rotating diffuser was used to reduce speckle.

The digital camera was a *Xenics Xeva* camera operating at 15Hz, consisting of a 14-bit InGaAs FPA detector with  $640 \times 512$  pixels and sensitive to the spectral band  $0.9 - 1.7\mu\text{m}$ . In addition, due to less thermal noise and dead pixels, a silicon camera from *Hamamatsu* was used in combination with the 980nm laser. The field of view of the system is  $1\text{cm} \times 1\text{cm}$  with a diffraction limited resolution of  $12.5\mu\text{m}$ .

## 2.2 Analysis of the Mueller matrix

The polarimetric information in a measured Mueller matrix can in many cases be extracted using polar decomposition techniques. Several decomposition techniques have been proposed [12, 14, 13]. In particular, the forward polar decomposition technique, described in details elsewhere [8, 10, 11, 12, 14], was applied to all measurements presented here. The basic principle of the forward decomposition is to assume that the polarizing properties of the measured Mueller matrix ( $\mathbf{M}$ ) is taking place in the following order, diattenuation ( $\mathbf{M}_D$ ), retardation ( $\mathbf{M}_R$ ) and depolarization ( $\mathbf{M}_\Delta$ ), which gives

$$\mathbf{M} = \mathbf{M}_\Delta \mathbf{M}_R \mathbf{M}_D. \quad (4)$$

It is further convenient to calculate a numeric quantity for the polarimetric properties, in this paper only the retardance and the orientation of the slow axis are explicitly used.

Due to detector noise, the measured Mueller matrix will always have an error. The error may result in a slightly unphysical Mueller matrix. By putting appropriate physical constraints on the measured matrices, a measure of the matrix physicality can be found. It is further possible to calculate the closest physical matrix of an unphysical matrix. In particular, the constraints proposed by Cloude [23] was applied in this work.

### 3 System performance, results and discussion

#### 3.1 Validation of calibration of the NIR MME Imaging System

For an image the average inverse condition number of  $\mathbf{A}$  and  $\mathbf{W}$  is 0.46.

An estimate of the accuracy of the Mueller matrix imaging system can be made by considering a measurement of the well defined Mueller matrix of air (the identity matrix). The mean matrix of a measured Mueller matrix image was

$$\begin{bmatrix} 1.000 \pm 0.00 & -0.004 \pm 0.01 & -0.003 \pm 0.01 & 0.006 \pm 0.01 \\ 0.000 \pm 0.01 & 1.002 \pm 0.02 & -0.001 \pm 0.02 & -0.002 \pm 0.02 \\ 0.001 \pm 0.01 & -0.002 \pm 0.02 & 1.006 \pm 0.03 & -0.003 \pm 0.02 \\ 0.001 \pm 0.01 & 0.002 \pm 0.02 & 0.007 \pm 0.02 & 0.998 \pm 0.03 \end{bmatrix},$$

with the standard deviation from the mean value given as the  $\pm$ . The error in the mean matrix is in the third decimal, while the standard deviation from the mean is in the second. The variations found over the pixels may have many sources, but is most likely due to detector noise. The mean noise (fidelity) found from Cloude filtering is  $-23.7\text{dB}$  with standard deviation of  $0.8\text{dB}$ . The non-uniformity and error is found to be satisfactory, although there is room for further improvements.

#### 3.2 Polarimetric images and Strain mapping

Polarimetric imaging can be used to investigate strain fields in transparent crystals. An isotropic material which experiences a non-isotropic stress, becomes, as described by the photoelastic theory [24, 25], anisotropic (birefringent) due to the induced internal strain. Polarimetry is very sensitive to changes in the retardance

$$\delta = \Delta n \cdot d = (n_{\text{slow}} - n_{\text{fast}}) \cdot d, \quad (5)$$

which is proportional to the birefringence (difference in refractive index from slow to fast axis,  $\Delta n$ ) and the thickness of the sample ( $d$ ). The refractive index will increase in the direction of the positive strain (compression). Hence the direction of the slow axis will give the direction of the positive strain. The retardance will be a projection of the strain in real space to the  $xy$ -image plane. A quantitative calculation of the strain using the photoelastic properties and known crystal orientation [24, 25], is out of the scope of the current proof of concept report.

##### 3.2.1 Retardance imaging of strain in stressed $\text{CaF}_2$

The capability of the MME system to image strain patterns was investigated by inducing a direct force onto a crystalline  $\text{CaF}_2$  prism, which is isotropic

and transparent from the UV to the infrared. The prism was placed on a platform in the image plane of the system, and stress was applied through a metal plug. The upper edge of the prism was opaque, such that the interface region between the metal plug and the crystal could not be examined.

Figure 2 shows Mueller matrix images of the prism without and with applied stress. It is evident from the non stressed image that the crystal is isotropic, and has no retardance or diattenuation. After the stress is applied, the crystal becomes anisotropic, seen by the appearance of the non diagonal lower right  $3 \times 3$  matrix. From the measured Mueller matrix, the magnitude of the retardance and the orientation of the slow axis is then calculated.

The corresponding retardance plots for the two Mueller matrix images in Figure 2 are shown in Figure 3. It is evident that when no stress is applied, there is no slow axis, and the calculated direction is therefore random, as a result of noise. When stress is applied, the direction of the slow axis corresponds to the direction of the positive strain.

Evidently, this sample could have been studied with any visual MME imaging system. However, in case of more rough surfaces or a low band-gap crystal, the use of near infra-red light becomes imminent.

### 3.2.2 Retardance imaging of strain in a multi-crystalline silicon wafer

The band-gap of Si makes the material transparent for photons with lower energy than 1.1eV, which means that a visible MME can not perform bulk strain measurements in transmission.

In this experiment the sample was initially a  $150\mu\text{m}$  thick multi-crystalline wafer, with a surface of about  $4\text{cm} \times 2.5\text{cm}$  and a trapezoidal shape (see Figure 4). Crystalline silicon is isotropic with a cubic lattice structure. In multi-crystalline wafers the grains are through-going and the grain boundaries go straight through the wafer, eliminating the problem of shading grains. In order to avoid large losses of intensity and to obtain a good signal to noise ratio, the wafer was polished on both sides, down to a thickness of approximately  $100\mu\text{m}$ . The wafer was placed in an assembly consisting of two bars with slits, keeping the wafer vertically stable and in position (see Figure 4). Stress was then applied to the wafer by buckling [26], which is a well known method for material strength tests. The strain is induced when the bars are forced towards each other such that the wafer bends by the control of a fine threaded screw.

In order to map the whole wafer, the assembly is mounted on a translation stage which automatically moves to the next position after each Mueller matrix image acquisition. For simplicity and proof of concept, only one of the images is considered here, the location of this area on the wafer is indicated by the red square in Figure 4.

Figure 5 shows the calculated retardance and the orientation of the slow



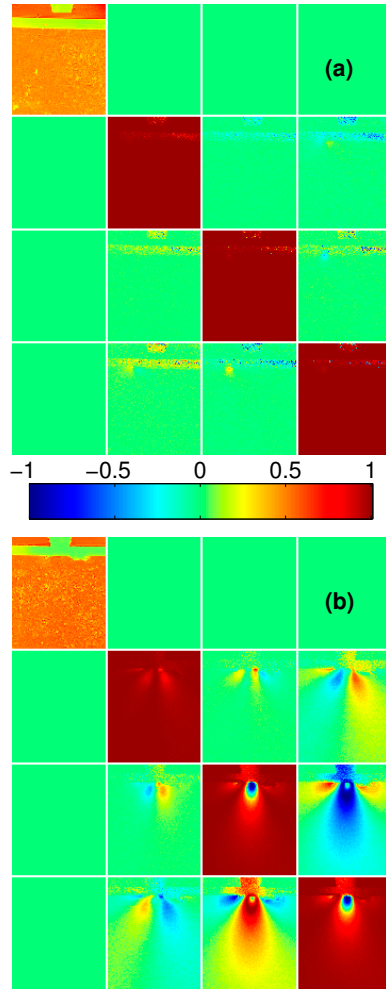


Figure 2: Mueller matrix images of non stressed (a) and stressed (b) calcium fluoride crystal. The elements are normalized to  $m_{1,1}$ , except from the  $m_{1,1}$  image which shows the transmission intensity image. In (a) the crystal is found isotropic, *i.e.* No strain induced birefringence is observed in the crystal, while in (b) the crystal is found with a graded anisotropy due to the non uniform applied stress.

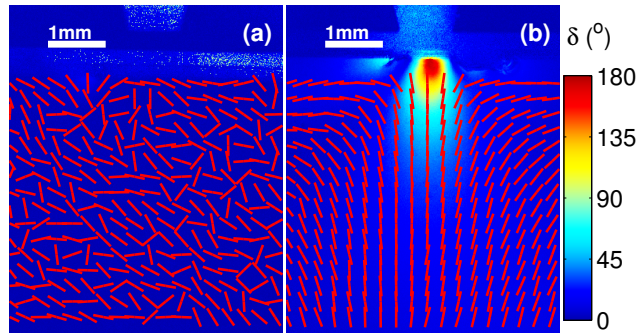


Figure 3: Calculated retardance from the Mueller matrix image in Figure 2. (a) shows the retardance map when no stress is applied, and (b) when stress is applied. The lines show the direction of the slow axis, while the color-map indicates the retardance in degrees with wavelength of 980nm.

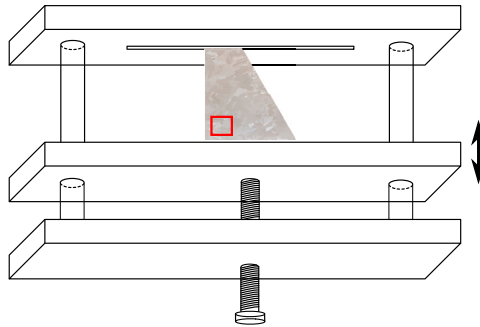


Figure 4: The assembly made for the buckling of the wafer. The wafer is placed between a fixed and a non fixed bracket, which then can be translated by a fine threaded screw.

axis of the selected area of the strained wafer. The crystal grains show contrast in both the orientation of slow axis and the retardance maps, which indicates that both different magnitude and orientation of strain can be found. The two areas (1 and 2) indicated by the red squares in Figure 5(a) are enlarged and shown in Figure 6 and 7.

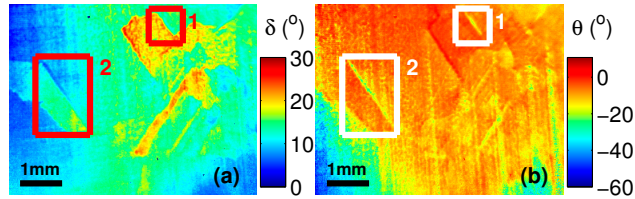


Figure 5: Figure (a) shows the calculated retardance map of the area indicated by the red square in Figure 4, with applied strain, while Figure (b) shows the orientations of the slow axes for the area in interest. Areas 1 and 2 indicate the two areas that are described in more detail within the text.

The retardance image of area 1 (Figure 6) shows a grain boundary where the retardance is higher for the grain located in the lower part of the image, compared to the upper grain. Various domains of lower and higher retardance can also be observed inside the two grains. Figure 6(a) shows that at the grain boundary there appears to be domains with lower retardance than the surrounding grains. It is observed from Figure 6(b), that the orientation of the strain is very different in this particular domain. These observations may possibly be due to a relaxation of strain at the grain boundary.

In area 2 (Figure 7) the grain is observed to have a higher retardance than the adjacent grains. One may expect that the whole grain experienced the same retardance, but in this case a higher retardance is found in the lower part of the grain. This observation can possibly be explained by the low retardance on the grain boundary around the upper part of the grain, where a relaxation may have occurred. The corresponding orientation of the slow axis (Figure 7(b)) shows a different strain orientation than the surrounding grains. The details of the structures within the domains can without great difficulty be studied in a lab set-up. A production line equipment can be envisaged in order to inspect strain over large areas, or strain above a particular threshold level. Polarimetric imaging may also be useful in several other occasions *e.g.* to characterize the polarization dependent optical properties of optical components, such as lenses, wherever these have to be taken into account.

Surface roughness and multiple reflections and its effect on the measured retardance and depolarization are important effects and will together with

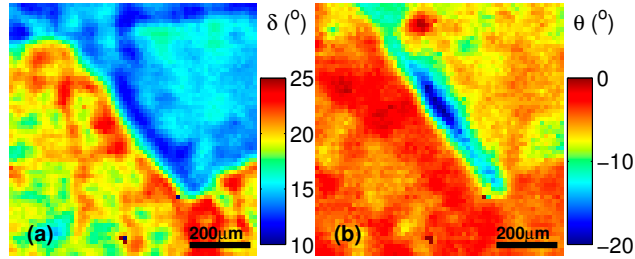


Figure 6: Figure (a) shows the calculated retardance map of area 1, with applied strain. There is good contrast at the grain boundary, also interesting is the low retardance domain along the grain boundary, which may be induced due to a relaxation of strain at the boundary. Figure (b) shows the calculated orientation of the slow axis.

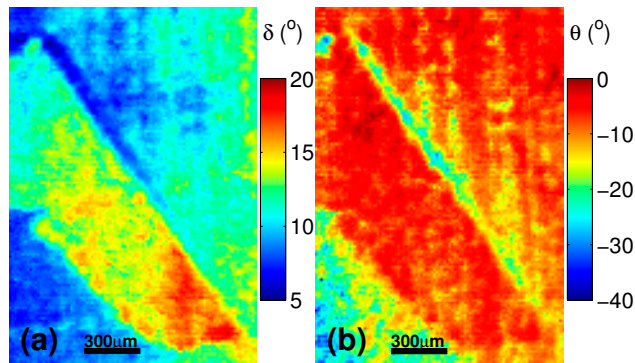


Figure 7: Figure (a) shows the calculated retardance map of area 2, with applied strain. Figure (b) shows the corresponding orientation of slow axis. In this area of the wafer we also see that there is a domain along the grain boundary where the retardance is lower than in the two adjacent grains. Also the slow axis has a different orientation in this domain.

quantitative analysis of strain be addressed in future work.

## 4 Conclusions

In conclusion, we have constructed a near infra-red (NIR) Mueller matrix imaging ellipsometer based on ferroelectric liquid crystal retarders. The system has been demonstrated to be a valuable tool in the characterization of strain in NIR transparent solids, and in particular multi-crystalline silicon. Through the use of Mueller matrix analysis tools, a detailed analysis of strain field domains can be made, which in the future can be quantified and used as input to numerical models.

### 4.1 Acknowledgements

The authors acknowledge Håkon Ottar Nordhagen and Stéphane Dumoulin from the Department of Applied Mechanics and Corrosion at SINTEF for collaboration and useful discussions on strain in multi-crystalline silicon.

The authors are also grateful to Hallvard Skjerpig, Frantz Stabo-Eeg, Ingar Stian Nerbø and Mikael Lindgren for help and discussions on the MME imaging system.

The work was performed within “The Norwegian Research Centre for Solar Cell Technology” project number 193829), a Centre for Environment-friendly Energy Research co-sponsored by the Norwegian Research Council and research and industry partners in Norway.

## References

- [1] Lars Martin Sandvik Aas, Paal Gunnar Ellingsen, Morten Kildemo, and Mikael Lindgren. Dynamic Response of a fast near infra-red Mueller matrix ellipsometer. *Journal of Modern Optics*, 57(17):(page range not confirmed) 2010.
- [2] Blandine Laude-Boulesteix, Antonello De Martino, Bernard Drévilion, and Laurent Schwartz. Mueller polarimetric imaging system with liquid crystals. *Applied optics*, 43(14):2824–32, May 2004.
- [3] JM Bueno and P Artal. Double-pass imaging polarimetry in the human eye. *Optics letters*, 24(1):64–66, 1999.
- [4] J.R. Chung, J.S. Baba, A.H. DeLaughter, and G.L. Cote. Development and use of a novel automated Mueller matrix polarization imaging system for in-vivo imaging of lesions. In *Proceedings of SPIE*, volume 4613, pages 111–117, 2002.

- [5] AM Baldwin, JR Chung, JS Baba, CH Spiegelman, and MS. Mueller matrix imaging for cancer detection. *25th Proceedings of IEEE*, pages 1027–1030, 2003.
- [6] D. Lara-Saucedo and C. Dainty. Depth Resolved Polarization Sensitive Imaging of the Eye using a Confocal Mueller Matrix Ellipsometer-Proof of Principle. *Investigative Ophthalmology and Visual Science*, 44(5):3627, 2003.
- [7] Michael Richert, Xavier Orlik, and Antonello De Martino. Adapted polarization state contrast image. *Optics express*, 17(16):14199–210, August 2009.
- [8] Nirmalya Ghosh, Michael F G Wood, and I Alex Vitkin. Mueller matrix decomposition for extraction of individual polarization parameters from complex turbid media exhibiting multiple scattering, optical activity, and linear birefringence. *Journal of biomedical optics*, 13(4):044036, 2010.
- [9] MK Swami, S. Manhas, P. Buddhiwant, N. Ghosh, A. Uppal, and PK Gupta. Polar decomposition of 3 x 3 Mueller matrix: a tool for quantitative tissue polarimetry. *Opt. Express*, 14:9324–9337, 2006.
- [10] S Manhas, MK Swami, P Buddhiwant, N Ghosh, PK Gupta, and K. Singh. Mueller matrix approach for determination of optical rotation in chiral turbid media in backscattering geometry. *Opt. Express*, 14:190–202, 2006.
- [11] Nirmalya Ghosh, Michael F G Wood, Shu-hong Li, Richard D Weisel, Brian C Wilson, Ren-Ke Li, and I Alex Vitkin. Mueller matrix decomposition for polarized light assessment of biological tissues. *Journal of biophotonics*, 2(3):145–56, March 2009.
- [12] S.Y. Lu and R.A. Chipman. Interpretation of Mueller matrices based on polar decomposition. *Journal of the Optical Society of America A*, 13(5):1106–1113, 1996.
- [13] Razvigor Ossikovski. Analysis of depolarizing Mueller matrices through a symmetric decomposition. *Journal of the Optical Society of America. A, Optics, image science, and vision*, 26(5):1109–18, May 2009.
- [14] R Ossikovski, A. De Martino, and S Guyot. Forward and reverse product decompositions of depolarizing Mueller matrices. *Optics letters*, 32(6):689–691, 2007.
- [15] R Ossikovski, M Anastasiadou, S.B. Hatit, E. Garcia-Caurel, and A. De Martino. Depolarizing Mueller matrices: how to decompose them? *Physica Status Solidi (A)*, 205(4):720–727, 2008.

- [16] E Compain, S Poirier, and B Drevillon. General and self-consistent method for the calibration of polarization modulators, polarimeters, and mueller-matrix ellipsometers. *Applied optics*, 38(16):3490–502, June 1999.
- [17] E Garcia-Caurel. Spectroscopic Mueller polarimeter based on liquid crystal devices. *Thin Solid Films*, 455-456:120–123, 2004.
- [18] A M Gandorfer. Ferroelectric retarders as an alternative to piezoelectric modulators for use in solar Stokes vector polarimetry. *Opt. Eng.*, 38(8):1402–1408, 1999.
- [19] TS Narasimhamurty. *Photoelastic and electro-optic properties of crystals*. Plenum Press, New York :, 1981.
- [20] DF Nelson and M Lax. Theory of the photoelastic interaction. *Physical Review B*, 3(8):2778–2794, 1971.
- [21] J. Ladstein, F. Stabo-Eeg, E. Garcia-Caurel, and M. Kildemo. Fast near-infra-red spectroscopic Mueller matrix ellipsometer based on ferroelectric liquid crystal retarders. *physica status solidi (c)*, 5(5):1097–1100, May 2008.
- [22] JM Bueno. Polarimetry using liquid-crystal variable retarders: theory and calibration. *Journal of Optics A: Pure and Applied Optics*, 2(3):216–222, 2000.
- [23] F. Stabo-Eeg, M Kildemo, I.S. Nerbø, and M Lindgren. Well-conditioned multiple laser Mueller matrix ellipsometer. *Optical Engineering*, 47:073604, 2008.
- [24] J.S. Tyo. Noise equalization in Stokes parameter images obtained by use of variable-retardance polarimeters. *Optics letters*, 25(16):1198–200, 2000.
- [25] S.R. Cloude. Conditions for the physical realisability of matrix operators in polarimetry. In *Proc Soc Photo Opt Instrum Eng*, volume 1166, pages 177–185, 1989.
- [26] Don Orr Brush. *Buckling of bars, plates and shells*. McGraw-Hill, 1975.





P. G. Ellingsen, M. B. Lilledahl, L. M. S. Aas, C. D. L. Davies, and M. Kildemo, “Quantitative characterization of articular cartilage using Mueller matrix imaging and multiphoton microscopy,” *J. Biomed. Opt.* **16**, 116002 (2011)

## Paper 5



# Quantitative characterization of articular cartilage using Mueller matrix imaging and multiphoton microscopy

Pål Gunnar Ellingsen, Magnus Borstad Lilledahl, Lars Martin Sandvik Aas, Catharina de Lange Davies, and Morten Kildemo  
Norwegian University of Science and Technology, Department of Physics, Faculty of Natural Sciences and Technology,  
Institutt for Fysikk, 7491 Trondheim, Norway

**Abstract.** The collagen meshwork in articular cartilage of chicken knee is characterized using Mueller matrix imaging and multiphoton microscopy. Direction and degree of dispersion of the collagen fibers in the superficial layer are found using a Fourier transform image-analysis technique of the second-harmonic generated image. Mueller matrix images are used to acquire structural data from the intermediate layer of articular cartilage where the collagen fibers are too small to be resolved by optical microscopy, providing a powerful multimodal measurement technique. Furthermore, we show that Mueller matrix imaging provides more information about the tissue compared to standard polarization microscopy. The combination of these techniques can find use in improved diagnosis of diseases in articular cartilage, improved histopathology, and additional information for accurate biomechanical modeling of cartilage. © 2011 Society of Photo-Optical Instrumentation Engineers (SPIE). [DOI: 10.1117/1.3643721]

Keywords: Mueller matrix imaging; multiphoton microscopy; collagen; cartilage.

Paper 11303R received Jan. 15, 2011; revised manuscript received Aug. 18, 2011; accepted for publication Sep. 6, 2011; published online Oct. 26, 2011.

## 1 Introduction

Articular cartilage covers and protects the bones in joints, and its integrity is essential for normal function. It imparts two important properties to a joint. First, it provides a low-friction surface for smooth articulation of the joint; second, it provides a cushioning layer to distribute loads and protect the underlying bone. The structure of articular cartilage is typically divided into three distinct morphological zones: (i) The superficial layer with a dense collagen network and the collagen fibers oriented primarily tangential to the articulating surface, (ii) the intermediate layer, where the fibers are more randomly distributed, and (iii) the radial layer, where the fibers are oriented perpendicular to the bone surface. The collagen fibers are cross-linked with proteoglycans in a fluid-saturated gel of glycosaminoglycans and proteoglycans. Scattered throughout the cartilage are chondrocytes that reside in lacunae and are responsible for the formation of new cartilage.<sup>1</sup>

Osteoarthritis is a disease in articular cartilage symptomized by pain and reduced joint function, affected by a variety of factors (genetic, traumatic, age, excessive loading).<sup>2</sup> It is the leading cause of disability in the U.S. and will likely see an increased incidence in the future due to an aging and more obese population.<sup>3</sup> Osteoarthritis is characterized by structural changes in the cartilage, accompanied by a loss of proper function. The loss of function will lead to changed loading conditions in the knee and, therefore, further changes in the microscopic structure. In order to predict the outcome of this biological cascade, it is necessary to have methods to characterize the current tissue structure. Osteoarthritis is usually diagnosed based on clinical findings, sometimes with the addition of radiographic

imaging. However, in a significant fraction of symptomatic patients, no radiographic changes are found.<sup>4</sup> Magnetic resonance imaging may be used for further stratification, but the association between clinical symptoms and findings from images is not always strong.<sup>5</sup> Therefore, a more detailed investigation using novel imaging techniques, is necessary to enhance diagnosis.

Bright-field light microscopy of haematoxylin-eosin-stained sections is the standard method to assess the microscopic structure of cartilage, even though it is not possible to see the structure of the collagen network. Polarization microscopy is sometimes used but can only provide qualitative information on the direction of collagen fibers due to the complex nature of the polarization properties of tissue. Novel methods to study the microscopic structure of cartilage will provide more details on the current pathological status and perhaps differentiate between conditions that cannot be distinguished with standard techniques.

Multiphoton microscopy (MPM) is a nonlinear optical process used to acquire images of biological specimens.<sup>6</sup> Because of the nonlinearity of the signals, the technique is intrinsically confocal (no need for confocal optics), and many biological molecules exhibit specific intrinsic nonlinear signatures such that no staining is required. The second-harmonic generation (SHG) signal can be used to image the collagen type II fibers present in cartilage.<sup>7,8</sup> *In vivo* imaging is possible and yields high-resolution, three dimensional images.<sup>9</sup> *In vivo* MPM would be a valuable complementary technique to standard arthroscopy. Methods have been developed to generate quantitative measures of the structure of the collagen fabric<sup>10</sup> and its optical properties.<sup>11</sup> The drawback of MPM is that high-resolution imaging of macroscopic volumes is time consuming. Furthermore, in the intermediate and radial layers, the collagen fibers are below the resolution limit of optical microscopy, such that individual fibers cannot be resolved.

Address all correspondence to: Morten Kildemo, Norwegian University of Science and Technology, Department of Physics, Faculty of Natural Sciences and Technology, 7491 Trondheim, Norway; Tel: +0047 73593211; E-mail: morten.kildemo@ntnu.no.

Mueller matrix imaging (MMI) provides a complementary technique to MPM and extracts the full Mueller matrix for every pixel in the image of a sample.<sup>12</sup> Because the resolution is adjustable (but usually worse than MPM by a factor of around 10), and camera-based imaging is used instead of point scanning, larger areas are scanned faster compared to MPM. Because MMI also is an optical technique, it cannot resolve the small collagen fibers in the middle layer. However, the advantage of MMI is that it is based on the rich polarization information contained in the full Mueller matrix, such that the directionality of the fibers may be derived, as well as the optical rotation and depolarization of the sample, by using forward polar decomposition.<sup>13,14</sup> The use of decomposed Mueller matrix measurements to characterize tissue phantoms and biological samples has been described,<sup>15,16</sup> but to our knowledge never on samples of cartilage. Compared to other polarimetric imaging systems that only measure some of the components of the Mueller matrix<sup>17–19</sup> and require significant prior knowledge of the sample and the desired measurements, the Mueller matrix imaging system is much more flexible, enabling the characterization of more complex and unexplored samples with the possibility to fully characterize the polarization properties of the sample. Here, we show that the combination of MPM and MMI provide more detailed information about the articular cartilage structure compared to conventional methods and potentially a better understanding of the progression of osteoarthritis.

## 2 Materials and Methods

### 2.1 Materials

The medial femoral condyle of chicken cartilage ( $n = 2$ ) was cut in 100- $\mu\text{m}$ -thick sections to a depth of 2 mm using a vibratome (Leica VT-1000). After sectioning, the samples were transferred to microscope slides and a cover glass placed on top. The edges were sealed with Vaseline to avoid dehydration. Sections were cut in the transversal plane. The sections were kept at 4°C between measurements.

### 2.2 Multiphoton Microscopy

The MPM images were acquired using a commercial system (Zeiss LSM 510), equipped with a Ti:sapphire laser pumped by a 5-W solid state laser (Coherent Mira and Verdi, respectively). The Ti:sapphire laser was tuned to 800 nm for excitation of the SHG signal. A dichroic short-pass filter at 650 nm was used to collect the backscattered light. A second dichroic at 475 nm and a bandpass filter at 390–425 nm were used to separate the SHG from the fluorescence. All images were acquired in the epi configuration.

Images were acquired with a 10 $\times$ , 0.6 numerical aperture (NA) objective. For samples larger than the field of view, several images were juxtaposed automatically using the microscopy control system. Images were acquired at four to eight different depths, with an interval of 10  $\mu\text{m}$ , depending on the quality of the signal in the deeper sections.

On the basis of an image-analysis algorithm described in detail elsewhere,<sup>10</sup> we derived the primary direction and anisotropy of the fibers at every pixel in the image. Briefly, the algorithm calculates the two-dimensional discrete Fourier transform of a small subframe around a given pixel. Typically, the strongest Fourier components will tend to lie on a line perpendicular to

the fibers in the image. The direction of this line was found by minimizing the sum of angles, weighted by the Fourier power spectrum relative to this line. The anisotropy is extracted as a measure of how close the strongest frequency components are clustered around this line.

### 2.3 Mueller Matrix Imaging

The near-infrared Mueller matrix imaging (NIR MMI) system used here is described in greater detail elsewhere.<sup>12</sup> Note that the light source used here is the 980-nm laser diode and that the numerical aperture of the system is 0.04. It uses two ferroelectric liquid crystals (FLCs) together with a polarizer and two wave plates to generate four orthogonal Stokes vectors in what is known as a polarization-state generator (PSG), which then are used to probe the sample. After passing through the sample, the resulting polarization-state is analyzed by a polarization state analyzer (PSA), consisting of the same components as the PSG, in reverse order. Sixteen intensity images are acquired using different settings of the PSG and PSA. The Mueller matrix  $\mathbf{M}$  is then calculated from the configurations of the PSG and PSA using the eigenvalue calibration method.<sup>20</sup> Repeating this for every pixel in the images results in a Mueller matrix image,  $\mathbf{M}_{\text{im}}$ . The Mueller matrix is normalized, meaning that all of the elements in the matrix is divided by the  $M_{11}$  element.

The measured  $\mathbf{M}$  is decomposed into depolarization, ( $\mathbf{M}_{\Delta}$ ), retardation, ( $\mathbf{M}_{\text{R}}$ ), and diattenuation, ( $\mathbf{M}_{\text{D}}$ ), matrices using forward polar decomposition,  $\mathbf{M} = \mathbf{M}_{\Delta}\mathbf{M}_{\text{R}}\mathbf{M}_{\text{D}}$ , first described by Lu and Chipman<sup>13</sup> and applied by Manhas et al.<sup>14</sup> to tissue characterization.

From  $\mathbf{M}_{\text{R}}$ , it is further possible to find the linear retardance, direction of the slow axis (perpendicular to the fast axis), and the optical rotation (see Manhas et al.<sup>14</sup>). We assume that the collagen fibers can be modeled using the Bruggeman effective medium theory,<sup>21</sup> and thus assign the slow optical axis to the long axis of the fibers.

## 3 Results

### 3.1 Multiphoton Microscopy

SHG images of the superficial layer show a distinct collagen structure, which is illustrated in Fig. 1(a). By employing the direction analysis method described in Sec. 2.2, we derived the primary direction and degree of anisotropy of the fibers, which is shown in Figure 1(b). The direction is coded according to color using the provided legend and the anisotropy is mapped to the intensity of the color. Figure 2(a) shows a sample where both the superficial and intermediate layers can be seen. The center region, which belongs to the superficial zone, exhibits clear fibrillar structure, whereas in the intermediate layer, shown in the lower right part of Fig. 2(a), no collagen fibers can be discerned. Only the lacunae can be seen as dark voids, embedded in a smooth SHG signal. Figure 2(b) shows that the analysis picks up the direction in the superficial region but that in the intermediate layer where no structure can be discerned, the anisotropy is very low, corresponding to low intensity in the color image.

### 3.2 Mueller Matrix Imaging

MMI images were acquired from the same samples as imaged with MPM. The MMI images were first Cloude filtered<sup>22</sup> and

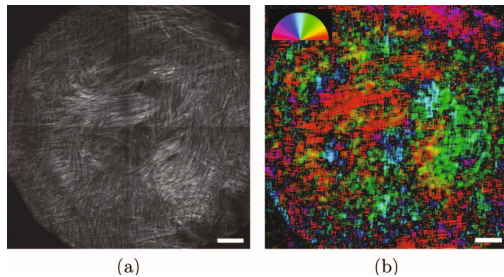


**Fig. 1** (a) SHG intensity image of a transverse section of cartilage in the superficial layer ( $100\ \mu\text{m}$  below the surface), where the collagen fibers are clearly visible. This image is the result of four images tiled together. (b) Result of the directional analysis. The calculated direction of the fibers is color coded according to the semicircle legend. The intensity of the color has been scaled to the calculated anisotropy value. Scale bar is  $200\ \mu\text{m}$ .

then decomposed using the forward polar decomposition described in Sec. 2.3. An example of the full Mueller matrix for a cartilage sample is illustrated in Fig. 3. The  $M_{11}$  element has been substituted by the intensity image, because this element would be equal to 1 as a result of the normalization. The values of the diattenuation matrix  $\mathbf{M}_D$  were found to be very small and are not included here.

After the decomposition, the direction of the slow axis is found from the retardance matrix  $\mathbf{M}_R$ .<sup>14</sup> The corresponding image of the directions is illustrated in Fig. 4. Because the long axis of the collagen fibers corresponds to the optical slow axis, the directional image shows the collagen fiber direction and can be compared to the MPM image of the same sample, as shown in Fig. 5.

The forward polar decomposition enables in addition to the direction of the slow axis, the calculation of the amount of double refraction in the sample known as the linear retardance (which is seen in Fig. 6), the amount of left or right circular polarization induced by the sample, known as the optical rotation (shown in Fig. 7), and the depolarization index (as seen in Fig. 8). The

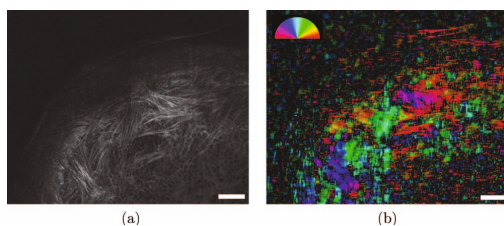


**Fig. 2** (a) SHG intensity image of a transverse section of cartilage from slightly below the superficial layer ( $500\ \mu\text{m}$  below the surface). The central part of the image belongs to the superficial region, and here, the fibers are clearly visible. The lower right part belongs to the intermediate layer. No clear structure of fibers can be seen in this region, only the lacunae are distinguishable as dark voids. (b) Result of directional analysis. The calculated direction of the fibers is color coded according to the semicircle legend. The intensity of the color has been scaled by the calculated anisotropy value. In the intermediate layer, only a weak random direction is picked up. Scale bar is  $200\ \mu\text{m}$ .

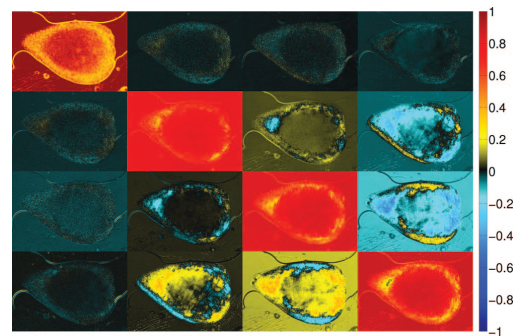


**Fig. 3** Full Cloude-filtered Mueller matrix image for a sample of cartilage, from a transversal section at a depth of  $500\ \mu\text{m}$ , with the intensity image overlaid the  $M_{11}$  element. The central dark area in  $M_{11}$  is the intermediate layer, and the surrounding bright area is the superficial layer.

depolarization index shows how much of the incoming polarized light is converted into partially polarized light.

The intermediate zone of the cartilage (center of Figs. 4 and 6) exhibits more variation and features in the MMI images compared to what can be seen in the MPM images. In this intermediate zone, the direction and retardance images show regions with differing structure.

#### 4 Discussion

The Mueller matrix was decomposed into three polarization properties of which only the retardation and depolarization were used directly in this study. The retardance (circular, linear, and direction of fast axis) will, in terms of effective medium theory, yield results from features smaller than the resolution in the image. The latter property is useful, because it can be used to characterize collagen fibers from the intermediate and radial zone of the cartilage, where the collagen fibrils are below the resolution limit of MPM.

Because the collagen fibers have a higher refractive index than the surrounding medium,<sup>23</sup> they will have the slow axis

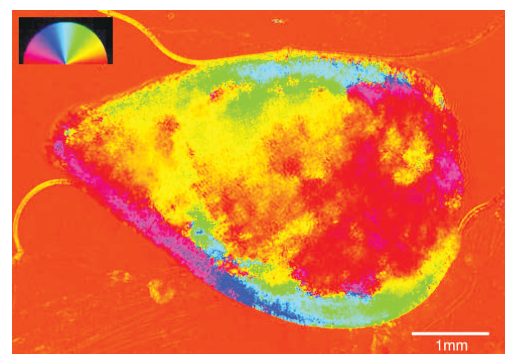


**Fig. 4** Visualization of the direction of the slow axis found from  $\mathbf{M}_R$ .

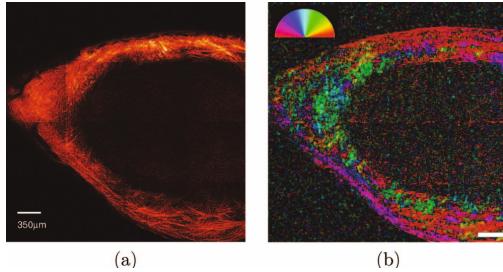


**Fig. 5** (a) SHG images from the same area as the MMI images and (b) calculated directions of image in (a).

along the long axis. The difference in the refractive index of the slow and fast axes can be calculated using the simple linear dispersion relation for a birefringent medium

$$\Delta n = \frac{\lambda \delta}{2\pi L},$$

where  $\lambda$  is the wavelength (here, 980 nm),  $\delta$  the linear retardance (in radians), and  $L$  the thickness of the sample (here, 100  $\mu\text{m}$ ). Using a representative value of  $\delta = 50$  deg for the edges of the sample, as seen in Fig. 6, and  $\delta = 15$  deg for the intermediate region, results in an apparent birefringence  $\Delta n = 1.4 \times 10^{-3}$  for the edges, similar to previously reported values,<sup>24</sup> and  $\Delta n = 0.4 \times 10^{-3}$  from intermediate regions. As Fig 6 shows, there are large differences in the linear retardance across the sample, resulting in large differences in  $\Delta n$ , such that care should be taken when reporting birefringence measurements of collagen in turbid media.

The slow axis found from the decomposed Mueller matrix is the projection of the three-dimensional slow axis into the imaging plane. In addition, since directions found from the Mueller matrix measurement are from a volume, the directions seen in Fig. 4, will be an average of the collagen fibers through the sample as opposed to the MPM images, which are acquired at a certain depth (Fig. 5). Even when taking the latter into consideration, the directions in the sample correspond well to the direction in the corresponding MPM image, indicating that the

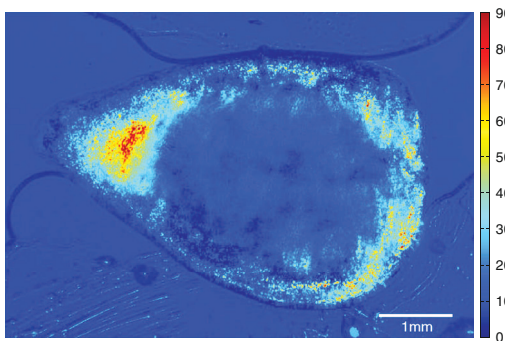


**Fig. 6** Retardance image, showing the absolute value of the linear retardance. Color bar is in degrees.

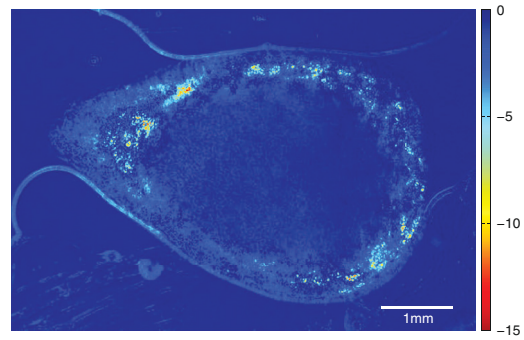


**Fig. 7** Optical rotation in degrees.

direction of the collagen fibers are mostly homogeneous through the sections. However, when characterizing the samples using MPM some variation in the direction with respect to the depth was observed, which would result in an intermediate direction in the MMI image and correspondingly different calculated values for the directional parameter.

In the intermediate layer (center of Fig. 6), where the MPM images cannot resolve individual collagen fibrils that are smaller than the imaging resolution limit, the MMI directional image shows structure variations and, thus, the ability to characterize the subresolution structures in this area of cartilage.

The collagen fibers in the cartilage scatter the incoming light, contributing to the depolarization (see Fig. 8). The depolarization will increase with the density and size of the collagen fibers, and could thus be useful for extracting more information about the collagen structure. By comparing the depolarization image (shown in Fig. 8) to the retardance image (shown in Fig. 6), one can see that the areas with a high depolarization index are mostly the same areas as the ones with high retardance, indicating a higher concentration or larger size of the collagen fibers, resulting in the higher depolarization. The reason the retardance is small in some areas of high depolarization could be attributed

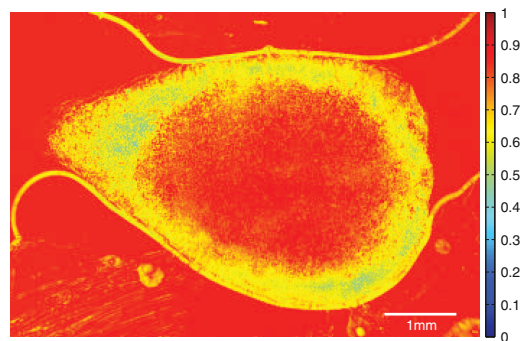


**Fig. 8** Depolarization index, where 1 is fully polarized and 0 fully depolarized.

**Table 1** Specific rotation for hyaluronic acid (HA), keratane sulfate (KS), and chondroitin sulfate (CS) in a water solution (Ref. 28). In addition, the specific rotation of collagen in 0.5M CaCl<sub>2</sub> is given (Ref. 27). The temperature at which the specific rotation is measured is given, when given in the source. The concentration of the chemical compounds in human femoral head cartilage from ages 3 to 19 are also given (Ref. 29). Total wet volume of tissue per unit weight of collagen ( $d_c^{-1}$ ) is  $4.96 \pm 0.041$  ml/g (Ref. 29).

Chemical substance	Specific rotation $[\alpha]_{589}$	Wet tissue weight percentage $w$
HA	-68.2 deg at 27°C	0.16
KS	4.5 deg	$0.83 \pm 0.095$
CS type A	-25 deg	$2.86 \pm 0.10$
Collagen	-360 deg at 8°C	$18.5 \pm 1.4$

to the collagen fibers in that area being aligned at an angle to the image plane, reducing the measured linear retardance.

An interesting observation is that the optical rotation (see Fig. 7) appears large compared to commonly reported values from solution. However, such large values may be justified by considering the triple helix<sup>25</sup> structure of the collagen together with proteoglycans. The left-handed collagen helix will induce optical rotation to the incoming polarized light. The amount of induced optical rotation is dependent on the orientation of the collagen fiber, with little contribution from out-of-plane fibers. Cartilage consists of proteoglycans, which contain<sup>26</sup> hyaluronic acid (HA), keratane sulfate (KS), and chondroitin sulfate (CS), all of which are optical active. The optical activity of these components are given in Table 1, together with their concentrations in femoral head cartilage. On the basis of these values, the expected optical rotation from a 100- $\mu$ m-thick solution of cartilage is calculated using

$$\phi = [\alpha_c]_{583} L d, \quad (1)$$

where  $\phi$  is the expected optical rotation,  $[\alpha_c]_{583}$  the specific rotation in Table 1 for the given compound,  $L$  the thickness of the sample in decimeter (here,  $10^{-3}$  dm), and  $d$  the density in (grams per milliliter), given here by  $d = d_c w_s / w_c$ , where  $d_c$  is the collagen density,  $w_s$  the substance weight percentage, and  $w_c$  the collagen weight percentage. Using (1) and values from Table 1 gives an optical rotation due to proteoglycans of  $-8.6 \times 10^{-4}$  deg, and due to collagen of  $-0.07$  deg at 583 nm, assuming that a 0.5 M CaCl<sub>2</sub> solution has the same optical rotation as water. The proteoglycan contribution to the optical rotation is thus negligible. The measurements of the optical rotation here were done at 980 nm, which is expected to give lower optical rotation due to the two-term Drude equation.<sup>27</sup> The optical rotation of the collagen fibers depends on their orientation. Hence, one would expect the ordered collagen fibers in the cartilage to have a higher optical rotation compared to randomly ordered collagen fibers in solution. This corresponds well to the observed values of optical rotation. Figure 7 shows structural variation across the image plane, believed to be caused by changes in the fibril direction relative to the image plane. However the variation in signal across the sample is different

compared to the retardance and depolarization images, indicating that additional information is stored in this image.

The comparison between the direction found from the MPM images and from the MMI images showed that they overall agreed quite well. Discrepancies could be seen toward the edges and at some isolated interior regions. Toward the edges, the Fourier analysis technique used in the MPM analysis will exhibit some artifacts as it picks up the edge of the sample as a strong frequency component (interpreted as a fiber) running tangential to the edge. If the fibers run perpendicularly to the edge, then this will be picked up by MMI and large discrepancies are expected. Other sources of discrepancies could be due to small collagen fibers not resolved by MPM and/or changes in the collagen direction through the sample (MPM could not image completely through the thickness of the sample). The tiling of the microscope images to create images of larger regions is evident in Figs. 1(a) and 2(a), which is due to uneven excitation over the imaging plane, probably due to movement of the beam at the back aperture of the objective. However, it appears that the transition between images is quite well filtered out during image analysis.

MMI will be unable to differentiate between collagen fibers running parallel to the sample surface and fibers that are at an angle to the surface. One way to distinguish these two cases would be to rotate the sample in the beam such that the Mueller matrix is extracted with the collagen fibers rotated at different angles to the incoming beams. By having enough different directions, it should be possible to extract a three-dimensional average direction of the fibers.

The structure of the collagen fibers as seen in the MPM images could be useful in the diagnosis and assessment of osteoarthritis. In this study, the MMI was performed in transmission mode; however the technique can also be applied in reflection mode, which would make it applicable for *in vivo* use. MMI can also be used in conjunction with high NA objectives to achieve even higher resolution images of the polarization properties. In the current setting, however, it is perhaps its ability to image large regions relatively fast that is its main advantage. Histopathology is another field where MMI could be very valuable. Its ability to generate more detailed polarization properties could make it valuable for better assessing the structure of diseased cartilage in histopathology studies. For example, the depolarization index and differences in linear and circular retardation are not picked up by regular polarization microscopes. The detailed structure that is possible to extract with these two imaging techniques could also have important applications in the study of the biomechanics of cartilage.

## 5 Conclusion

By applying an image-analysis technique based on the Fourier transform on the MPM images, we were able to quantify the direction of the fibers in the superficial layer. Combining this with Mueller matrix imaging proved to be a powerful combination, allowing for the extraction of directional parameters from the intermediate layer. The structure in the intermediate layer is usually assumed to be isotropic, but the retardance images clearly show that there is structural inhomogeneities in the connective tissue in these areas as well. In conclusion, the combination of

MMI and MPM provides a powerful technique in the study of osteoarthritis and other cartilage diseases.

### Acknowledgments

We acknowledge Linh Hoang, at the Department of pathology, Children and Women's Health at NTNU, for help in preparing the cartilage samples.

### References

1. W. C. Mow, W. Y. Gu, and F. H. Chen, *Structure and Function of Articular cartilage and Meniscus*, 3rd ed., pp. 181–258, Lippincott, Williams and Wilkins, Philadelphia (2005).
2. D. J. Hunter and D. T. Felson, "Osteoarthritis," *BMJ* **332**(7542), 639–642 (2006).
3. "National health interview survey," Tech. Rep., Center for Disease Control and Prevention (2009).
4. M. B. Kinds, P. M. J. Welsing, E. P. Vignon, J. W. J. Bijlsma, M. A. Viergever, A. C. A. Marijnissen, and F. P. J. G. Lafeber, "A systematic review of the association between radiographic and clinical osteoarthritis of hip and knee," *Osteoarth Cartilage* **19**(7), 768–778 (2011).
5. E. Yusuf, M. C. Kortekaas, I. Watt, T. W. J. Huizinga, and M. Kloppenburg, "Do knee abnormalities visualised on mri explain knee pain in knee osteoarthritis? a systematic review," *Ann. Rheum. Dis.* **70**(1), 60–67 (2011).
6. W. Denk, "Two-photon laser scanning fluorescence microscopy," *Science* **248**(4951), 73–76 (1990).
7. A. T. Yeh, M. J. Hammer-Wilson, D. C. Van Sickle, H. P. Benton, A. Zoumi, B. J. Tromberg, and G. M. Peavy, "Nonlinear optical microscopy of articular cartilage," *Osteoarth Cartilage* **13**(4), 345–352 (2005).
8. J. C. Mansfield, C. P. Winlove, J. Moger, and S. J. Matcher, "Collagen fiber arrangement in normal and diseased cartilage studied by polarization sensitive nonlinear microscopy," *J. Biomed. Opt.* **13**(4), 044020 (2008).
9. M. J. Levene, D. A. Dombeck, K. A. Kasischke, R. P. Molloy, and W. W. Webb, "In vivo multiphoton microscopy of deep brain tissue," *J. Neurophysiol.* **91**(4), 1908–1912 (2004).
10. M. B. Lilledahl, D. M. Pierce, T. Ricken, G. A. Holzapfel, and C. d. L. Davies, "Structural analysis of articular cartilage using multiphoton microscopy: input for biomechanical modelling," *IEEE Trans. Med. Imaging* (in press).
11. A. Erikson, J. Ortegren, T. Hompland, C. de Lange Davies, and M. Lindgren, "Quantification of the second-order nonlinear susceptibility of collagen I using a laser scanning microscope," *J. Biomed. Opt.* **12**(4), 044002 (2007).
12. L. M. S. Aas, P. G. Ellingsen, and M. Kildemo, "Near infra-red Mueller matrix imaging system and application to retardance imaging of strain," *Thin Solid Films* **519**, 2737–2741 (2011).
13. S. Y. Lu and R. A. Chipman, "Interpretation of Mueller matrices based on polar decomposition," *J. Opt. Soc. Am. A* **13**(5), 1106–1113 (1996).
14. S. Manhas, M. K. Swami, P. Buddhawant, N. Ghosh, P. K. Gupta, and K. Singh, "Mueller matrix approach for determination of optical rotation in chiral turbid media in backscattering geometry," *Opt. Express* **14**(1), 190–202 (2006).
15. N. Ghosh, M. F. G. Wood, and I. A. Vitkin, "Mueller matrix decomposition for extraction of individual polarization parameters from complex turbid media exhibiting multiple scattering, optical activity, and linear birefringence," *J. Biomed. Opt.* **13**(4), 044036 (2008).
16. N. Ghosh, M. F. G. Wood, S. Li, R. D. Weisel, B. C. Wilson, R. Li, and I. A. Vitkin, "Mueller matrix decomposition for polarized light assessment of biological tissues," *J. Biophot.* **2**(3), 145–56 (2009).
17. L.-W. Jin, K. A. Claborn, M. Kurimoto, M. A. Geday, I. Maezawa, F. Sohraby, M. Estrada, W. Kaminsky, and B. Kahr, "Imaging linear birefringence and dichroism in cerebral amyloid pathologies," *Proc. Natl. Acad. Sci.* **100**, 15294–15298 (2003).
18. M. Shribak and R. Oldenbourg, "Techniques for fast and sensitive measurements of two-dimensional birefringence distributions," *Appl. Opt.* **42**(16), 3009–3017 (2003).
19. W. Kaminsky, L.-W. Jin, S. Powell, I. Maezawa, K. Claborn, C. Branham, and B. Kahr, "Polarimetric imaging of amyloid," *Micron (Oxford, England: 1993)* **37**, 324–338 (2006).
20. E. Compain, S. Poirier, and B. Drevillon, "General and self-consistent method for the calibration of polarization modulators, polarimeters, and mueller-matrix ellipsometers," *App. Opt.* **38**, 3490–3502 (1999).
21. H. G. Tompkins and E. A. Irene, *Handbook of Ellipsometry*, Vol. 1, William Andrew Publishing/Noyes, Norwich, NY (2005).
22. S. R. Cloude, "Conditions for the physical realizability of matrix operations in polarimetry," *Proc. SPIE* **1166**, 177–185 (1989).
23. V. V. Tuchin, L. V. Wang, and D. A. Zimnyakov, *Optical Polarization in Biomedical Applications*, Springer-Verlag, Berlin (2006).
24. N. Ugryumova and S. J. Matcher, "Variable angle-of-incidence polarization-sensitive optical coherence tomography: its use to study the 3D collagen structure of equine articular cartilage," *Proc. SPIE* **6079**, 60792C (2006).
25. B. Brodsky and J. Ramshaw, "The collagen triple-helix structure," *Matrix Biol.* **15**, 545–554 (1997).
26. D. Heinegård and I. Axelsson, "Distribution of keratan sulfate in cartilage proteoglycan," *J. Bio. Chem.* **252**, 1971–1979 (1977).
27. P. H. Vonhippel and K. Y. Wong, "The collagen gelatin phase transition. II. shape of the melting curves and effect of chain length," *Biochemistry* **2**(6), 1399–1413 (1963).
28. Combined Chemical Dictionary Online Version 14.2," Taylor & Francis, Boca Raton, FL (2011).
29. A. Maroudas, M. T. Bayliss, and M. F. Venn, "Further studies on the composition of human femoral head cartilage," *Ann. Rheum. Dis.* **39**(5), 514–523 (1980).



P. G. Ellingsen, L. M. S. Aas, V. S. Hagen, R. Kumar, M. B. Lilledahl, and M. Kildemo, “Mueller matrix three-dimensional directional imaging of collagen fibers,” *J. Biomed. Opt.* **19**, 26002 (2014)

## Paper 6



# Mueller matrix three-dimensional directional imaging of collagen fibers

Pål Gunnar Ellingsen, Lars Martin Sandvik Aas, Vegard Stenhjem Hagen, Rajesh Kumar, Magnus Borstad Lilledahl, and Morten Kildemo\*

Norwegian University of Science and Technology, Department of Physics, Faculty of Natural Sciences and Technology, Trondheim, Norway

**Abstract.** A method for measuring three-dimensional (3-D) direction images of collagen fibers in biological tissue is presented. Images of the 3-D directions are derived from the measured transmission Mueller matrix images (MMIs), acquired at different incidence angles, by taking advantage of the form birefringence of the collagen fibers. The MMIs are decomposed using the recently developed differential decomposition, which is more suited to biological tissue samples than the common polar decomposition method. Validation of the 3-D direction images was performed by comparing them with images from second-harmonic generation microscopy. The comparison found a good agreement between the two methods. It is envisaged that 3-D directional imaging could become a useful tool for understanding the collagen framework for fibers smaller than the diffraction limit. © The Authors. Published by SPIE under a Creative Commons Attribution 3.0 Unported License. Distribution or reproduction of this work in whole or in part requires full attribution of the original publication, including its DOI. [DOI: 10.1117/1.JBO.19.2.026002]

Keywords: Mueller matrix imaging; collagen; directional imaging; second-harmonic.

Paper 130673RR received Sep. 16, 2013; revised manuscript received Jan. 6, 2014; accepted for publication Jan. 7, 2014; published online Feb. 6, 2014.

## 1 Introduction

Biomedical research is experiencing a revolution due to the development of instruments for spectral and spatial characterization. In addition, pulsed lasers are readily available for nonlinear optical applications. Recently, polarization sensitive techniques, known from the thin film community, have been developed for biomedical applications. In the thin film community, the polarization sensitive technique spectroscopic ellipsometry has been successfully used to characterize material properties of many kinds for several decades.<sup>1</sup> As a consequence, ellipsometry now plays an important role in the semiconductor industry. More recently, spectroscopic Mueller matrix ellipsometry has been employed to characterize anisotropic nanostructured materials and plasmonic structures.<sup>2-6</sup> Due to the turbidity of biological tissue,<sup>7</sup> the modeling is more complicated than for more uniform samples such as thin films. In addition, partial depolarization of light in the sample requires acquisition of the full polarization properties, i.e., the Mueller matrix, and not only the ellipsometric parameters  $\Psi$  (amplitude) and  $\Delta$  (phase difference). Nevertheless, Mueller matrix ellipsometry has been shown to be a promising technique for the characterization of biological tissue.<sup>8-13</sup>

Recently, several setups have been developed to acquire Mueller matrix images (MMIs) of biological samples. In particular, Pierangelo et al.<sup>13</sup> demonstrated the use of a reflection imaging Mueller matrix ellipsometer to characterize and diagnose colorectal cancer. Furthermore, several broadband Mueller matrix designs for imaging have been proposed<sup>14</sup> and some have been implemented.<sup>15</sup> By carefully choosing the probing wavelength, it is possible to make the technique sensitive to a certain depth range in the tissue.<sup>7</sup> Hence, if MMI is combined with hyperspectral imaging it would be possible to study the depth dependent effects. The MMI technique is, in

principle, nondestructive and can, with further development, achieve a submicrometer resolution, as well as being sensitive to structural features smaller than the diffraction limit.

There are a range of polarization effects which alters a Mueller matrix, the common being depolarization, diattenuation, birefringence, and optical activity. If a material possesses several of these effects, it is not always easily seen from the Mueller matrix which of the effects are responsible for a certain feature in the measured data. One way of simplifying the analysis is to decompose the measured Mueller matrix. The typical way of decomposing the Mueller matrix has been the forward polar decomposition,<sup>16,17</sup> but recently, Ossikovski et al.<sup>18</sup> pointed out that polar decomposition assumes the polarization effects to be multiplicative, which is rarely the case for biological media. They suggested that the differential decomposition is a more suitable approach for decomposing such simultaneous effects. The differential decomposition was originally proposed by Azzam<sup>19</sup> and later extended to include depolarizing media by Ossikovski<sup>20</sup> and has recently been applied on biological tissue by Kumar et al.<sup>12</sup> In the latter work, it was shown how to calculate physical properties from the decomposed matrices.

Using decomposed MMIs of biological tissue containing collagen fibers, it has been shown possible to extract the in-plane direction of the fibers from their induced birefringence.<sup>11</sup> We, here, generalize this idea further in order to find the 3-D direction of collagen fibers in biological tissue. This generalized method is tested and validated by comparing the three-dimensional (3-D) direction image of tendon derived from MMIs, with second-harmonic (SHG) images of the same sample. SHG imaging is well known to be a good diffraction limited technique for imaging collagen fibers.<sup>21,22</sup>

## 2 Materials and Methods

### 2.1 Sample Preparation

Tendon tissue was taken from medial femoral condyle of a chicken's knee, bought fresh from the supermarket. A small

\*Address all correspondence to: Morten Kildemo, E-mail: morten.kildemo@ntnu.no

section of the tissue was embedded in a mounting medium for cryo-sectioning (O.C.T., Sakura, Alphen aan den Rijn, The Netherlands). Rapid freezing of the O.C.T. embedded tissue was completed using liquid nitrogen. This frozen section was stored in a freezer ( $-60^{\circ}\text{C}$ ) until cut with a cryostat into  $50\text{-}\mu\text{m}$  thin tissue sections. The cutting plane was parallel to the collagen fibers. The thin sections were placed on standard microscope glass slides and stored in a freezer ( $-60^{\circ}\text{C}$ ). Before being measured, the tissue samples were brought back to room temperature and covered with a standard cover slip. Edges of the cover slip were sealed with Vaseline to avoid dehydration. Between measurements, the slides were stored at  $4^{\circ}\text{C}$ .

## 2.2 SHG Imaging

SHG images were collected on a Zeiss LSM 510 meta microscope using a Coherent Mira 900 for excitation at  $790\text{ nm}$ . Imaging was done with a  $40\times 1.2\text{ NA}$  objective. A custom built polarization setup, which compensates for any birefringence in the optical path, was used to ensure circular polarization. The average power at the focal plane was approximately 8.

## 2.3 MMI Setup

After the samples were imaged with SHG, they were measured in a custom built MMI ellipsometer, shown in Fig. 1. The system uses ferroelectric liquid crystals for both the polarization state generator and analyzer. Details of the system can be found in Aas et al.<sup>23</sup> An improvement was made to the illumination, by replacing both the laser and rotating diffuser, with a  $940\text{ nm}$  collimated light emitting diode (LED). In addition, a motorized rotation stage for the sample was introduced in order to image the sample at the different projections needed to extract the 3-D direction, as described below.

The system was calibrated using the eigenvalue calibration method<sup>24</sup> on four reference samples (air, two polarizers, and a retarder), ensuring the correct measurement of the Mueller matrix. By comparing the measurement of air to the identity matrix, an error estimate was made resulting in a measure for the accuracy of the system.

## 2.4 Decomposition of the Mueller Matrix

As the differential decomposition method is able to decompose simultaneous polarization effects, it was chosen for the decomposition of the measured Mueller matrices presented here. Due to the measurement noise, some of the measured Mueller matrices are slightly unphysical, which was compensated for by using the filtering described by Cloude,<sup>25</sup> prior to the decomposition.

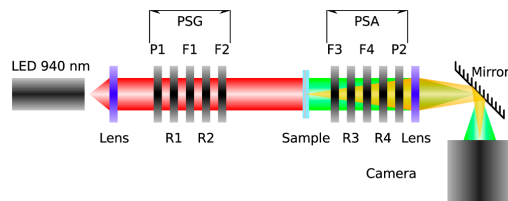


**Fig. 1** The Mueller matrix imaging (MMI) setup consisting of the polarization state generator (PSG) and the polarization state analyzer (PSA). P1 and P2 are the linear polarizers, R1, ..., R4 are the retarders and F1, ..., F4 are the ferroelectric liquid crystals.

The differential decomposition results in two matrices,  $L_m$  and  $L_u$ ,<sup>20</sup> where  $L_m$  contains the elements used to calculate the retardance and the diattenuation. The uncertainties (standard deviation) in the retardance and the diattenuation can be calculated by using the same matrix elements from  $L_u$  as those originally used from  $L_m$ . Furthermore, the depolarization can be calculated from  $L_u$ . In this study, the relevant properties are the linear retardance  $\delta$ , the angle of orientation of the linear retardance  $\theta$ , and the depolarization  $\Delta$  (It is here noted that the depolarization  $[\Delta^{\log-M}$ , Eq. (19) in the paper by Kumar et al.<sup>12</sup>] has the wrong signs of the exponential, it should be  $\Delta^{\log-M} = 1 - (1/3)(e^{\alpha_1} + e^{\alpha_2} + e^{\alpha_3})$  as discussed in a private correspondence with Ossikovski, one of the authors of the original paper.).<sup>12</sup>

## 2.5 Directional Calculation

In every day life, we are familiar with determining the orientation of an object just by looking at it. Because our eyes are separated by a distance, they see two different projections of an object which enables deduction of the object's orientation. The MMI setup can only image one projection, but it is possible to rotate the sample in two different sample rotations  $\alpha$ , see Figs. 2 and 3, and then use the two resulting images to calculate the direction of the imaged birefringent structure, i.e., the collagen framework.

In order to derive the direction of anisotropic structures, it is convenient to start with the Euler transformations.<sup>26</sup> They require the definition of two coordinate systems, the laboratory frame of reference and the sample frame of reference. Let  $\mathbf{p} = [x, y, z]$  describes a vector in the laboratory frame of reference. The frame of reference is defined in such a way that the  $x$ -axis points along the direction of illumination, the  $y$ -axis is horizontal, and the  $z$ -axis is vertical, see Fig. 2. Let  $\mathbf{p}' = [x', y', z']$  be a vector in the sample frame of reference. The sample frame of

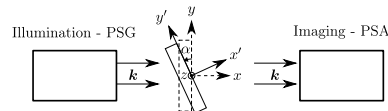


**Fig. 2** Rotation  $\alpha$  of the sample seen from above the setup.

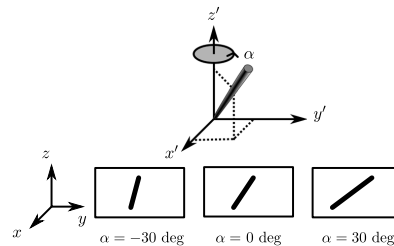


**Fig. 3** The coordinate systems used for the calculation of the directions. The laboratory frame ( $xyz$ ) is identical to the sample frame of reference ( $x'y'z'$ ) at  $\alpha = 0$ . The  $x$ -axis points along the illumination direction toward the camera and  $z$  is vertical. As the rotation is around  $z$ ,  $z' = z$  for any  $\alpha$ . The lower row of figures shows the projection of a three-dimensional (3-D) fiber onto the imaging plane, for different rotations of the sample ( $\alpha$ ).

reference coincides with the laboratory frame for a rotation  $\alpha = 0$  deg, see Fig. 2. The sample is only rotated around the  $z = z'$  axis, see Figs. 2 and 3, resulting in the following Euler rotation matrix

$$\mathbf{R}(\alpha) = \begin{bmatrix} \cos \alpha & \sin \alpha & 0 \\ -\sin \alpha & \cos \alpha & 0 \\ 0 & 0 & 1 \end{bmatrix}. \quad (1)$$

By using this transformation, it is possible to transform from the sample frame of reference  $\mathbf{p}'$  to the laboratory frame of reference  $\mathbf{p}$ , by  $\mathbf{p} = \mathbf{R}(-\alpha)\mathbf{p}'$ . Applying this transformation gives the following relations

$$\begin{aligned} x &= x' \cos \alpha - y' \sin \alpha, \\ y &= x' \sin \alpha + y' \cos \alpha, \\ z &= z'. \end{aligned} \quad (2)$$

The goal is to determine  $\mathbf{p}'$  by measuring the Mueller matrix at two different sample rotations,  $\alpha_1$  and  $\alpha_2$ , by looking at the projections into the laboratory frame of reference (the measured image), resulting in the measured  $(y_1, z_1)$  and  $(y_2, z_2)$ . By choosing  $\alpha_2 = -\alpha_1 = \alpha$ , (in our setup  $\alpha_2 < 0$  due to the direction of rotation) and solving Eq. (2), the components of  $\mathbf{p}'$  results in

$$x' = \frac{y_2 - y_1}{2 \sin \alpha}, \quad y' = \frac{y_1 + y_2}{2 \cos \alpha}, \quad z' = z_1 = z_2. \quad (3)$$

As the MMI measurement only yields the direction of the slow axis,  $\theta$ , and not the projected length (the length in the  $yz$  plane) of the fiber, it is not possible to find the absolute value (length) of the vector. In order to resolve this, we define the projected length of the fiber as

$$\begin{aligned} l &= \sqrt{y^2 + z^2} \\ &= \sqrt{x'^2 \sin^2 \alpha + y'^2 \cos^2 \alpha + 2x'y' \sin \alpha \cos \alpha + z'^2}. \end{aligned}$$

It is now possible to define the coordinates with respect to the measured angles

$$\begin{aligned} y_1 &= l_1 \cos \theta_1, & z_1 &= l_1 \sin \theta_1, \\ y_2 &= l_2 \cos \theta_2, & z_2 &= l_2 \sin \theta_2. \end{aligned}$$

Using  $z_1 = z_2 = z$  we find that

$$y_1 = z \cot \theta_1, \quad y_2 = z \cot \theta_2,$$

which, when inserted into Eq. (3), gives

$$x' = \frac{z(\cot \theta_2 - \cot \theta_1)}{2 \sin \alpha}, \quad y' = \frac{z(\cot \theta_1 + \cot \theta_2)}{2 \cos \alpha}, \quad z' = z.$$

These equations depend on the absolute length of  $z$ , however, as we are only interested in the direction of the fiber, we can set  $z = 1$ . This solution is limited to only include positive  $z$ , which is not a problem since all solutions with negative  $z$  can be represented by the opposite vector located in the positive  $z$  space. In addition, it will not be possible to get a solution purely in the  $xy$

plane ( $z = 0$ ). A real measurement contains some noise, both from the measurement itself and from numerical noise, ensuring that the angle is never exactly zero. In addition, the rotation around  $z$  means that it is not possible to see the difference between different vectors in the  $xy$  plane if  $z = 0$ . The final equations are then

$$x' = \frac{\cot \theta_2 - \cot \theta_1}{2 \sin \alpha}, \quad y' = \frac{\cot \theta_1 + \cot \theta_2}{2 \cos \alpha}, \quad z' = 1. \quad (4)$$

When presenting the results derived with Eq. (4), the vector is normalized to its length  $\sqrt{x'^2 + y'^2 + z'^2}$ .

Another consideration to make is that the angle of incidence is not the same as the rotation angle of the sample, due to the difference in refractive index. This difference yields a correction for  $\alpha$  which is  $\alpha = \arcsin[\sin(\alpha_r)/n_t]$ , where  $\alpha_r$  is the angle of rotation (incidence angle on the glass) and  $n_t$  is the refractive index of tissue, assumed here to be 1.4.<sup>7</sup> According to Snell's law, the two glass slides sandwiching the sample do not affect this correction.

## 2.6 Directional Imaging

By changing the angle of incidence on the sample, i.e., rotating the sample, and using the slow axis direction found from the decomposition, it is possible to calculate and hence make an image of the 3-D direction of the fibers as described in Sec. 2.5. The calculation is done using incidence angles of  $\alpha_r = \pm 30$  deg. The resulting images are resampled, using  $\alpha_r$ , such that the stretching due to rotation is counteracted and the pixels are square.  $\alpha_r$  is used because the image is seen on the surface of the glass.

## 3 Results and Discussion

Two of the recorded Mueller matrices, after cropping and resampling, are shown in Fig. 4. The first element of the Mueller matrix has the intensity image overlaid. These Mueller matrices are the basis for the decomposition and calculating the directions as explained in Sec. 3.2.

### 3.1 Depolarization and Linear Retardance

Linear retardance describes how much the polarization in one direction is phase shifted with respect to its orthogonal polarization. Figure 5 shows the linear retardance together with its uncertainty for the tendon sample. The uncertainty is calculated from  $L_u$  and represents the standard deviations of the linear retardance. As previously reported,<sup>11</sup> a high concentration of collagen results in a high retardance, mainly due to the form birefringence induced by the shape of the fibers in the effective

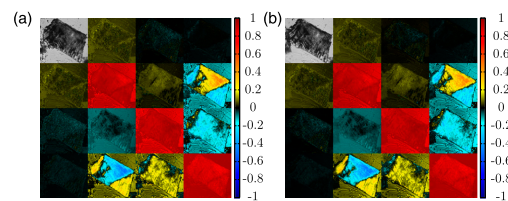
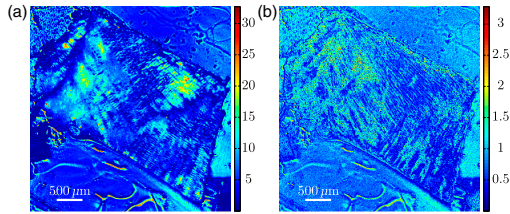


Fig. 4 The normalized, cropped, and resampled MMI for 30 deg (a) and -30 deg (b), with the intensity image (gray scale image) overlaid the first element in the Mueller matrix as it is 1 in every pixel.



**Fig. 5** Linear retardance (a) and the uncertainty (b) for the tendon sample at normal incidence. Both images are in degrees.

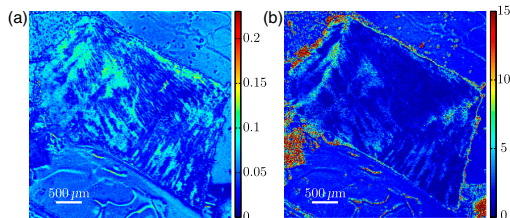
medium. The mentioned study looked at the collagen fibers present in cartilage, which is less ordered than the collagen fibers in tendons. Being less ordered means that the structure should be modeled as a multilayered effective medium (requiring a layered decomposition of the Mueller matrix) with one orientation for every layer. The higher degree of order in the tendon makes the presented results more clear, and thus avoids the need to consider the sample as a multilayered system.

Figure 5(b) shows the uncertainty image (standard deviation) of the linear retardance, which is seen to be above the random noise level in some areas. As the uncertainty in this figure is a result of depolarization effects, it is useful for the analysis of the sample. Previous evaluation of the uncertainty has been limited to the knowledge of the measurement error found from the calibration. Specifically, the error is found from the measurement of air which, here, results in a measurement error on the order of a few percents. The uncertainty image supplies additional information about the sample. It gives a measure for the uncertainty induced by randomness in the sample. This randomness can, for instance, be the fiber orientations and/or sizes, as well as depolarizing effects like multiple scattering and integration over several polarization states in one pixel. This is confirmed by comparing the uncertainty measurement to the depolarization shown in Fig. 6(a).

### 3.2 Directional Imaging

From the retardance found in the decomposition, it is not only possible to calculate the linear retardance, but also the direction of the fast axis of the birefringence. This latter property can, together with the correct effective medium model, be used to find the direction of the collagen fibers as explained in Sec. 2.

The directional image and the SHG image for the tendon sample are shown in Fig. 7. As the 3-D directional image in



**Fig. 6** (a) Depolarization at normal incidence for the tendon sample. The color scale is from 0 for fully polarized to 1 for fully depolarized. (b) Uncertainty in the direction of the slow axis for normal incidence. The color scale is in degrees.

Fig. 7(a) shows, the fibers are mostly in the plane, as expected due to the direction of the cryostat cut. The calculated in-plane directions [black lines in Figs. 7(a) and 7(b)] correspond very well with the apparent directions in the SHG images [Figs. 7(c) and 7(e)]. There are some areas that are clearly out-of-plane [red areas in the 3-D directional image, Fig. 7(a)], which in the SHG images are either dark or show some weak structure. The latter can be explained by the SHG signal generation. When considering SHG signal generation, fiber orientations are important, as a fiber in-plane has a much larger cross section for generating SHG, compared to one out-of-plane. This means that the darker parts of the image in Fig. 7(c) probably are due to an out-of-plane orientation of the fibers, in accordance with the 3-D directional image. Figure 7(d) shows an overlay of the out-of-plane part of Fig. 7(a) and the SHG image in Fig. 7(c).

The lower right of the sample shows an offset between the directional image and the SHG. There could be several reasons for this offset, one being that the size of the fibers is around the upper limit of the validity of the effective medium model, which is  $\sim\lambda$  (here  $\lambda = 940$  nm). In this study, it was necessary that the fibers were sufficiently large to visualize with SHG, which is limited by the diffraction limit. It is expected that the MMI results will be superior for smaller fibers.

Another contributing factor to the error in the direction is the depolarization induced uncertainties in the direction of the fast axis. The calculation of this uncertainty was not given by Kumar et al.<sup>12</sup> as it cannot be calculated from  $L_u$  in the same way as the uncertainty in the other parameters. As a solution to this, we have calculated the uncertainty, shown in Fig. 6(b), using the standard method for propagation of errors, here, the uncertainties found in  $L_u$ . If the propagation is made at an incidence angle of 0 deg, the resulting uncertainty in the angle of the fast axis is given by

$$\sigma_\theta = \sqrt{\frac{[L_u(2,4)]^2}{4[L_m(3,4)]^2 \left\{ 1 + \frac{[L_m(2,4)]^2}{[L_m(3,4)]^2} \right\}^2} + \frac{[L_u(3,4)]^2 [L_m(2,4)]^2}{4[L_m(3,4)]^4 \left\{ 1 + \frac{[L_m(2,4)]^2}{[L_m(3,4)]^2} \right\}^2}} \quad (5)$$

The reasons for choosing to study the uncertainty at an incidence angle of 0 deg, instead of  $\pm 30$  deg, are due to the approximations used to derive the propagation uncertainty. Propagation of uncertainties uses only the first derivatives and not the higher orders, which for Eq. (4) might be an incorrect approximation. The uncertainty at 0 and  $\pm 30$  deg is expected to be similar, although the exact relation is hard to predict. A prediction is hard because there could be a reduction in the uncertainty as a result of the increase in the number of data points (two data sets), although the increase in apparent thickness could on the other hand increase the uncertainty. As a consequence, the 0 deg uncertainty will be used as a good indication for the  $\pm 30$  deg uncertainty.

By studying Fig. 6(b), it is possible to see that the uncertainty in the directions is larger in the lower right part of the sample compared to the upper, which is in accordance with the comparison between the 3-D image and the SHG image, shown in Fig. 7. In addition, by comparing with Fig. 6(a), it is seen that they correlate well showing that the uncertainty is a result of the depolarization. As the depolarization is generated by, among others,

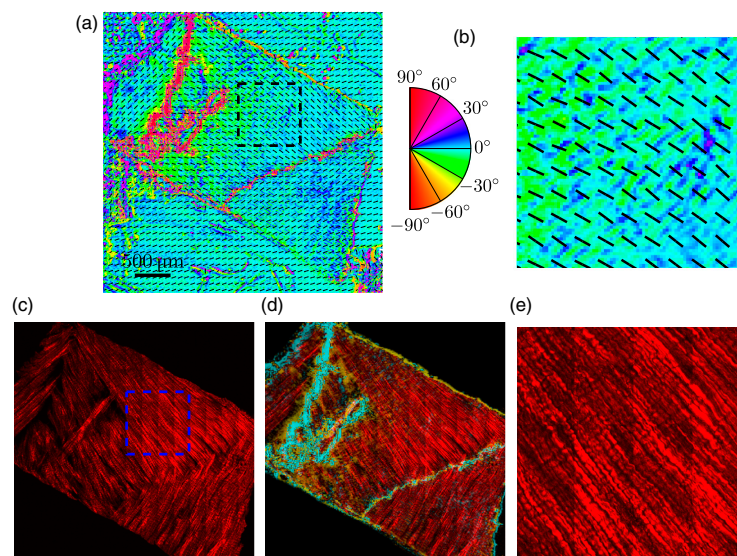


**Fig. 7** 3-D directional image (a) with a zoomed view (b), an SHG image (c) with a zoomed in view (e) and an overlay of the SHG and the out-of-plane direction of the tendon (d). The colorwheel beside the directional image shows the out-of-plane direction in degrees, with 0 deg being in the image plane and  $\pm 90$  deg normal to the image plane. +90 deg is the direction toward the reader (positive  $\Delta \log -M$ ). The overlay (d) (area outside of the sample masked for clarity) shows the SHG and out-of-plane directions overlain. The yellow color represent the negative out-of-plane direction and the cyan the positive direction. No color represents an in-plane direction and increasing color more out-of-plane.

the randomness of the fiber orientations, it offers a better understanding of the sample structure.

The out-of-plane directions in Fig. 7 are seen to correspond well with the same areas in the SHG image. Additionally, by studying Fig. 7(a) and the zoomed in views in Figs. 7(b) and 7(e), it is possible to see that the oscillating structure (the oscillation between green and blue) along the fibers is visible both in the SHG image and the out-of-plane direction image. Both of these results confirm that the 3-D directional imaging finds the correct directions.

It is worth noting that the method described above makes it possible to find the fiber directions using MMI, even though the resolution in our system is much poorer than for SHG. Another notable property is that this method only requires the sample to be birefringent, as the calculation is based on the direction of linear retardance. Linear retardance is present in a range of different biologicals,<sup>9</sup> colloids,<sup>27</sup> and solid matter systems,<sup>23</sup> extending the possible applications for the method.

#### 4 Conclusion

We have presented a method for determining the 3-D direction of collagen fibers embedded in biological tissue from MMIs. The resulting images are shown to be in good agreement for a tendon sample when compared to SHG images. In particular, it is possible to see oscillating structures in the collagen orientation, as well as the out-of-plane directions of the fibers. The possibility to see effects from collagen fibers below the diffraction limit could be an important input to the understanding of how the collagen framework looks. Additionally, the use of the differential decomposition instead of the, until now, most

common polar decomposition has provided a good insight into the uncertainties in the calculation of the physical properties.

#### Acknowledgments

The authors would like to thank Razvigor Ossikovski for the correspondence on the implementation of the differential decomposition method.

#### References

1. R. M. A. Azzam and N. M. Bashara, *Ellipsometry and Polarized Light*, North-Holland Publishing, Amsterdam (1977).
2. D. Schmidt et al., "Optical, structural, and magnetic properties of cobalt nanostructure thin films," *J. Appl. Phys.* **105**(11), 113508 (2009).
3. I. Nerbø et al., "Real-time in situ Mueller matrix ellipsometry of GaSb nanopillars: observation of anisotropic local alignment," *Opt. Express* **19**(13), 571–575 (2011).
4. L. Aas et al., "Determination of small tilt angles of short GaSb nanopillars using UV-visible Mueller matrix ellipsometry," *Thin Solid Films* **541**, 97–101 (2013).
5. T. Oates, H. Wormeester, and H. Arwin, "Characterization of plasmonic effects in thin films and metamaterials using spectroscopic ellipsometry," *Prog. Surf. Sci.* **86**(11–12), 328–376 (2011).
6. L. M. S. Aas et al., "Optical properties of biaxial nanopatterned gold plasmonic nanowired gridpolarizer," *Opt. Express* **21**(25), 30918–30931 (2013).
7. V. V. Tuchin, *Tissue Optics: Light Scattering Methods and Instruments for Medical Diagnosis*, 2nd ed., SPIE Press, Bellingham, WA (2007).
8. J. Chung et al., "Use of polar decomposition for the diagnosis of oral precancer," *Appl. Opt.* **46**(15), 3038–3045 (2007).
9. N. Ghosh et al., "Mueller matrix decomposition for polarized light assessment of biological tissues," *J. Biophotonics* **2**(3), 145–156 (2009).

10. M.-R. Antonelli et al., "Mueller matrix imaging of human colon tissue for cancer diagnostics: how Monte Carlo modeling can help in the interpretation of experimental data," *Opt. Express* **18**(10), 10200 (2010).
11. P. G. Ellingsen et al., "Quantitative characterization of articular cartilage using Mueller matrix imaging and multiphoton microscopy," *J. Biomed. Opt.* **16**(11), 116002 (2011).
12. S. Kumar et al., "Comparative study of differential matrix and extended polar decomposition formalisms for polarimetric characterization of complex tissue-like turbid media," *J. Biomed. Opt.* **17**(10), 105006 (2012).
13. A. Pierangelo et al., "Multispectral Mueller polarimetric imaging detecting residual cancer and cancer regression after neoadjuvant treatment for colorectal carcinomas," *J. Biomed. Opt.* **18**(4), 046014 (2013).
14. P. A. Letnes et al., "Fast and optimal broad-band Stokes/Mueller polarimeter design by the use of a genetic algorithm," *Opt. Express* **18**(22), 23095–23103 (2010).
15. L. M. S. Aas et al., "Overdetermined broadband spectroscopic Mueller matrix polarimeter designed by genetic algorithms," *Opt. Express* **21**(7), 8753–8762 (2013).
16. S.-Y. Lu and R. A. Chipman, "Interpretation of Mueller matrices based on polar decomposition," *J. Opt. Soc. Am. A* **13**(5), 1106–1113 (1996).
17. S. Manhas et al., "Mueller matrix approach for determination of optical rotation in chiral turbid media in backscattering geometry," *Opt. Express* **14**(1), 190–202 (2006).
18. R. Ossikovski, A. De Martino, and S. Guyot, "Forward and reverse product decompositions of depolarizing Mueller matrices," *Opt. Lett.* **32**(6), 689691 (2007).
19. R. Azzam, "Propagation of partially polarized light through anisotropic media with or without depolarization: a differential  $4 \times 4$  matrix calculus," *J. Opt. Soc. Am.* **68**(12), 1756–1767 (1978).
20. R. Ossikovski, "Differential matrix formalism for depolarizing anisotropic media," *Opt. Lett.* **36**(12), 2330–2332 (2011).
21. P. Stoller et al., "Quantitative second-harmonic generation microscopy in collagen," *Appl. Opt.* **42**(25), 5209–5219 (2003).
22. G. Cox et al., "3-Dimensional imaging of collagen using second harmonic generation," *J. Struct. Biol.* **141**(1), 53–62 (2003).
23. L. M. S. Aas, P. G. Ellingsen, and M. Kildemo, "Near infra-red Mueller matrix imaging system and application to retardance imaging of strain," *Thin Solid Films* **519**(9), 2737–2741 (2011).
24. E. Compain, S. Poirier, and B. Drevillon, "General and self-consistent method for the calibration of polarization modulators, polarimeters, and Mueller-matrix ellipsometers," *Appl. Opt.* **38**(16), 3490–3502 (1999).
25. S. R. Cloude, "Conditions for the physical realisability of matrix operations in polarimetry," *Proc. SPIE* **1166**, 177–185 (1990).
26. H. Goldstein, C. Poole, and J. Safko, *Classical Mechanics*, 3rd ed., Addison Wesley, San Francisco, CA (2002).
27. M. Kildemo et al., "Mueller matrix imaging of nematic textures in colloidal dispersions of Na-fluorohectorite synthetic clay," *Proc. SPIE* **8082**, 808221 (2011).

Biographies of the authors are not available.



P. G. Ellingsen, N. K. Reitan, B. D. Pedersen, and M. Lindgren, "Hyperspectral analysis using the correlation between image and reference," *J. Biomed. Opt.* **18**, 20501 (2013)

**Paper 7**



# Hyperspectral analysis using the correlation between image and reference

Pål Gunnar Ellingsen, Nina Kristine Reitan, Brede Dille Pedersen, and Mikael Lindgren

Norwegian University of Science and Technology, Department of Physics, Trondheim, Norway

**Abstract.** We present the use of correlation analysis on spectral data in order to quantify the amount of a given spectrum present with respect to a reference spectrum. The method is shown to be useful in analyzing hyperspectral fluorescence images. It is unhindered by the linear relationship assumed in linear spectral unmixing, and in addition, it is shown to be robust with respect to noise. © The Authors. Published by SPIE under a Creative Commons Attribution 3.0 Unported License. Distribution or reproduction of this work in whole or in part requires full attribution of the original publication, including its DOI. [DOI: 10.1117/1.JBO.18.2.020501]

Keywords: correlation analysis; hyperspectral imaging; spectral analysis.

Paper 12754L received Nov. 22, 2012; revised manuscript received Dec. 29, 2012; accepted for publication Jan. 3, 2013; published online Jan. 15, 2013.

The use of spectra in the identification and characterization of biological and chemical substances is constantly growing as the different measurement techniques are simplified and commercialized. The expansion from detecting a single spectrum from one point in the sample to measuring spectra for every pixel with a hyperspectral camera has opened the door to a lot of new applications. It has not yet reached its full potential, though it is used extensively in remote sensing, and it is now becoming part of commercial imaging setups for biomedical applications. In particular, the use of hyperspectral imaging in confocal microscopes (for example, the Zeiss META system) in microscopic analysis as classification in fluorescence in situ hybridization (FISH)<sup>1</sup> and fluorescence microscopes has emerged. With this availability, the need for good methods for analyzing the large data sets (known as hyperspectral cubes) is apparent. Common ways of doing this analysis is by using principle component analysis (PCA)<sup>2</sup> or linear spectral unmixing.<sup>3</sup> In remote sensing, there has also been some usage of spectral mixture analysis<sup>4</sup> and spectral angle mapping,<sup>5</sup> as compared by Dennison et al.<sup>6</sup>

PCA works on the full hyperspectral cube without making assumptions about the sample, and it projects the spectral data into a new orthogonal basis, where the axes are computed with respect to the largest spread in the spectral data between pixels. In comparison, spectral unmixing works individually

on each pixel and assumes that the resulting spectrum in a pixel is a linear combination of a set of reference spectra, and solves for the amount of each reference spectra using linear algebra. These techniques are straightforward and work well for samples with high signal-to-noise ratios and small effects from interfering background signals.

We use the data from individual pixels in the image, just as in the case of linear unmixing, but the analysis is based on the correlation coefficient<sup>7</sup>

$$\rho_{XY} = \frac{\sigma_{XY}}{\sigma_X \sigma_Y}, \quad (1)$$

where  $X$  and  $Y$  are random variables,  $\sigma_{XY}$  is the covariance between  $X$  and  $Y$ , and  $\sigma_X$ ,  $\sigma_Y$  is the standard deviation for  $X$  and  $Y$ , respectively. The correlation coefficient is scale-free, meaning that it is independent of the units of measure for  $X$  and  $Y$ . Its resulting value will be in the interval  $-1 \leq \rho_{XY} \leq 1$ , where 1 corresponds to ( $Y = X$ ) and  $-1$  to  $Y = -X$ . In the case of hyperspectral data, the variables  $X$  and  $Y$  are the two spectra (one from the image and one from the reference) with  $N$  data points each, and the correlation coefficient (which will be called *correlation* from now on) is, then, given by

$$\rho_{XY} = \frac{\sum_{i=1}^N (X_i - \bar{X})(Y_i - \bar{Y})}{\sqrt{\sum_{i=1}^N (X_i - \bar{X})^2} \sqrt{\sum_{i=1}^N (Y_i - \bar{Y})^2}},$$

where  $\bar{X}$ ,  $\bar{Y}$  are the mean values of  $X$  and  $Y$ .

This method is robust with respect to noise, and it has been used for decades in remote sensing applications such as radar, where it can recover signals with signal-to-noise values of less than 1.<sup>8,9</sup> Since the signal-to-noise ratio in hyperspectral data can be low, due to the total intensity being separated into numerous wavelength channels, the use of correlation is favorable on such signals.

As an application of the correlation analysis, a 379-day-old male APP/PS1 mouse was injected with the well-known luminescent conjugated oligothiophene (LCO) pFTAA,<sup>10-12</sup> which is known to bind to amyloid  $\beta$  plaques in the brain that are known to be related to the progression of Alzheimer's disease.<sup>10-12</sup> Specifically, APP/PS1 mice were given two consecutive injections of pFTAA [or PBS for a reference autofluorescence (AF) spectrum] and were sacrificed 24 h after the second injection. The brain was snap-frozen, and 30  $\mu\text{m}$  cryo sections were prepared. These sections were fixed in ethanol, rehydrated with PBS, and mounted with Dako fluorescence mounting medium (Dako Cytomation, Glostrup, Denmark).

In addition, a reference brain section from a 174-day-old female APP/PS1 mouse was injected with PBS buffer and used as reference for the AF. Both of these were imaged using a Carl Zeiss AG LSM 510 META system with a laser excitation of 800 nm. This excitation ensured 2-photon absorption at 400 nm in the sample, yielding visible fluorescence from the pFTAA as well as the AF. The oligothiophene pFTAA and other related polymer analogs, such as PTAA, are known to have an appreciable 2-photon absorption cross section at 800 nm.<sup>13</sup> The fluorescence was then recorded into a spectrum for every pixel by the attached multichannel META detector. These pixels were then put together into a hyperspectral image. By acquiring such images for both the pFTAA and PBS sections, the correlation analysis could be done on the pFTAA brain section. The reference spectrum for the AF was found by imaging 10 plaques at an excitation wavelength of 800 nm,

Address all correspondence to: Mikael Lindgren, Norwegian University of Science and Technology, Department of Physics, Trondheim, Norway. Tel: +47 73593414; Fax: +47 73597710; E-mail: mikael.lindgren@ntnu.no

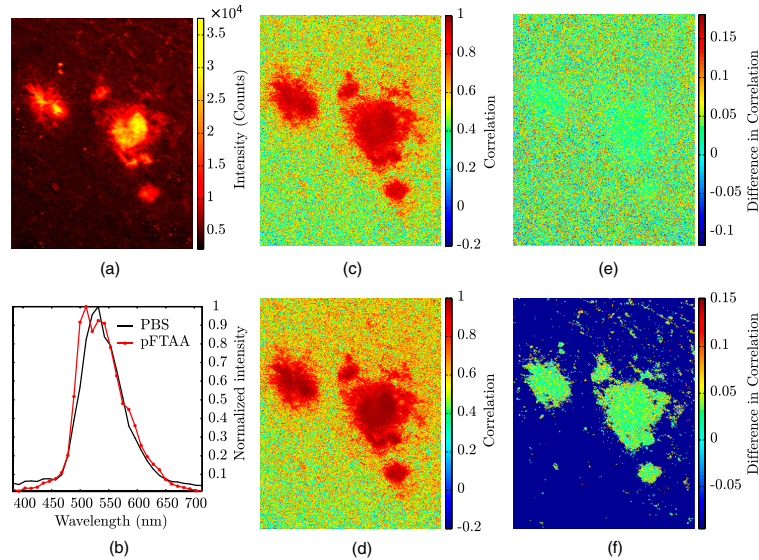


**Fig. 1** Correlation analysis of the amyloid beta plaques in an APP/PS1 mouse brain section. (a) shows the intensity image with the plaques clearly visible, and (b) shows the references spectra for PBS (autofluorescence) and pFTAA. Correlation between the measured spectrum and (c) PBS ( $\rho_{\text{PBS}}$ ) and (d) pFTAA ( $\rho_{\text{pFTAA}}$ ) is also shown. The difference  $\rho_{\text{pFTAA}} - \rho_{\text{PBS}}$  is shown without thresholding in (e), and with a threshold of 6,000 counts in the intensity in (f).

selecting the average spectrum of a circle with a diameter of 20 pixels in the central area of the plaques, and then averaging the 10 spectra into a reference spectrum. The pFTAA spectrum was defined from an average over a small region in the center of the plaque of the stained sample. An analysis was then done by calculating two different correlation coefficients between the measured spectra and the reference spectra of the stained sample. These correlation coefficient (from now on known as the correlation) images are shown in Fig. 1.

The intensity of the image is shown in Fig. 1(a), and the two reference spectra for AF and the stain pFTAA are shown in Fig. 1(b). Figure. 1(c) and 1(d) displays the map of the correlation between the PBS ( $\rho_{\text{PBS}}$ ) and pFTAA ( $\rho_{\text{pFTAA}}$ ) of the stained sample data set, respectively. The last two figures, 1(e) and 1(f), show the difference  $\rho_{\text{pFTAA}} - \rho_{\text{PBS}}$  without thresholding on the intensity (e) and with a threshold of 6,000 counts (f).

As can be seen from the reference spectra, the two spectra are very similar, confirmed by calculating the correlation between them, which is 0.9715. Even though they are this similar and give a high correlation in the plaque, as seen in Fig. 1(c) and 1(d), there is a significant difference between them, shown in Fig. 1(e) and even more clearly in Fig. 1(f), with ( $\rho_{\text{pFTAA}}$ ) being larger than  $\rho_{\text{PBS}}$  by approximately 0.04 for the whole plaque.

With the thresholding, we obtain a visually clearer mapping of the excess of the pFTTA signal, as shown in Fig. 1(f). As shown in this image, the method is good at distinguishing one reference spectrum from the background and/or AF, even though the method is well suited for analyzing more than one stain at a time, particularly when the stains have similar fluorescence spectra. In addition, it is not necessary to know more than one of the spectra present, as the correlation gives

a statistical number of how similar the spectra are. This makes it possible to statistically compare different images, regardless of their difference in intensity due to factors such as different acquisition settings. Such applications will be tested and validated in forthcoming studies.

The example application of the correlation method on a brain section from an APP/PS1-mouse shows its ability to distinguish two or more similar spectra, including the AF. The method shows promising results for hyperspectral fluorescence and confocal images. It is especially good with noisy images due to the nature of the correlation. However, due to its form, it is best suited for use on spectra where only some of the contributing signals (such as reference spectra) are known.

#### Acknowledgments

This work was supported by the EU-FP7 Health Programme Project LUPAS. We acknowledge the members of the LUPAS consortium for discussions and samples used for testing this method; in particular, we acknowledge Susann Handrick and Sofie Nyström for sample preparation.

#### References

1. R. A. Schultz et al., "Hyperspectral imaging: a novel approach for microscopic analysis," *Cytometry* **43**(4), 239–247 (2001).
2. I. T. Jolliffe, *Principal Component Analysis*, 2d Ed., Springer Series in Statistics, Springer-Verlag, New York (2002).
3. R. Lansford, G. Bearman, and S. E. Fraser, "Resolution of multiple green fluorescent protein color variants and dyes using two-photon microscopy and imaging spectroscopy," *J. Biomed. Opt.* **6**(3), 311–318 (2001).
4. C. M. Pieters and P. A. J. Englert, Eds., *Remote Geochemical Analysis: Elemental and Mineralogical Composition*, pp. 145–166, Cambridge University Press, Cambridge, UK (1993).

## JBO Letters

5. F. Kruse et al., "The spectral image processing system (SIPS)—Interactive visualization and analysis of imaging spectrometer data," *Remote Sens. Environ.* **44**(2–3), 145–163 (1993).
6. P. E. Dennison, K. Q. Halligan, and D. A. Roberts, "A comparison of error metrics and constraints for multiple endmember spectral mixture analysis and spectral angle mapper," *Remote Sens. Environ.* **93**(3), 359–367 (2004).
7. R. E. Walpole et al., *Probability and Statistics for Engineers and Scientists*, pp. 95–102, Pearson Education International, Upper Saddle River, New Jersey (2002).
8. P. Tait, *Introduction to Radar Target Recognition*, IEEE Radar, Sonar, Navigation, and Avionics Series, pp. 77–80, The Institution of Engineering and Technology (2005).
9. J. A. Richards, *Remote Sensing with Imaging Radar*, Signals and Communication Technology, pp. 58–61, Springer, Berlin, Heidelberg (2009).
10. A. Åslund, K. P. R. Nilsson, and P. Konradsson, "Fluorescent oligo and poly-thiophenes and their utilization for recording biological events of diverse origin—When organic chemistry meets biology," *J. Chem. Biol.* **2**(4), 161–175 (2009).
11. T. Klingstedt and K. P. R. Nilsson, "Luminescent conjugated poly- and oligo-thiophenes: optical ligands for spectral assignment of a plethora of protein aggregates," *Biochem. Soc. Trans.* **40**(4), 704–710 (2012).
12. K. P. R. Nilsson, M. Lindgren, and P. Hammarström, "A pentameric luminescent-conjugated oligothiophene for optical imaging of *in vitro*-formed amyloid fibrils and protein aggregates in tissue sections," *Methods Molec. Biol.* **849**, 425–434 (2012).
13. F. Stabo-Eeg et al., "Quantum efficiency and two-photon absorption cross-section of conjugated polyelectrolytes used for protein conformation measurements with applications on amyloid structures," *Chem. Phys.* **336**(2–3), 121–126 (2007).



P. G. Ellingsen, S. Nyström, N. K. Reitan, and M. Lindgren, “Spectral correlation analysis of amyloid  $\beta$  plaque inhomogeneity from double staining experiments,” *J. Biomed. Opt.* **18**, 101313 (2013)

**Paper 8**





# Spectral correlation analysis of Amyloid $\beta$ plaque inhomogeneity from double staining experiments

Pål Gunnar Ellingsen,<sup>a</sup> Sofie Nyström,<sup>b</sup> Nina Kristine Reitan,<sup>a</sup> and Mikael Lindgren<sup>a</sup>

<sup>a</sup>Norwegian University of Science and Technology, Department of Physics, Faculty of Natural Sciences and Technology, Trondheim, Norway

<sup>b</sup>Linköping University, IFM-Department of Chemistry, Linköping, Sweden

**Abstract.** A spectral correlation algorithm for the analysis of hyperspectral fluorescence images is proposed by Ellingsen et al. [J. Biomed. Opt. 18, 020501 (2013)]. Here, it is applied to the analysis of double-stained  $A\beta$  amyloid plaques being related to the Alzheimer's disease (AD). Sections of APP/PS1 AD mice model brains are double stained with luminescent-conjugated oligothiophenes, known to bind to amyloid protein deposits. Hyperspectral fluorescence images of the brain sections are recorded and by applying the correlation algorithm the spectral inhomogeneity of the double-stained samples is mapped in terms of radial distribution and spectral content. To further investigate the progression of  $A\beta$  amyloid plaque formation, 19 AD mice of different ages up to 23 months are characterized, enabling a statistical analysis of the plaque heterogeneity. In accordance with recent findings by Nyström et al. [ACS Chem. Biol. 8, 1128–1133 (2013)], the spectral distribution within  $A\beta$  plaques is found to vary with age throughout the lifespan of the mouse. With the new correlation algorithm, it is possible to quantify the spectral abundance of the two stains depending on the relative distance from the plaque center and mouse age. Thus, we demonstrate the use of the correlation analysis approach in double-staining experiments and how it is possible to relate these to structural/spectral changes in biological samples. © The Authors. Published by SPIE under a Creative Commons Attribution 3.0 Unported License. Distribution or reproduction of this work in whole or in part requires full attribution of the original publication, including its DOI. [DOI: 10.1117/1.JBO.18.10.101313]

Keywords: double stain; hyperspectral imaging; spectral analysis; Alzheimer's disease; amyloid plaque.

Paper 130134SSR received Mar. 8, 2013; revised manuscript received May 16, 2013; accepted for publication Jun. 27, 2013; published online Aug. 9, 2013.

## 1 Introduction

Modern fluorescence microscopes are capable of recording images with a reasonably resolved spectrum in each pixel, enabling advanced spectroscopic characterization of optically resolved structures. However, this requires access to adequate methods for resolving and discriminating spectral features or components of the generated hyperspectral images. There are several methods for accomplishing this, and they have become more and more sophisticated with the increase in computing power available in modern computers. One common way of doing spectral analysis is by linear spectral unmixing,<sup>1–3</sup> which classifies the measured spectrum in every pixel in terms of a linear sum of input references. If the reference spectra are not known, a commonly used method is the principal component analysis,<sup>4</sup> which separates the spectrum into its main (orthogonal) components, using statistics gathered from the image. Another approach that classifies the spectra is the spectral angle mapper algorithm.<sup>5–7</sup> All of these methods have their drawbacks, e.g., they are difficult to use if the signals are weak with interfering background fluorescence or if there are large differences in relative quantum efficiency of different spectral components. The problems associated with the common signal processing tools prompted us to propose a spectral cross-correlation algorithm for hyperspectral images.<sup>8</sup> The correlation coefficient<sup>8</sup> is advantageous over, for instance, linear spectral unmixing,<sup>1–3</sup> since it is statistically defined and scale invariant. It is limited to between  $-1$  and  $1$ , with  $-1$  being  $M = -R$ ,

$0 M = \text{random}$  and  $1 M = R$ . In spectral measurements, the measured intensities should never be negative, as intensity is dependent on the number of photons. As a result, the correlation coefficient should be larger than  $0$ , assuming the background offset is reasonably small. Due to random noise in the measurement, the correlation coefficient will never be exactly  $1$ . As will be shown, this method is well suited for the analysis of biological samples with a complex background as we can gain sensitivity by using all spectral ranges of the hyperspectral image, but we are at the same time able to discriminate the relative contribution from different spectral components as with the linear signal processing algorithms.

As a demonstration of the correlation algorithm,<sup>8</sup> we here present a detailed analysis of double-staining experiments of Alzheimer's disease (AD) progression in mouse models. AD is known to be accompanied by the accumulation of  $A\beta$  peptide deposits in the brain, although the relation to the disease is still in many respects unknown. Luminescent-conjugated oligothiophenes (LCOs)<sup>9</sup> and the related polymers<sup>10,11</sup> are known to bind to amyloid deposits and change its fluorescence emission, enabling spectral diagnostics of  $A\beta$  plaque formation.<sup>12</sup> Smaller variants of LCOs can be used *in vivo* as they pass the blood-brain barrier.<sup>13</sup> It was recently shown by Nyström et al.,<sup>14</sup> that simultaneous staining with two different LCOs reveals varying spectral characteristics based on structural differences of the formed protein aggregates. Central plaque regions appear to have larger spectral contribution from the shorter of the two LCOs, quadro-formylthiophene acetic acid (qFTAA), whereas the longer hepta-formylthiophene acetic acid (hFTAA), known to be more promiscuous and stain both prefibrillar aggregates and mature amyloid deposits, was shown to stain plaques from the different ages more uniformly. The results were

Address all correspondence to: Mikael Lindgren, Norwegian University of Science and Technology, Department of Physics, Faculty of Natural Sciences and Technology, Trondheim, Norway. Tel: +47 73593414; Fax: +47 73597710; E-mail: mikael.lindgren@ntnu.no

compared with *in vitro* fibrillation experiments and it was shown that the spectral characteristics of the two LCOs were related to the time point of the fibrillation process. Another study based on classification using spectral angle mapping by Wegenast-Braun et al.<sup>15</sup> confirmed the location of the LCO (hFTAA) to the plaques, and compared it to other conventional staining methods based on antibodies, Congo red, methoxy-X04, and thioflavin S.

The previous study by Nyström et al.<sup>14</sup> for characterization of age-dependent conformational rearrangements of the A $\beta$  deposits in AD relied on a rather simple comparison of two spectral components in the center of the doubly stained AD plaques. By using the correlation algorithm and developing auxiliary routines for plaque analysis, such as radial distribution analysis, we can obtain a wealth of detailed structural data. Here, we apply the cross-correlation algorithm and make a statistical analysis of relative fluorescence stain distribution of the same set of raw data as used in the study of Nyström et al.<sup>14</sup> Based on the correlation analysis, we make a detailed comparison between AD mice of different ages in a systematic manner to reveal further details of the progression of AD amyloid plaque formation in such mouse models.

## 2 Materials and Methods

### 2.1 Samples

The LCO staining solution, containing a mix of qFTAA and hFTAA, was prepared by using 1 mg ml<sup>-1</sup> stock solutions prepared in 2 mM NaOH and stored at 4°C while awaiting use. Synthesizing of qFTAA and hFTAA was done as described by Klingstedt et al.<sup>9</sup> Before staining, fresh solutions were prepared by diluting the stock to 1:500 in phosphate buffered saline (PBS). Then qFTAA and hFTAA were mixed in a ratio of 2:1, resulting in a final concentration of 2.4  $\mu$ M qFTAA and 0.7  $\mu$ M hFTAA, in assay solutions. Brain tissues from 19 mice aged 6 to 23 months were employed in the study to facilitate the investigation of the age dependence of spectral variations in the plaques. About 10  $\mu$ m cryo sections were prepared and kept at -20°C until needed. The LCO staining solution containing a mix of qFTAA and hFTAA was applied to the cryosections. The sections were washed 3  $\times$  5 min with PBS and mounted with Dako fluorescence mounting medium. The slides were left in room temperature in the dark overnight and sealed with nail polish. Structures for qFTAA and hFTAA can be seen in Fig. 1. See Nyström et al. for further details.<sup>14</sup>

### 2.2 Hyperspectral Imaging

After preparation, the samples were imaged using a Leica DM6000 B fluorescence microscope mounted with a SpectraCube module from applied spectral imaging (ASI). An excitation wavelength filter with peak transmission at 405 nm and a full width at half maximum of  $\approx$ 20 nm and a

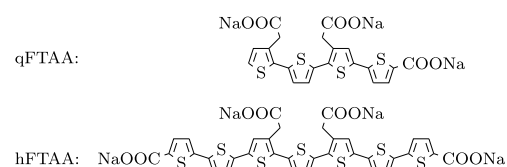


Fig. 1 Chemical structures for the LCOs qFTAA and hFTAA.

long-pass filter allowing emission above 450 nm were used to block back-propagating light from the excitation.

### 2.3 Correlation Analysis

The correlation analysis, see Ellingsen et al. for the details,<sup>8</sup> is based on calculating the cross-correlation coefficient  $\rho$  between the measured spectrum in a pixel ( $M$ ) and a reference spectra ( $R$ ). This is repeated for every pixel in the hyperspectral image above a certain background threshold, yielding a new image with the correlation coefficient. If there are additional reference spectra, the process is repeated, yielding one correlation image for each reference spectrum. For the remainder of this work, the correlation coefficient will be referred to as the correlation.

## 3 Results and Discussion

### 3.1 General Approach for Collecting Data

Hyperspectral images were recorded using the fluorescent microscope (Leica) equipped with an ASI Sagnac interferometric hyperspectral imager, see Sec. 2.2 for details. The initial hyperspectral images, each containing several plaques, were thresholded to remove background (signal to noise of more than 10 for the intensity image, with the same level for individual spectral channels) and then the data of individual plaques were extracted using operator selected region of interest (ROI). Figure 2 shows an example of the thresholded image and Fig. 3 shows a resulting cropped image.

Totally, 19 different AD mice were examined and data were collected from between 5 and 34 plaques (with majority of them above 20) for each age (some mice showed more plaques than others). Correlation images were then generated from this set of raw data using reference spectra from plaques stained with pure qFTAA and hFTAA, respectively. The two reference spectra are shown in Fig. 4. For more details on the acquisition of these spectra, see Nyström et al.<sup>14</sup> As can be seen in Fig. 4, the references are well defined, with distinct spectral differences. When mixed and used in double staining the resulting spectra will be harder to separate due to the occurrence of both stains and a

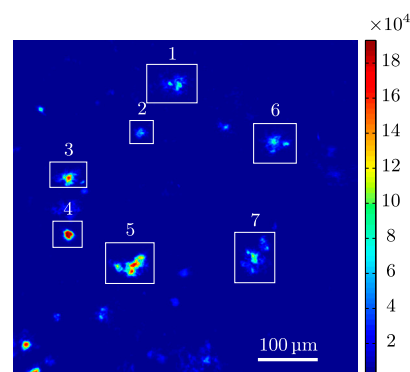
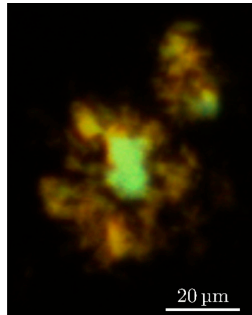
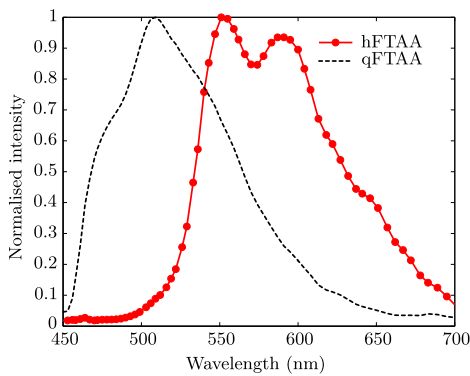


Fig. 2 Intensity image (sum over spectrum) with regions of interest showing the seven cropped areas used in the rest of the analysis. Color scale is in counts. The threshold of 3500 counts is shown as dark blue. The mouse age was 686 days.



**Fig. 3** Intensity image of crop number 7 in Fig. 2 colored in the natural colors of the eye using the algorithm described in Ref. 16. (See Video 1 MPEG, 0.8 MB) [URL: <http://dx.doi.org/10.1117/1.JBO.18.10.XXXXXX.1>] for a wavelength scan over the image.



**Fig. 4** The reference spectra for qFTAA and hFTAA recorded in single-stain experiments.

background that can vary depending on the location within the sample and the sample itself.

Qualitative observation of plaques generally showed a diffuse structure surrounding a region of high fluorescence, defining a center of high fluorescence intensity. The plaque shapes were not distinct but essentially circular with small elliptical distortions, or with patches of smaller regions with high intensities arranged around an essentially circular main plaque. Two ways of identifying the plaque center was tested: (1) from the average of some pixels of highest intensity, or (2) by calculating the center of mass for the whole intensity distribution, see e.g., Adams.<sup>17</sup> The latter approach was abandoned as it generated a much larger spread of data when calculating radial distributions, especially with plaques that were far from spherical. Therefore, approach (1) was adopted by defining a threshold for the background intensity (sum over the spectrum) image, and then finding the maximum after passing it through a  $3 \times 3$  median filter. The motivation for adopting this approach was that the plaques are actually sections of three-dimensional structures. A consequence would then be that the center would be the area where the plaque is “thickest” and therefore the fluorescence intensity should be the highest. Using a median filter

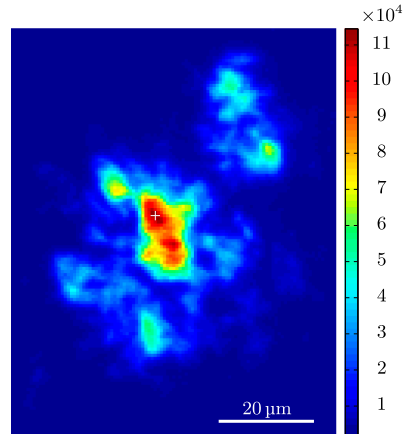


**Fig. 5** Image showing the sum over the spectrum for crop number 7 in Fig. 2. The white plus in the figure marks the center used in the radial analysis. Color scale is in counts. The threshold of 3500 counts is shown as dark blue.

ensures that a singular pixel with a high intensity, e.g., from noise or a measurement error, was not chosen as the center. An example of such a defined center is shown in Fig. 5 for a plaque that is very irregular in shape. The choice of method for finding the center for any of the methods will give some results where the center is ill-defined; however, owing to the nature of the statistical analysis, as long as the majority of the centers are found well enough, the overall results from the statistics should make the most probable distribution most significant.

After the correlation images for all the plaques were generated, (see representative correlation images for the two stains in Fig. 6), the data set was further analyzed in terms of radial distribution and mouse age.

### 3.2 Spectral Correlations Versus Radial Distribution

Having calculated the correlation for every pixel in an image, we now want to map its distribution, e.g., the radial distribution within a plaque. The distance or radius from the plaque center  $r$  is given by

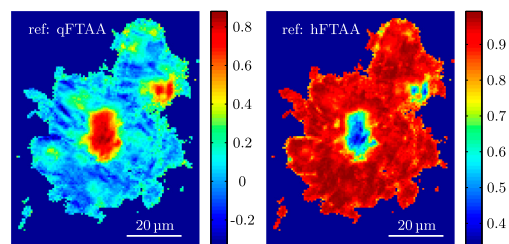


**Fig. 6** Image showing the correlation between the qFTAA (left) or hFTAA (right) reference and the measured spectrum. The crop is the same as Fig. 5. Notice the big difference in the center of the plaque between the correlation value. The threshold of 3500 counts is shown as dark blue.

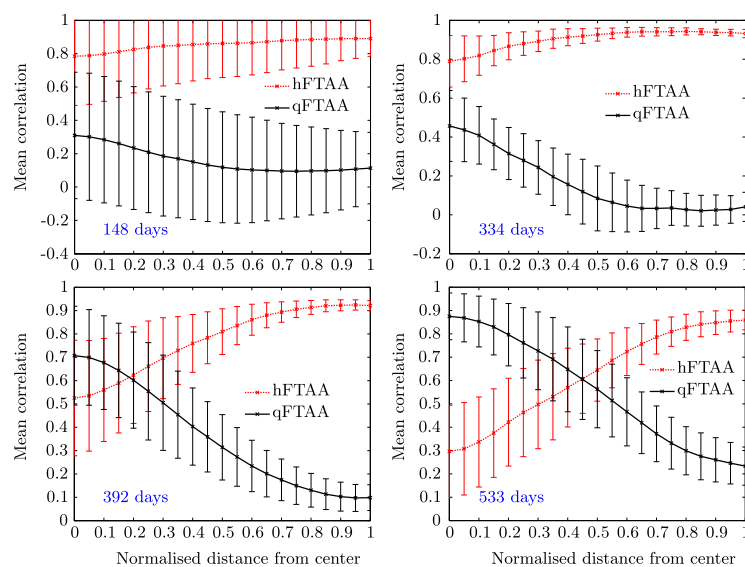


**Fig. 7** The mean correlation and its standard deviation as a function of normalized distance from center (radius) for four mice of different ages. The mean and standard deviation are calculated over all analyzed plaques of each mouse. The age is indicated in each plot.

$$r = \sqrt{(X - x)^2 + (Y - y)^2},$$

where  $(X, Y)$  is the center as discussed in Sec. 3.1 and  $(x, y)$  represents the coordinate of a given pixel in the image. The value of the radius is rounded to an integer, and all of the valid pixels (those above the background threshold) are sorted into bins according to their integer value, enabling the plotting of correlation as a function of radius for each correlation distribution. As the goal was to compare different plaques with different sizes (due to, for instance, age, sample preparation, and imaging), the radius needed to be normalized. This was done by distributing the radii onto 21 uniformly spaced radii between 0 and 1. This is equivalent to dividing the radius by the maximum and then re-sampling the data to 21 points from a much higher number of points. With a normalized radius, it was possible to do statistics for the correlation of each mouse as a function of plaques radius. Four of these statistical plots, showing the mean and standard deviation as a function of radius, are shown in Fig. 7. These plots are not randomly selected, rather they are the most clear examples of the progression of the radial distribution as a function of mouse age: Figs. 6 and 7 clearly show that qFTAA stains the center of a plaque much better than the periphery. For hFTAA the situation is opposite, with the highest values in the periphery and the smallest in the center.

The findings so far are in agreement with the simple analysis in Nyström et al.<sup>14</sup> based on a simple comparison of intensities of two spectral emission peaks in the center of a plaque, where the peak at 500 nm corresponds to the binding of qFTAA and the peak at 540 nm reflects the binding of hFTAA. The difference between the two references becomes even more pronounced the older the mice are, with the correlation eventually crossing each other somewhere around 400 days (see Fig. 7). From this, it can

be deduced that there is a clear change over time with respect to the structure of the plaque, clearly inhibiting the binding of hFTAA in the center. Since the LCOs are sensitive to the conformation of the proteins within the  $A\beta$  plaque, this yields a very promising result for the study of structural changes within the plaque for different ages. Further details of the spectral correlation was obtained from a statistical analysis of all plaques, to be discussed below (Sec. 3.3).

### 3.3 Statistical Analysis of Spectral Distribution

In addition to the four mouse ages shown in Fig. 7, data of 15 more AD mice were recorded, correlated with the references and the corresponding radial characteristics was calculated for each age. In order to plot the wealth of analyzed data, the relative abundance of the hFTAA and qFTAA spectral components are plotted as a function of mouse age at different relative radii as in Fig. 8. Hereby, we obtain an overview of the spectral characteristics for the essential regions of the plaques. This shows that the correlation for qFTAA and hFTAA in the plaque center varies significantly as a function of age, apparently crossing each other for mice at approximately 340–490 days of age. In the outer regions of the plaques (Fig. 8: lower panels), the relative abundance is relatively constant up to approximately 500 days of age. Here, hFTAA has a much larger propensity to bind with a correlation value close to 1. These results and conclusions are in agreement with the simpler analysis in Nyström et al.<sup>14</sup> Interestingly, the correlation analysis shows a pronounced “second wave” as qFTAA increases its correlation value in the outer regions above 500 days. Also, a second crossing of the correlation values is prominent at plaque center (Fig. 8: upper left panel), indicating that there are different structural properties of plaques in the younger mice (<500 days) compared with the older ones, and that hFTAA staining

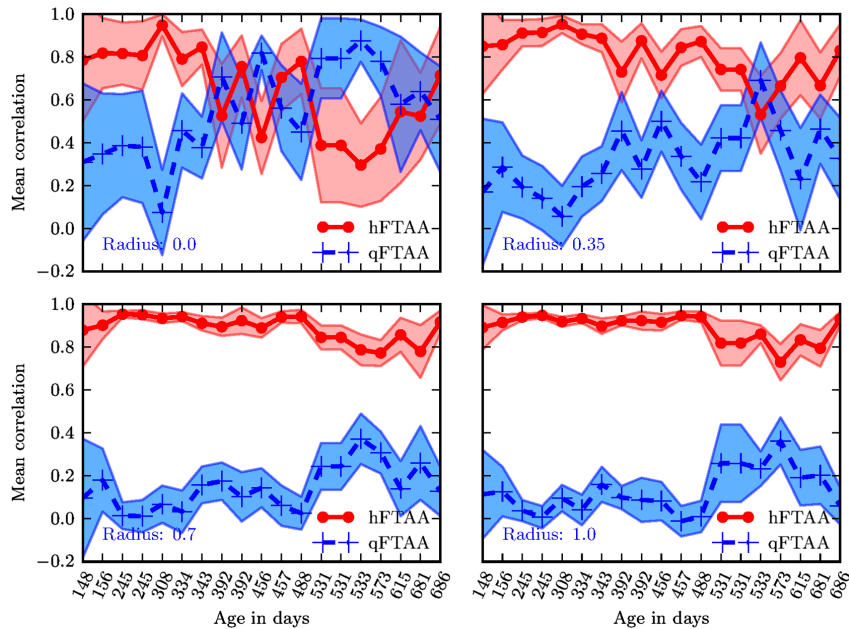


**Fig. 8** Mean correlation as a function of age in days and normalized distance from the center. Notice that the x-axis (age) is uniformly spaced with respect to each case, and that there are three identical ages (245, 392, 531 days) which are from different mice and therefore are shown as different points. The outer red/blue borders denote the standard deviation.

starts to dominate the plaque centers again at >600 days. These results and conclusions are in agreement with the simpler analysis in Nyström et al.<sup>14</sup> Variation in plaque morphologies in both man<sup>18</sup> and mouse<sup>12</sup> has been documented earlier. However, our described method allows for both qualitative and quantitative analysis of images from biological specimens due to the ability to analyze the entire image for a series of images in a data set. Together with the ability to analyze radial distributions and smaller spectral differences, it provides a more detailed and accurate approach, with statistically verified results.

#### 4 Conclusion

This paper shows the application of spectral correlation on hyperspectral images obtained from samples of double-stained  $A\beta$  amyloid plaques of AD mice brain sections. Using the spectral correlation approach, we obtain a wealth of signal processing results that can be used to assess the structural composition leading to spectral changes in detail. In agreement with a previous study based on a simple two spectral point comparison,<sup>14</sup> it is found that there are structural changes within the plaques for AD mice of different ages. Using our analysis strategy, these spectral changes could be quantified in detail and it was found that the radical distribution of relative abundance showed a clear monotonous change in AD mice up to about 500 days of age. Moreover, a second transition in terms of plaque inhomogeneity was observed for mice of very old age (>500 days) and this may suggest further detailed studies of AD mouse models at high ages. Conclusively, the spectral correlation algorithm was demonstrated as useful in the assessment of fluorescence hyper spectral images in multiple staining experiments.

#### Acknowledgments

This work was supported by the EU-FP7 Health Programme Project LUPAS ([www.lupas-amyloid.eu](http://www.lupas-amyloid.eu)). In addition, Sofie Nyström was supported by the Swedish Alzheimer Foundation. We acknowledge the members of the LUPAS consortium for discussions and samples used for testing the cross-correlation method. In particular, we acknowledge Susann Handrick and Bettina Wegenast-Braun for assisting in sample preparations and Profs. Per Hammarström, Peter Nilsson, Christian Liebig, Frank Heppner, and Mathias Jucker for valuable discussions.

#### References

1. M. E. Dickinson, "Multi-spectral imaging and linear unmixing add a whole new dimension to laser scanning fluorescence microscopy," *Biotechniques* **31**(6), 1272–1278 (2001).
2. T. Zimmermann, "Spectral imaging and its applications in live cell microscopy," *FEBS Lett.* **546**(1), 87–92 (2003).
3. T. Zimmermann, "Spectral imaging and linear unmixing in light microscopy," *Microsc. Tech.* **95**, 245–265 (2005).
4. I. T. Jolliffe, *Principal Component Analysis*, 2nd ed., Springer Series in Statistics, Springer-Verlag, New York (2002).
5. O. A. De Carvalho and P. R. Meneses, "Spectral correlation mapper (SCM): an improvement on the spectral angle mapper (SAM)," in *Airborne Visible/Infrared Imaging Spectrometer (AVIRIS) 2000 Workshop Proceedings*, Pasadena, CA (2000).
6. P. E. Dennison, K. Q. Halligan, and D. A. Roberts, "A comparison of error metrics and constraints for multiple end member spectral mixture analysis and spectral angle mapper," *Rem. Sens. Environ.* **93**(3), 359–367 (2004).
7. H. Z. M. Shafri, A. Suhaili, and S. Mansor, "The performance of maximum likelihood, spectral angle mapper, neural network and decision

- tree classifiers in hyperspectral image analysis," *J. Comput. Sci.* **3**(6), 419–423 (2007).
8. P. G. Ellingsen et al., "Hyperspectral analysis using the correlation between image and reference," *J. Biomed. Opt.* **18**(2), 20501 (2013).
  9. T. Klingstedt et al., "Synthesis of a library of oligothiophenes and their utilization as fluorescent ligands for spectral assignment of protein aggregates," *Org. Biomol. Chem.* **9**(24), 8356–70 (2011).
  10. K. P. R. Nilsson et al., "Conjugated polyelectrolytes–conformation-sensitive optical probes for staining and characterization of amyloid deposits," *Chembiochem: Eur. J. Chem. Biol.* **7**(7), 1096–104 (2006).
  11. F. Stabo-Eeg et al., "Quantum efficiency and two-photon absorption cross-section of conjugated polyelectrolytes used for protein conformation measurements with applications on amyloid structures," *Chem. Phys.* **336**(2–3), 121–126 (2007).
  12. K. P. R. Nilsson et al., "Imaging distinct conformational states of amyloid-beta fibrils in Alzheimer's disease using novel luminescent probes," *ACS Chem. Biol.* **2**(8), 553–560 (2007).
  13. A. Aslund et al., "Novel pentameric thiophene derivatives for in vitro and in vivo optical imaging of a plethora of protein aggregates in cerebral amyloidoses," *ACS Chem. Biol.* **4**(8), 673–684 (2009).
  14. S. Nyström et al., "Evidence for age dependent in vivo conformational rearrangement within A $\beta$  amyloid deposits," *ACS Chem. Biol.* **8**(6), 1128–1133 (2013).
  15. B. M. Wegenast-Braun et al., "Spectral discrimination of cerebral amyloid lesions after peripheral application of luminescent conjugated oligothiophenes," *Am. J. Pathol.* **181**(6), 1953–1960 (2012).
  16. R. L., "Conversion of wavelength in nanometers to RGB in Python," *Coding Mess*, May 2009, <http://codingmess.blogspot.no/2009/05/conversion-of-wavelength-in-nanometers.html> (03 06 2013).
  17. R. A. Adams, *Calculus: A Complete Course*, 5th ed., pp. 432–437, Addison-Wesley, Toronto (2003).
  18. L.-W. Jin et al., "Imaging linear birefringence and dichroism in cerebral amyloid pathologies," *Proc. Natl. Acad. Sci. U. S. A.* **100**(26), 15294–15298 (2003).

P. G. Ellingsen and M. Lindgren, “Design and test of a Raman spectroscopic system based on a time-gated intensified CCD,” *Submitt. to Opt. Express* 4. June 2014 (2014)

**Paper 9**





# Design and test of a Raman spectroscopic system based on a time-gated intensified CCD

Pål Gunnar Ellingsen and Mikael Lindgren

Department of physics, Norwegian University of Science and Technology  
7491 Trondheim, Norway  
[mikael.lindgren@ntnu.no](mailto:mikael.lindgren@ntnu.no)

**Abstract:** We have designed and developed a system for time-gated spectroscopy, specifically Raman and luminescence spectroscopy. The system is based on a 2 ns pulsed Nd:YAG laser, a spectrometer with a time-gated intensified CCD (ICCD), allowing detection from 2 ns gate-width and longer, at arbitrary time point. We demonstrate the recording of Raman spectra of luminescent samples, removing background luminescence by time-gating. We also demonstrate the use of spectral correlation analysis to verify weak spectral components in a solvent with a trace amounts of solute.

© 2014 Optical Society of America

**OCIS codes:** (000.0000) General. Time gated spectroscopy, Raman, Luminescence, Spectral analysis

---

## References and links

1. C. V. Raman and K. S. Krishnan, "A new type of secondary radiation," *Nature* **121**, 501–502 (1928).
2. I. Lewis and H. Edwards, *Handbook of Raman spectroscopy: from the research laboratory to the process line* (CRC Press, 2001).
3. P. Matousek, M. Towrie, C. Ma, W. M. Kwok, D. Phillips, W. T. Toner, and a. W. Parker, "Fluorescence suppression in resonance Raman spectroscopy using a high-performance picosecond Kerr gate," *J. Raman Spectrosc.* **32**, 983–988 (2001).
4. R. C. Wiens, S. K. Sharma, J. Thompson, A. Misra, and P. G. Lucey, "Joint analyses by laser-induced breakdown spectroscopy (LIBS) and Raman spectroscopy at stand-off distances," *Spectrochim. Acta. A. Mol. Biomol. Spectrosc.* **61**, 2324–34 (2005).
5. S. M. Angel, N. R. Gomer, S. K. Sharma, and C. McKay, "Remote Raman spectroscopy for planetary exploration: a review," *Appl. Spectrosc.* **66**, 137–50 (2012).
6. M. Gaft and L. Nagli, "UV gated Raman spectroscopy for standoff detection of explosives," *Opt. Mater. (Amst)* **30**, 1739–1746 (2008).
7. I. T. Jolliffe, *Principal Component Analysis*, Springer Series in Statistics (Springer-Verlag, New York, 2002), second ed. ed.
8. R. Lansford, G. Bearman, and S. E. Fraser, "Resolution of multiple green fluorescent protein color variants and dyes using two-photon microscopy and imaging spectroscopy," *J. Biomed. Opt.* **6**, 311–8 (2001).
9. R. E. Walpole, R. H. Myers, S. L. Myers, and K. Ye, *Probability and Statistics for Engineers and Scientists* (Pearson Education, 2002), 7th ed.
10. P. G. Ellingsen, N. K. Reitan, B. D. Pedersen, and M. Lindgren, "Hyperspectral analysis using the correlation between image and reference," *J. Biomed. Opt.* **18**, 20501 (2013).
11. P. G. Ellingsen, S. Nyström, N. K. Reitan, and M. Lindgren, "Spectral correlation analysis of amyloid  $\beta$  plaque inhomogeneity from double staining experiments," *J. Biomed. Opt.* **18**, 101313 (2013).
12. S. A. Asher, "UV resonance Raman spectroscopy for analytical, physical, and biophysical chemistry. Part 1," *Anal. Chem.* **65**, 59A–66A (1993).
13. ASTM, "Standard Guide for Raman Shift Standards for Spectrometer Calibration," *Annu. B. ASTM Stand.* **E1840-96**, 1–11 (2007).

14. R. Westlund, E. Glimsdal, M. Lindgren, R. Vestberg, C. Hawker, C. Lopes, and E. Malmström, "Click chemistry for photonic applications: triazole-functionalized platinum(ii) acetylides for optical power limiting," *J. Mater. Chem.* **18**, 166 (2008).
  15. M. O. Trulson and R. A. Mathies, "Raman cross section measurements in the visible and ultraviolet using an integrating cavity: Application to benzene, cyclohexane, and cacodylate," *J. Chem. Phys.* **84**, 2068 (1986).
  16. B. Li and A. B. Myers, "Absolute Raman cross sections for cyclohexane, acetonitrile, and water in the far-ultraviolet region," *J. Phys. Chem.* **94**, 4051–4054 (1990).
  17. E. Glimsdal, M. Carlsson, T. Kindahl, M. Lindgren, C. Lopes, and B. Eliasson, "Luminescence, singlet oxygen production, and optical power limiting of some diacetylide platinum(II) diphosphine complexes," *J. Phys. Chem. A* **114**, 3431–42 (2010).
  18. R. Westlund, E. Malmström, C. Lopes, J. Öhgren, T. Rodgers, Y. Saito, S. Kawata, E. Glimsdal, and M. Lindgren, "Efficient Nonlinear Absorbing Platinum(II) Acetylide Chromophores in Solid PMMA Matrices," *Adv. Funct. Mater.* **18**, 1939–1948 (2008).
- 

## 1. Introduction

Raman spectroscopy has been developed extensively by advances in both instrumentation and theory since its was first observed in 1928 by C.V. Raman [1]. It is now an important tool for characterisation of chemical, geological, biological and medical samples, and widely used in all fields of natural sciences as well as applications such as forensics [2]. Even with all of these advances there are still samples that can not be easily characterised, due to luminescence from the sample. As the unwanted luminescence can be orders of magnitude larger than the desired Raman signal, the common solutions so far have been long exposures, curve fitting and the use of long wavelengths shifted far away from the absorption giving rise to luminescence excitation. All of these have drawbacks limiting their use in applications.

Raman scattering is known to be "instantaneous", whereas luminescence typically occurs in the range 1 ns to 100 ns for fluorescence and >100 ns for phosphorescence. Previously, the suppression of luminescence and fluorescence has been demonstrated by using a Kerr gated system [3]. This results in a time-resolution of about 4 ps, and a quite complex optical system. In comparison we here present a much easier time-gated spectrometer which can be used to measure Raman spectra with reduced luminescence, as well as measuring the luminescence spectra, allowing the instantaneous recording of a full spectrum or a segment of a spectrum. The system is made possible by the availability of pulsed lasers and intensified CCDs (ICCD). Similar systems, with longer gate-times than the system presented here, have previously been tested and proposed for planetary exploration [4, 5] and for detection of explosives [6].

Having recorded the spectra it can be interesting to analyse its chemical composition in terms of the contributing Raman signals from the various components. For instance, this would be interesting if the sample contains a mixture of several different substances, each with its own distinct spectrum. In the case where the component spectra are unknown, it is possible to use principle component analysis [7, 2]. In many Raman spectroscopy cases, the reference spectra can be "guessed", either from prior knowledge or by analysing the peak positions in the spectrum. For these cases one common solution for finding the relative abundances, like in fluorescence spectroscopic imaging, is linear spectral unmixing[8]. This method has some disadvantages with regards to background noise, signal to noise level and the linearity of the mixing procedure. In this context we recently developed a method base upon calculating the correlation coefficient[9] between a reference and the measured spectrum. It was developed and used on hyperspectral fluorescence images[10, 11], and is here adopted to demonstrate sensitive detection of components in Raman spectra.

## 2. Experimental setup

Our setup, shown schematically in figure 1, is based on an Ekspla 2 ns pulsed Nd:YAG laser, a spectrometer coupled with an ANDOR time-gated intensified CCD (ICCD), and in addition

focusing and polarisation optics. In order not to damage the samples, the Ekspla laser was modified to allow for adjustment of the pulse energy. The modification consists of mounting a motorised rotator on the wave plate before the beam enters the nonlinear crystals, enabling the control of the coupling efficiency in these. This modification results in some leakage of the 1064 nm light into the beam, which is especially a problem from the the 532 nm beam. In the latter case it is removed by a combination of a grating and a band pass filter (not shown in figure 1). In order to control the incident polarisation upon the sample, wave plates are used, shown in figure 1. They have be adjusted to ensure an incident diagonal ( $45^\circ$ ) polarisation upon the sample.

The laser consists of 1064 nm beam, which can be either frequency doubled, tripled or quadrupled resulting in excitation wavelengths of 532 nm, 355 nm or 266 nm. The possibility to excite in the UV, means that it is possible to do UV resonance Raman spectroscopy, where the excitation is to an excited state in comparison to the usual case of a virtual state [12].

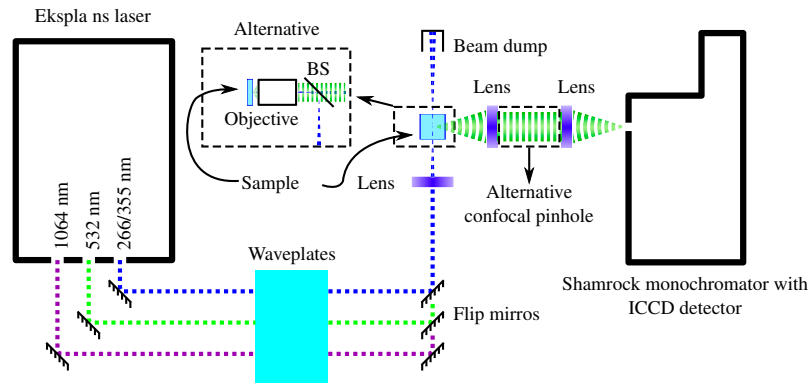


Fig. 1: A schematic drawing of the time-gated Raman spectrometer setup. The modified setup used for measuring data for the spectral correlation analysis is also shown. BS stands for beam splitter. The triggering connection between the laser and the ICCD detector is not shown. Also not shown is the computer cables controlling the monochromator and the ICCD camera.

In the system, the time-gated detection is controlled by settings of the ICCD. The ICCD camera is time-gated using an electric field. The electric field is controlled by setting the voltage of a photocathode, which converts the incoming photons to electrons, and a phosphorous screen, which converts the electrons back to photons. After the photons are converted back from electrons by the phosphorus screen, they are detected by a CCD. The use of an electric field enables the on and off switching of the amplification with less than a 2 ns gate width. In addition it is possible to adjust the field strength, changing the amplification level up to  $\approx 10000$  times the incoming number of photons.

In order to calibrate the system with respect to wavelength, a sample of cyclohexane was used as a reference, as suggested in [13]. This calibration is done in post processing of the signal by fitting the known peak position to a polynomial. The polynomial describes the mapping from measured wavelength to actual calibrated wavelength.

For the test with the spectral correlation analysis, the system was slightly modified as shown in figure 1. It was changed from a  $90^\circ$  configuration to a reflection setup by using a glass

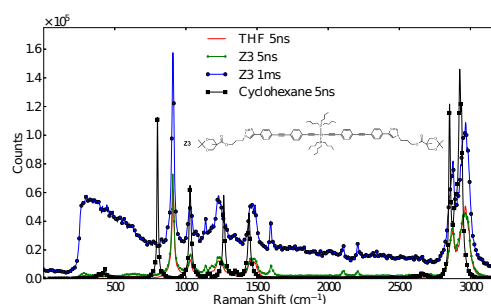


Fig. 2: Measured Raman spectra for THF and Z3 dissolved in THF, at excitation of 532 nm. The cyclohexane spectrum was used to calibrate the wavelength and is shown for reference. Z3 was measured with a both 5 ns gate and a 1 ms gate in order to show the advantage of the time gate. In addition the chemical structure of Z3 is shown.

slide as a beam splitter and a  $32\times$  objective to focus the beam onto the sample. The Raman scattered light then passes back through the beam splitter, going to the monochromator through a pinhole of  $200\mu\text{m}$ , ensuring confocal detection. The confocal detection resulted in a good spatial location of the origin of the signal (which is of advantage for solid samples), at the cost of some loss in intensity. Additionally, the wave plate was adjusted such that the polarisation was vertical.

### 3. Samples for testing the system

Testing and evaluating the suppression of luminescence in the detection system was done by measuring the Pt-acetylide chromophore abbreviated Z3 [14], and cyclohexane, spectrophotometric grade from Sigma-Aldrich, as the reference. Z3 was used because it has a relatively long lifetime luminescence. The cyclohexane ring structure with high symmetry results in a relatively simple Raman spectrum. This together with a lack of luminescence makes it suited for measuring the UV resonance known to occur in cyclohexane [15, 16]. The samples were measured in a 10 mm quartz cuvettes. Z3 was first dissolved in THF, GC grade from Sigma-Aldrich. Oxygen in the solvent quenching the phosphorescence was removed by a freeze-thaw procedure as described by Glimsdal et al. [17], resulting a bright phosphorescence with decay time of several hundred microseconds [17].

As a further test of the sensitivity in the system, 1 ml of spectroscopic grade tetrahydrofuran (THF), from Sigma-Aldrich, was diluted by removing  $800\mu\text{l}$  and replacing it with the same amount of tap water. The result was a  $1/5$  volume fraction of THF to tap water. By repeating this process, dilutions of  $1/25$ ,  $1/125$ ,  $1/625$  . . . ,  $1/15625$  were made. For each of the dilutions, the spectrum was recorded. In post processing the correlation coefficient between each of these spectra and the reference spectra for pure THF and pure tap water was calculated.

### 4. Results and discussion

For the test of suppression of the long lifetime luminescence, Z3 was measured. The spectra were recorded using the laser wavelength of 532 nm both with a time gate of 5 ns and 1 ms with the same amplification, 700 accumulations, a repetition rate of 10 Hz and a integration time of 3.5 ms. This resulted in the spectra shown in figure 2.

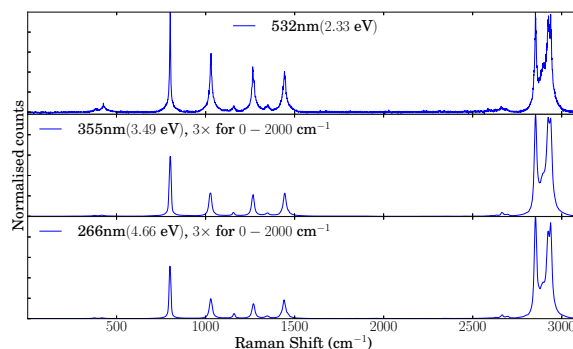


Fig. 3: Measured Raman spectra of cyclohexane at different excitation wavelengths with the same excitation energy and number of averages. Note that the  $0\text{ cm}^{-1}$  to  $2000\text{ cm}^{-1}$  range is zoomed in with a factor of 3 for the 355 nm and 266 nm excitations.

As can be seen in the figure, the measured spectrum for Z3 shows some peaks that are different from the THF peaks, as would be expected due to the different chemical structure. The assignment of the main peaks by Westlund et al. [18] are as follows:  $1128\text{ cm}^{-1}$  and  $1592\text{ cm}^{-1}$  carbon-carbon double bonds, and  $2208\text{ cm}^{-1}$  and  $2102\text{ cm}^{-1}$  carbon-carbon triple bonds in connection with the central platinum, see the chemical structure shown in the same figure. Suppression of the luminescence is clearly seen in the difference between the 5 ns gate and the 1 ms gate spectrum. The position of the peaks are the same, but the background luminescence is much larger for the long gate, as expected. Another difference is the height of the Raman peaks, which is due to the amplification in the ICCD not reaching maximum value for the short gate. However, better signal to noise ratio is achieved at shorter gate widths, as the detection system is not plagued by the background luminescence.

For studying the resonance Raman from cyclohexane, three different measurements were carried out, one for each of the harmonic wavelengths available. The results are shown in figure 3. The spectra were recorded with  $20\text{ }\mu\text{J}$  pulses and identical settings on detection system. But since another grating had to be used for the 266 nm excitation, and the monochromator and detector system were not calibrated with respect to absolute intensity, it is not possible to directly compare the intensities and thereby calculate a Raman cross section which could be compared to the known ones [15, 16]. Therefore the spectra have been normalised, but fortunately it is also possible to get an idea of the increase in signal strength by looking at the signal to noise ratio. By studying figure 3, one can clearly see that the signal to noise ratio becomes better the further one moves into the UV with the excitation laser wavelength. Another effect is the relative change in the strength of the peaks as a function of wavelength, where the  $801\text{ cm}^{-1}$  line and the  $2850\text{--}2950\text{ cm}^{-1}$  lines scale differently. The amount of scaling is more than expected from Trulson et al. [15], though this can be due to for instance nonlinearities in the detector system and stimulated Raman excitation due to the high peak intensity.

To test the sensitivity of the system, several different dilutions of tap water in THF was measured. The measurement settings were an excitation wavelength of 532 nm, a repetition rate of 55 Hz, 30000 accumulations and a 4 ns gate width. In addition photon counting was used, removing the need to carry out background subtraction. This was carried out by thresholding the device just above the dark count level and counting any signal above this as a single photon

count. The resulting spectra from the measurements are shown in figure 4a). Having measured these spectra, the correlation coefficients between the spectra and water or THF, were calculated. The results of the calculations are shown in figure 4b). By studying the change of the correlation value with amount of with THF, it is possible to see that correlation can detect the presence of THF down to a concentration of  $\approx 1/1000$ . It is here worth noting that the maximum number of photon counts is below 1000.

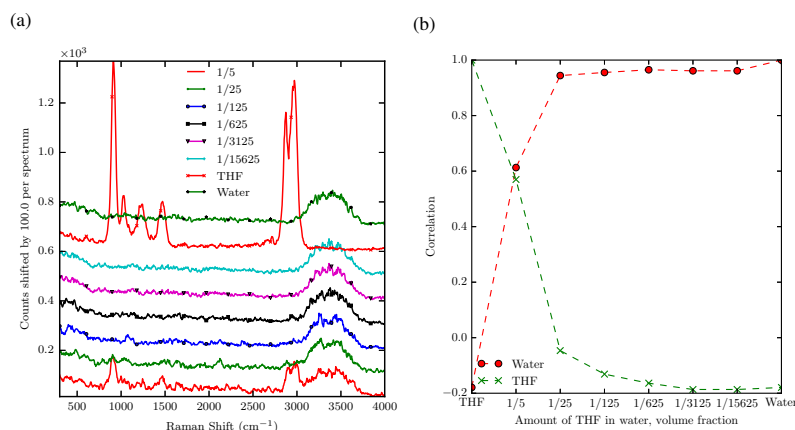


Fig. 4: a) Measured Raman spectra for the different volume fractions of THF in tap water, as well as pure THF and tap water. The spectra have been shifted by 100 counts to clarify the differences. Excitation was done at 532 nm. b) Correlation coefficient between the spectra and both THF and tap water.

From these result it is envisioned that the correlation method can be useful for detecting trace substances with a well know reference spectrum in for instance art recovery and forensics. Another use could be in hyperspectral Raman imaging, where it will give the ability to generate a number per pixel which can be used in a statistical analysis. This has been shown to be effective in hyperspectral fluorescence images [11, 10] and is therefore expected to work also for Raman spectral images.

## 5. Conclusion

We here presented a time-gated Raman system capable of measuring the luminescence and Raman spectrum of a sample, down to 2 ns gate widths, with a high amplification of the signal. This greatly reduces the background from long lifetime luminescence. The system is also equipped for doing UV resonance Raman, and this is shown for cyclohexane. In addition we show the detection limits of the system by applying a newly developed spectral correlation analysis to a 1/1000 dilution of tetrahydrofuran in water.